UNIVERSITY OF ICELAND

Ph.D. Thesis
in Physics

Growth and characterization of Mn-based magnetic MAX phases

The quest for room temperature ferromagnetism

Einar Baldur Þorsteinsson

November 2025

FACULTY OF SCIENCE

Growth and characterization of Mn-based magnetic MAX phases

Einar Baldur Þorsteinsson

Thesis submitted in partial fulfillment of a
Philosophiae Doctor degree in Physics

Ph.D. Committee
Friðrik Magnus (Advisor)
Einar Örn Sveinbjörnsson
Unnar Bjarni Arnalds
Árni Sigurður Ingason

Opponents
Hans Högberg
Michael Farle

Faculty of Science
School of Engineering and Natural Sciences
University of Iceland
Reykjavik, November 2025

Growth and characterization of Mn-based magnetic MAX phases
The quest for room temperature ferromagnetism
(Mn-based magnetic MAX phases)

Thesis submitted in partial fulfillment of a *Ph.D.* degree in Physics

Faculty of Science
School of Engineering and Natural Sciences
University of Iceland
Dunhagi 5
107 Reykjavik
Iceland

Telephone: 525-4000

Bibliographic information:
Einar Baldur Þorsteinsson, 2025, *Growth and characterization of Mn-based magnetic MAX phases*, Ph.D.Thesis, Faculty of Science, University of Iceland, 122 pp.

Author ORCID: 0000-0002-4224-3241
ISBN: 978-9935-9826-6-7

Printing: Háskólaprent
Reykjavik, Iceland, November 2025

Abstract

MAX phases are a family of naturally nanolaminated materials, with the chemical formula $M_{n+1}AX_n$, the most common being M_2AX. Traditionally they are composed of a transition metal (M), an A-group element (A), and either carbon or nitrogen (X). However in recent years, the elements available at each site have been expanding as new phases continue to be discovered. The basic structural ordering of M_2AX is distinct layers of elements with the order M-A-M-X-M-A-M-X. In this thesis the MAX phase Mn_2GaC is used as a base material to branch out from by substituting manganese (Mn) with chromium (Cr), iron (Fe) and scandium (Sc), with the aim of investigating the magnetic properties of the resulting compounds.

The magnetic properties of epitaxially grown Mn_2GaC thin films on $MgO(1\,1\,1)$ are studied, where the low-temperature magnetization at 5 T field is not found to change significantly with temperature, contradicting the existing literature. This is found to stem from insufficient subtraction of the large non-linear MgO substrate background signal. Investigations into the magnetic anisotropy of Mn_2GaC using two films with different crystal growth orientations, find that the $(0\,0\,0\,l)$ crystallographic planes are magnetic easy planes. Scandium is used to obtain a different chemical ordering from the standard MAX phase, referred to as an *i*-MAX phase, which has an additional kagome-like in-plane ordering. This is formed when 1/3 of the Mn is substituted for Sc, forming $(Mn_{2/3}Sc_{1/3})_2GaC$. The films are grown epitaxially on $MgO(1\,1\,1)$, $Al_2O_3(0\,0\,0\,1)$ and SiC-$4H(0\,0\,1)$ substrates, with SiC giving the highest crystal quality. The magnetic properties of this phase are investigated and it is found to be antiferromagnetic.

Substituting Cr for Mn, forming $(Mn_{1-x}Cr_x)_2GaC$ with $x \leq 0.29$, results in a significant ferromagnetic response at room temperature, with critical temperatures reaching up to 489 K. The strongest moment measured was at $x = 0.12$, with a saturation magnetization and remanent magnetization

of 370 kA/m and 176 kA/m respectively, and a coercive field of 16.8 mT at room temperature. This is the first time a strong ferromagnetic response at and above room temperature is reported on for MAX phases, which is a significant milestone. The $(Mn_{1-x}Cr_x)_2GaC$ films are grown both epitaxially on $MgO(1\,1\,1)$ substrates and polycrystalline textured on Si/SiO_2 substrates, both resulting in similar magnetic properties. This opens up the possibilities of utilizing them in practical applications.

Investigating the solid solution of $(Mn_{1-x}Fe_x)_2GaC$, for $0.05 \leq x \leq 0.38$, shows that Fe seems to successfully integrate into the MAX phase according to x-ray measurements. However, even for the lowest concentration of $x = 0.05$, a large amount of the antiperovskite phase $(Mn,Fe)_3GaC$ is also formed. The addition of Cr to make $(Mn_{1-x-y}Fe_xCr_y)_2GaC$, has a stabilizing effect on the MAX phase, allowing almost a phase pure $x = 0.11$, $y = 0.21$ sample to be synthesized with only a trace of the antiperovskite competing phase appearing. This sample has similar magnetic characteristics to a Cr $y = 0.29$ sample with no Fe, however with a slightly lower critical temperature.

Ágrip

MAX fasar eru fjöldskylda af atómlagskiptum efnum, með efnaformúluna $M_{n+1}AX_n$, þar sem algengasta útgáfan er M_2AX. Hefðbundin samsetning er með hliðarmálmi (M), frumefni úr A-hópi (A), og annað hvort kolefni eða nitri (X) og í M_2AX fasa raða frumefnin sér í aðgreind atómlög í röðinni M-A-M-X-M-A-M-X. Á undarförnum árum hefur úrval frumefna sem geta verið í hverju sæti aukist samhliða því að nýjar efnasamsetningar hafa uppgötvast. Í þessari ritgerð verður MAX fasinn Mn_2GaC notaður sem grunnur til að útvíkka í aðrar samsetningar með því að skipta út mangani (Mn) fyrir króm (Cr), járn (Fe) og skandín (Sc). Markmiðið er að rannsaka seguleiginleika þessara nýju MAX fasa.

Seguleiginleikar einkristallaðra Mn_2GaC húða á MgO$(1\,1\,1)$ undirlagi eru rannsakaðir sérstaklega við lág hitastig. Við sjáum að seglun við 5 T svið breytist aðeins lítilega með hitastigi, gagnstætt við áður birtar vísindagreinar. Ástæðan fyrir þessum mismun er ófullnægandi frádráttur á ólínulega bakgrunninum frá MgO undirlögunum. Mælingar á segulmisáttun í tveimur Mn_2GaC sýnum með mismunandi kristalstefnum sýna að $(000l)$ kristalplönin eru auðseglandi. Skandín er svo notað til að breyta efnisuppröðuninni frá stöðluðum MAX fasa, yfir í svo kallaðan *i*-MAX fasa, sem hefur kagome atómuppröðun í plani sýnisins til viðbótar við lagskiptinguna. Þessi uppröðun myndast ef 1/3 af Mn er skipt út fyrir Sc, sem gefur efnajöfnuna $(Mn_{2/3}Sc_{1/3})_2GaC$. Þessar húðir eru ræktaðar sem einkristallar á MgO$(1\,1\,1)$, Al_2O_3 $(0\,0\,0\,1)$ og SiC-4H$(0\,0\,1)$ undirlög, þar sem SiC gefur bestu gæðin á kristalnum. Seguleiginleikar þessa fasa eru rannsakaðir og niðurstaðan er að hann er andjárnsegull.

Með því að skipta út Mn fyrir Cr til að mynda $(Mn_{1-x}Cr_x)_2GaC$ með $x \leq 0{,}29$, þá fæst töluverð járnseglandi svörun við stofuhita, og Curie hitastig sem nær upp í 489 K. Sterkasta merkið fæst við $x = 0{,}12$, með 370 kA/m mettunarseglun, 176 kA/m segulleif, og afseglunarsvið upp á 16,8 mT við stofuhita. Þetta er í fyrsta skipti sem sterk járnseglandi svörun fæst við eða yfir stofuhita í MAX fasa, sem markar stór tíma-

mót. $(Mn_{1-x}Cr_x)_2GaC$ húðirnar voru ræktaðar bæði sem einkristallar á $MgO(1\,1\,1)$ undirlög og fjölkristallar á Si/SiO_2 undirlög, sem bæði skila svipuðum seguleiginleikum. Þetta opnar á frekari möguleika til hagnýtingar á seglandi MAX fösum.

Rannsóknir á efnablöndunni $(Mn_{1-x}Fe_x)_2GaC$, með $0{,}05 \leq x \leq 0{,}38$, sýna að Fe virðist fara inn í MAX fasann samkvæmt röntgenmælingum. Aftur á móti kemur í ljós að jafnvel fyrir minnsta magnið $x = 0{,}05$, þá myndast antiperovskite fasinn $(Mn_{1-x}Fe_x)_3GaC$. Með því að bæta við Cr og mynda $(Mn_{1-x-y}Fe_xCr_y)_2GaC$, þá eykst stöðugleiki MAX fasans, sem gefur nánast fasahrein sýni með $x = 0{,}11$, $y = 0{,}21$ og einungis snefil af antiperovskite fasanum. Þetta sýni hafði sambærilega seguleiginleika á við sýni með Cr $y = 0{,}29$ og engu járni, en það var með aðeins lægra Curie hitastig.

Table of Contents

List of Publications

Paper I:

E.B. Thorsteinsson, A. S. Ingason, F. Magnus, Magnetic ordering and magnetocrystalline anisotropy in epitaxial Mn_2GaC MAX phase thin films. 2023, *Physical Review Materials*, Vol. 7, Issue 3, 034409. Accessed at `https://doi.org/10.1103/PhysRevMaterials.7.034409`.

My contributions: Synthesized the samples, performed all measurements, carried out all data analysis and co-authored the paper.

Paper II:

E.B. Thorsteinsson, M. Dahlqvist, A. Elsukova, A. Petruhins, P. O. Å. Persson, J. Rosen, A. S. Ingason, F. Magnus 2023, Room temperature ferromagnetism in the nanolaminted MAX phase $(Mn_{1-x}Cr_x)_2GaC$. *APL Materials*, Vol. 11, , 121102. Accessed at `https://doi.org/10.1063/5.0176571`.

My contributions: Synthesized the sample, performed all measurements except TEM, carried out data analysis and co-authored the paper.

Paper III:

E.B. Thorsteinsson, M. Dahlqvist, A. Elsukova, A. Petruhins, P. O. Å Persson, J. Rosen, A. S. Ingason, F. Magnus, 2025, Growth and magnetic properties of epitaxial thin films of the i-MAX phase (Mn2/3Sc1/3)2GaC. *Vacuum*, Vol. 233, 113856. Accessed at `https://doi.org/10.1016/j.vacuum.2024.113856`.

My contributions: Synthesized the sample, performed all measurements except TEM, carried out data analysis and co-authored the paper.

Paper IV:

E.B. Thorsteinsson, D. Dagbjartsson, A. S. Ingason, F. Magnus, 2025, Ferromagnetism at room temperature in Cr-doped polycrystalline Mn_2GaC MAX phase thin films. *Applied Physics Letters*, Vol. 127, 052408. Accessed at https://doi.org/10.1063/5.0279839.

My contributions: Synthesized the samples, performed X-ray pole figures, partially did VSM measurements and co-authored the paper.

Other publications not included or discussed in this thesis, but published during the time period of the thesis.

Paper V:

E.B. Thorsteinsson, S. Shayestehaminzadeh, U. B. Arnalds, 2018, Tuning metal-insulator transitions in epitaxial V_2O_3. *Applied Physics Letters*, Vol. 112, 161902. Accessed at https://doi.org/10.1063/1.5023180.

Paper VI:

D-S Park, G. J. Rees, H. Wang, D. Rata, A. J. Morris, I. V. Maznichenko, S. Ostanin, A. Bhatnagar, C-J Choi, R. D. B. Jónsson, K. Kaufmann, R. Kashtiban, M. Walker, C-T Chiang, **E.B. Thorsteinsson**, Z. Luo, I-S Park, J. V. Hanna, I. Mertig, K. Dörr, H. P. Gíslason, C.s F. McConville, 2018, Electromagnetic functionalization of wide-bandgap dielectric oxides by boron interstitial doping. *Advanced Materials*, Vol. 30, 1802025. Accessed at https://doi.org/10.1002/adma.201802025.

Paper VII:

B. Qi, H.P. Gunnlaugsson, S. Ólafsson, H.P. Gislason, **E.B. Thorsteinsson**, U. B. Arnalds, R. Mantovan, I. Unzueta l, D.V. Zyabkin, K.Bharuth Ram, K. Johnston, P.B. Krastev, T.E. Mølholt, H. Masenda, A.Tarazaga Martín-Luengo, D. Naidoo, J. Schel, 2020, Metal-insulator transition in crystalline V_2O_3 thin films probed at atomic-scale using emission Mössbauer spectroscopy. *Thin Solid Flims*, Vol. 714, 138389. Accessed at https://doi.org/10.1016/j.tsf.2020.138389.

Paper VIII:

E.B. Thorsteinsson, S. Shayestehaminzadeh, A. S. Ingason, F. Magnus, U. B. Arnalds, 2021, Controlling metal–insulator transitions in reactively sputtered vanadium sesquioxide thin films through structure and stoichiometry. *Scientific Reports*, Vol. 11, 6273. Accessed at `https://doi.org/10.1038/s41598-021-85397-x`.

Paper IX:

H. Hajihoseini, **E.B. Thorsteinsson**, V. V. Sigurjonsdottir, U. B. Arnalds, 2021, Strained interface layer contributions to the structural and electronic properties of epitaxial V_2O_3 films. *Applied Physics Letters*, Vol. 118, 161602. Accessed at `https://doi.org/10.1063/5.0043941`.

Paper X:

M. T. Sultan, K. Ignatova, **E.B. Thorsteinsson**, F. Magnus, U. B. Arnalds, 2021, Structural and electrical properties of V_2O_3 thin films on c-plane Al2O3 fabricated by reactive-HiPIMS and dcMS techniques. *Journal of Physics D: Applied Physics*, Vol. 54, 425302. Accessed at `https://doi.org/10.1088/1361-6463/ac1463`.

Paper XI:

M. T. Sultan, K. Ignatova, **E.B. Thorsteinsson**, U. B. Arnalds, 2022, Structural morphology and electrical transitions of V2O3 thin films grown on SiO2/Si by high power impulse magnetron sputtering. *Thin Solid Films*, Vol. 742, 139048. Accessed at `https://doi.org/10.1016/j.tsf.2021.139048`.

Paper XII:

K. A. Thórarinsdóttir, N. Strandqvist, V. V. Sigurjónsdóttir, **E.B. Thorsteinsson**, B. Hjörvarsson, F. Magnus, 2022, Finding order in disorder: Magnetic coupling distributions and competing anisotropies in an amorphous metal alloy *APL Materials*, Vol. 10, 041103. Accessed at `https://doi.org/10.1063/5.0078748`.

Paper XIII:

K. Ignatova, **E.B. Thorsteinsson**, B. A. Jósteinsson, N. Strandqvist, C. Vantaraki, V. Kapaklis, A. Devishvili, G K Pálsson U. B. Arnalds, 2022, Reversible exchange bias in epitaxial V2O3/Ni hybrid magnetic heterostructures. *Journal of Physics: Condensed Matter*, Vol. 34, 495001. Accessed at `https://doi.org/10.1088/1361-648x/ac9946`.

Paper XIV:

K. Ignatova, **E.B. Thorsteinsson** U. B. Arnalds, 2024, Angular-dependent magnetic properties in V2O3/Ni hybrid heterostructures. *Journal of Physics: Condensed Matter*, Vol. 34, 495001. Accessed at `https://doi.org/10.1088/1361-648x/ac9946`.

Acknowledgements

I want to thank my supervisor Friðrik Magnus for all the help and guidance over these years. Especially for the help and regular weekly meetings during the past two years of writing papers and this thesis, which has been a slow, difficult process for me, but now it is finally finished.

I also want to thank Sveinn Ólafsson for his assistance and support over the past three years, enabling me to continue with this work.

I would also like to thank the other professors Unnar, Einar Örn, Snorri. I could always ask for assistance if something came up.

I would be remiss if I did not thank Árni, for his insight into MAX phases and all things X-ray related.

Also want to thank Mohammad who taught me all about sputtering and x-ray measurements back in 2014.

There is also Kristján to thank, who has helped me when I was machining components in the workshop, and has helped whenever equipment has been misbehaving or broken.

Finally other colleagues in VR3, Kristbjörg, Kibbi, Taha, Kristina, Ásgeir, Arnar and more that have come and gone over the years.

1 Introduction

MAX phases as a family of materials have come under increasing focus over the past 30 years, with rapid discoveries of new phases over the last 15 years. To date, there are roughly 350 confirmed phases, of which close to 150 have been discovered in the past 5 years alone [1]. MAX phases refer to a group of materials that have naturally nanolaminated atomic layers with a specific order, the most basic of which has the order M-A-M-X-M-A-M-X and the chemical formula M_2AX. Traditionally M is a transition metal, A is an A-group element, and X is either carbon or nitrogen. However, with the influx of newly discovered MAX phases, the range of elements in each of the M-, A-, and X-sites has expanded considerably [1].

What makes MAX phases an interesting group of materials is their characteristic of exhibiting both the behavior of metals and ceramics, which makes them suitable under various conditions [2, 3]. The metallic attributes include good electrical and thermal conductivity, them being easily machinable, relatively soft, and not susceptible to thermal shock, as well as having plastic behavior at higher temperatures. MAX phases are also resistant to oxidation, are refractory and maintain their strength at high temperatures like ceramics. Another benefit of the MAX phases is that they are often of lower density than comparable metal alloys, giving them a further advantage over conventional materials. In addition, they are used as precursors to MXenes, where the A layer is etched away, resulting in two-dimensional materials with M-X-M structures, with exceptional properties [4–7]. After the discovery of the first magnetic MAX phase in 2013, there have been numerous attempts to produce magnetic MAX phases that exhibit strong or interesting magnetic behavior above room temperature. However, this has not been easy because there are several challenges that have limited the success in synthesizing such a phase.

The main focus of this thesis is the study of the Mn_2GaC MAX phase and

its derivatives by substituting Mn with other elements. Mn_2GaC exhibits interesting magnetic behavior where it has a ferromagnetic-like response below 210 K, and above, it transitions to antiferromagnetic behavior with a metamagnetic transition at higher field values. It has also been shown that the magnetic properties of Mn_2GaC are sensitive to changes in the *c* lattice parameter [8]. Therefore, introducing other elements into it by substituting the Mn atoms and looking at the change in magnetic response is an interesting line of research. Indeed, we find that substituting with Cr, Sc, or Fe fundamentally alters the magnetic interactions with important consequences for the magnetic ordering.

1.1 Organization of the thesis

The contents of the thesis are organized as follows. Chapter 2 gives a brief overview of the fundamentals of magnetism, describing different magnetic ordering, what magnetic anisotropy is, and how basic magnetic measurements are performed. Chapter 3 briefly covers the history of MAX phases and the different types of MAX phases that have emerged over time. It then gives an overview of the current state of research on magnetic MAX phases, with a focus on Mn and Cr containing phases. Chapter 4 lists the experimental methods and equipment used for the work in the thesis, as well as the sample synthesis process. Chapter 5 gives an overview of the main results of the papers, including the reasoning and processes behind the research. Some unpublished results are also presented. Chapter 6 gives conclusions and an outlook for potential future work. Chapter 7 has the attached papers that serve as the basis for this thesis.

2 Magnetism in materials

This section gives a brief overview of magnetism and magnetic ordering. Magnetism is one of the cornerstones of modern technology. It is the basis for magnetic storage such as hard drives, used in electric motors, and most power generation methods rely on the rotation of turbines and magnets to generate electricity. Magnetism has its origin from two sources. Firstly, the movement of electric charges, such as electric current or the motion of an electron around an atom. Secondly, the quantum mechanical spin of particles, which includes electrons, neutrons, and more. Spin here refers to angular momentum of these particles, which can be thought of in classical terms as if they were spinning around their own axis.

An external magnetic field can be generated by an electric current flowing through a wire in an electromagnet or by using a permanent magnet. The interaction between a magnetic moment and an external field is not always simple. The field will exert a force to align the moment parallel to the field, however, if it is not a single magnetic moment in a vacuum but instead it is surrounded by other moments in a material, then the response will be modified by the exchange interaction between neighboring moments. When many magnetic moments come together they can form a number of different magnetic orderings with different responses to an external field.

The resulting magnetization M from an external field is described with the equation,

$$M = \chi \cdot H \tag{1}$$

where H is the external field and χ is the magnetic susceptibility. Magnetic susceptibility describes the response of the magnetic moments to an external field. If χ is negative, the moments tend to align antiparallel to the applied field, and the material is diamagnetic. When the susceptibility is positive, the moments tend to align parallel with the applied field and

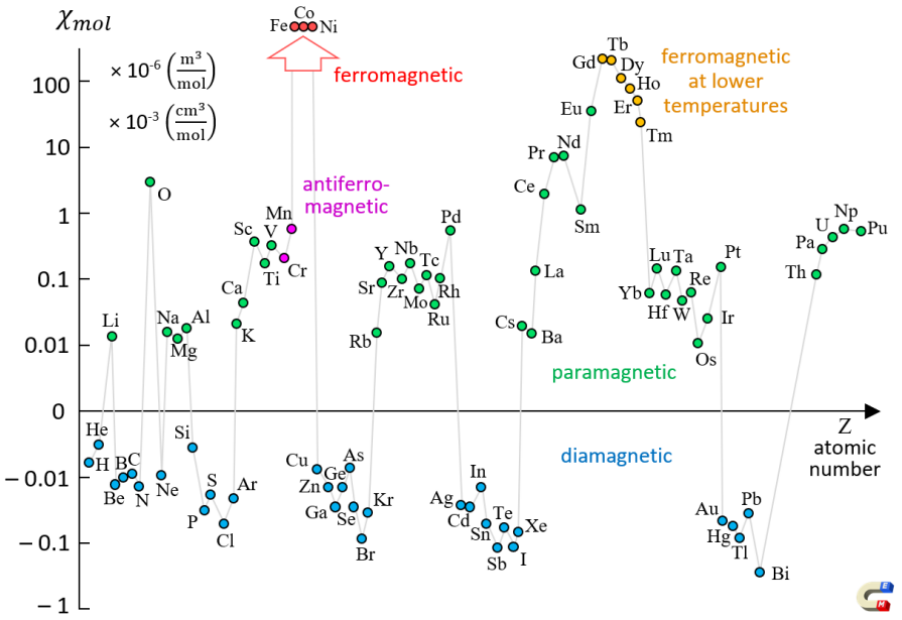

Figure 2.1. Molar magnetic susceptibility of chemical elements at room temperature. Reproduced from Encyclopedia Magnetica [9] by CC-BY-4.0 license.

the material is usually paramagnetic. Figure 2.1 shows the molar magnetic susceptibility of the elements. It can be seen that most materials are either dia- or paramagnetic, however, not all elements fall into those two categories. A more complex response occurs in a few elements which is the result of spontaneous magnetic ordering. Iron, cobalt, and nickel are ferromagnetic at room temperature, while chromium is antiferromagnetic. These orderings will be explored in more detail in the following sections.

2.1 Dia- and paramagnetism

Diamagnetism (DM) is when an external field induces an internal field in the opposite direction causing the material to be repelled by it. This effect is present in all materials, but is generally weak resulting in minor contributions to the total signal if other magnetic effects are present. In a classical approach, it can be thought of as originating from induced electrical current in the orbital motion of electrons by the external field,

producing a magnetic field in the opposite direction. The true origin, however, is quantum mechanical, as this occurs in materials with filled electron shells where the total spin and orbital angular momentum of the electrons is zero, $J = 0$. This results in no magnetic moment within a first order perturbation theory. This is therefore a common effect in materials that have their outer electron shells filled or compounds with ionic bonds. An example would be NaCl, as the Na and Cl complement each other, with the Na giving its free electron to the Cl, resulting in it having a filled outer electron shell. Although common in these types of compound materials, it is not a general rule. The effects of diamagnetism are largely temperature independent.

Paramagnetism (PM) is when electron spins weakly align with an external field, making the material slightly magnetic while exposed to an external field. This effect originates from unpaired electrons in the outer electron shell of the material. When there is no external field applied, the spins from these unpaired electrons have random orientations as a result of thermal motion. When an external field is applied it will align some of the spins with the field while thermal motion keeps most of them randomized. As a larger and larger field is applied, more of the spins align with it, causing a linear increase in the magnetization of the material. The removal of the external field causes all the spins to revert back to random orientations, therefore, without an external field the material is non-magnetic.

The temperature dependence of paramagnetic susceptibility follows Curie's law, given by the equation,

$$\chi = \frac{C}{T} \tag{2}$$

where C is the material specific Curie constant and T is the temperature. The temperature dependence of the susceptibility of paramagnets and diamagnets and can be seen in Figure 2.2.

2.2 Exchange interactions

How magnetic ordering comes about is a complex set of interactions between the electron orbitals in neighbouring and close by magnetic

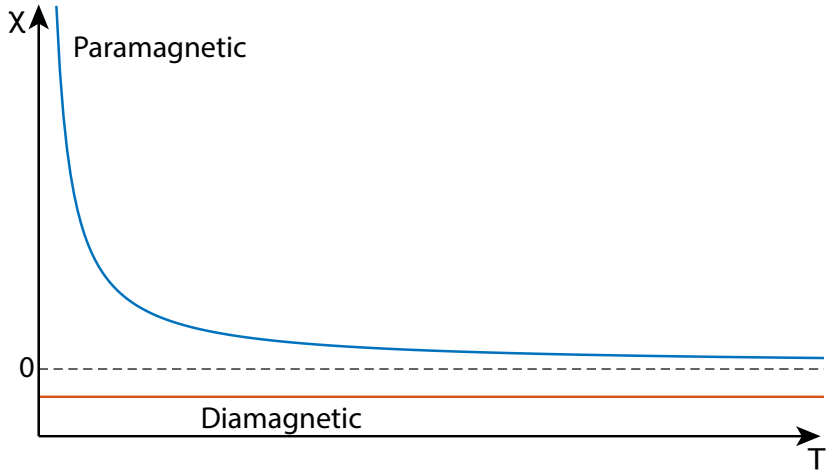

Figure 2.2. Susceptibility of dia- and paramagnetism as a function of temperature. The temperature dependence of paramagnetism follows Curie's law, while diamagnetism is temperature independent.

atoms. As with so many physical phenomena, magnetic ordering is the result of when nature looks to minimize the total energy of the system. The exchange energy, E_{ex}, between two spins i and j is given by the equation,

$$E_{ex} = -2J_{ex}\mathbf{S}_i\mathbf{S}_j = -2J\mathbf{S}_i\mathbf{S}_j \cdot \cos(\phi) \tag{3}$$

where J_{ex} is the exchange integral between the spins $\mathbf{S}$ while ϕ is the angle between the spins [10].

To minimize the energy, we have two cases. When J_{ex} is positive, the system favors parallel spins with $\cos(\phi) = 1$ whereas when J_{ex} is negative, the system will favor antiparallel spins with $\cos(\phi) = -1$. It can then be seen that when J_{ex} is positive there will be spontaneous alignment of spins resulting in a magnetized material without the need for external field, resulting in what is called ferromagnetic behavior. On the other hand, when when J_{ex} is negative, antiferromagnetism results.

If the exchange integral J_{ex} is looked at as a function of r_a/r_{3d}, where r_a is the atomic radius and r_{3d} is the orbital radius of 3d electrons, a trend can be seen for common transition metal elements [12, 13]. This is known as the Bethe-Slater curve and is shown in figure 2.3. Here the ferromagnetic elements Fe, Ni and Co fall nicely above the line, as

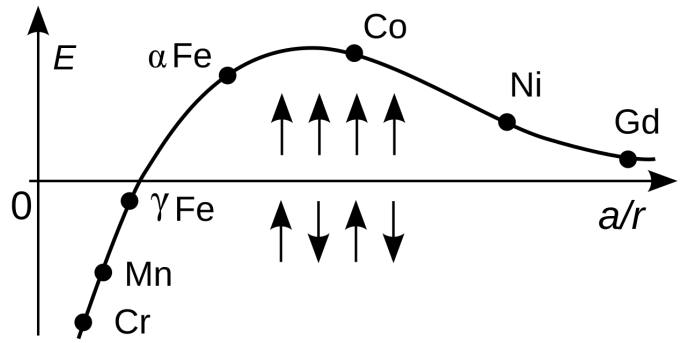

Figure 2.3. The Bethe-Slater curve, showing the exchange energy as a function of atomic radius for some elements. By Zurek S. [11] CC0 Licence, via Wikimedia Commons.

their magnetic behavior does originate from spins of 3d electrons. The Bethe-Slater curve can be used to give an indication of whether a material might be ferromagnetic and works well in alloys. This behavior can also hold for ferromagnetic amorphous materials which have no long-range ordered crystal structure and highlights that magnetic behavior is highly dependent on atomic distances and electron orbitals, as this changes the exchange interaction that occurs between the spin of the particles [14].

The nature of the exchange interaction is further categorized into direct and indirect exchanges [15]. Direct exchange is where electrons of neighbouring atoms interact directly without an intermediary, requiring the atomic orbitals of the electrons to overlap. The resulting interaction can be either ferromagnetic or antiferromagnetic. This mode for interaction can be limited, for example the 4f electrons in rare-earth metals are strongly localized around the atom, making it harder for them to participate in direct exchange.

Then there is indirect exchange, or often called superexchange, where two non-neighbouring magnetic atoms do not interact directly but rather across a non-magnetic intermediary atom. The unpaired electrons on the magnetic atoms are then free to move between all the atoms instead of remaining localized to their magnetic atom. This generally leads to antiferromagnetic behavior stemming from the Pauli exclusion principle, as anti-parallel spins have more permitted locations than parallel spins.

Another type of indirect exchange in metals is the RKKY interaction (named after Ruderman, Kittel, Kasuya and Yoshida). In this case a conduction band electron gets polarized with a certain spin orientation from a magnetic atom, this electron then moves in the conduction band and couples to another magnetic atom some distance away, causing it to get aligned to the itinerant electron. This effect depends on the distances between atoms and has oscillatory behavior.

Anisotropic exchange interaction, or Dzyaloshinsky-Moriya interaction is where the spin-orbit interaction takes the place of the non-magnetic atom from the superexchange. The exchange interaction is between the excited state of one ion with the ground state of another ion. This is also affected by the crystal anisotropy of the material, where the spins will seek to align perpendicular to the crystal field. This effect causes the spins to cant slightly and can occur in antiferromagnets causing a small ferromagnetic signal.

2.3 Magnetic ordering

2.3.1 Ferromagnetism

Ferromagnetism (FM) is when all magnetic moments in a material align spontaneously in the same direction, even without an external field. This occurs due to the alignment of the spins being the lowest energy state of the exchange interaction in materials that have a positive J_{ex} as mentioned in the previous section. This spontaneous alignment depends on the temperature of the material. At low temperatures the spins are aligned, but as the temperature is raised, thermal motion of the atoms and electrons in the material will gradually overcome the internal ordering from the exchange interactions and cause the magnetic moments to eventually point in randomized directions. This can be seen in Figure 2.4. The temperature at which the material enters this disordered state and becomes a paramagnet is called the Curie temperature or critical temperature. If a material that is above the critical temperature is cooled below it, the ordering is reestablished and the material will become magnetized even in the absence of an external field. This spontaneous magnetization is what defines ferromagnetism. The critical temperature is dependent on the material and the strength of the exchange interaction. Only three

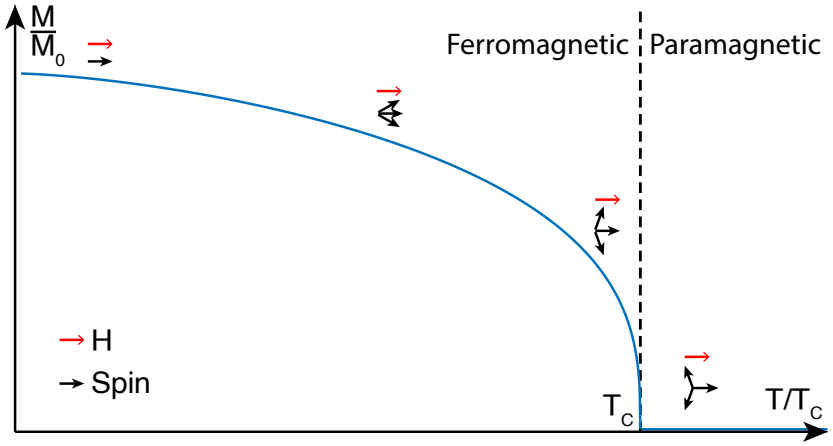

Figure 2.4. Temperature dependence of the magnetization of a ferromagnet. As the temperature is increased, the thermal motion in the spins is increased, eventually causing a transition to a paramagnetism with disordered orientations.

elements have a critical temperature above room temperature in their pure form, namely iron, cobalt, and nickel. However, there are a number of alloys and other materials that exhibit ferromagnetism at and above room temperature.

The temperature dependence of the magnetization M relative to the magnetization at zero temperature, M_0, for ferromagnets can be described with power laws. This can be seen in Table 2.1 and Figure 2.4. At low temperatures it follows Bloch's law [16] with $T^{3/2}$. While approaching the critical temperature T_C from below it follows $(T_C - T)^{\beta}$, where β is the critical exponent, for a mean field approximation it has the value $\beta = 1/2$ but other models are closer to $\beta = 1/3$. When around T_C, the magnetization follows the external field H with $H^{1/3}$. Above the T_C it follows the Curie-Weiss law with $(T - T_C)^{-1}$ [15].

In practice, macroscopic ferromagnetic materials may not exhibit magnetization in the absence of an applied field due to internal magnetic domain structure. Although all spins in a ferromagnet will align themselves with their neighbours, to lower the overall energy in the system they often form domains of magnetic moments each pointing in a direction, sometimes canceling out the overall magnetization of the material. If a sufficiently

Table 2.1. Temperature dependence of the magnetization of a ferromagnet around the Curie temperature

Low T	$M/M_0 \propto T^{3/2}$	Bloch's Law
$T << T_C$	$M/M_0 \propto (T_C - T)^{\beta}$	$\beta \approx 1/2$
$T \approx T_C$	$M/M_0 \propto H^{1/3}$	
$T > T_C$	$M/M_0 \propto H(T - T_C)^{-1}$	Curie law

strong external field is applied, it can fully overcome the internal domain structure in the material, causing all the moments to be truly aligned in the same direction, reaching the saturation magnetization of the material. As the external field is removed, some domain structure might reform, but the majority will maintain their alignment, this is called the remanent magnetization of the material. The remanence of a ferromagnet is what makes them permanent magnets. It is not necessary to fully saturate a material to achieve a remanent magnetization, generally just a small field suffices. However, the resulting remanence would be correspondingly smaller than if fully saturated, as fewer domains will have been aligned. This remanent field can also be removed or reversed by applying an opposing external field, thus causing the domains to reorient themselves to neutralize the overall magnetization. More details about this will be given in section 2.5, where the hysteresis of a ferromagnet will be described.

As all of the spins are aligned in ferromagnetic materials, they have a much higher susceptibility than dia- or paramagnets, making them highly effective in applications. Ferromagnetic materials are one of the cornerstones of modern technology, including magnetic materials in hard drives, electrical motors and generators.

2.3.2 Antiferromagnetism

Antiferromagnetism (AFM) is when the spins of atoms align with their neighbours but in antiparallel manner, thus canceling out any net moment or stray field. This is the lowest energy state for materials with a negative exchange interaction J_{ex}. These antiparallel spins are located on two different sub-lattices, where one sub-lattice points in one direction while the other sub-lattice points the opposite way. Antiferromagnets also have a critical temperature analogous to the Curie temperature, known as the Néel temperature. Above this temperature, they become paramagnets as

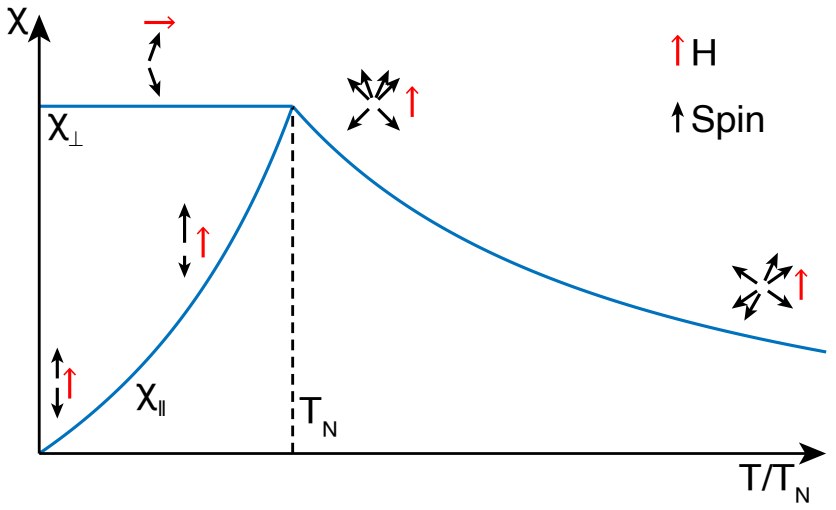

Figure 2.5. Temperature dependence of an antiferromagnet.

a result of thermal motion. Due to the net-zero moment, antiferromagnets respond much more weakly to an applied field than ferromagnets, which is seen as a much smaller magnetic susceptibility. Nonetheless, the susceptibility has a characteristic dependence on temperature which also depends on the orientation of the field with respect to the spin sublattices. Therefore, susceptibility measurements can be used to identify antiferromagnets, despite their weak interaction with an applied field. The temperature dependence of the susceptibility is shown in Figure 2.5.

The interactions of antiferromagnets with an external field are more complex than for ferromagnets. The direction of the applied field is important, whether parallel or perpendicular to the spins. The field strength is also a factor, wether it is a weak or strong external field that is applied. If we first consider the effects of a weak external field applied perpendicular to the aligned spins, then both spins will cant towards the field, causing a small net magnetization. The susceptibility will remain independent of temperature up to the Néel temperature, as both spins are affected equally by the temperature and the field. In the parallel case, at low temperatures both spins are in a saturated state opposing each other. However, as the temperature is raised, the external field is working against one spin and together with the other, causing the effective signal to slowly align more with the external field.

Now, if the external field is stronger, then for the perpendicular case, the spins will simply tilt more and more along the direction of the field. This is a linear effect until the external field is strong enough to saturate the moments along the field, as seen in Figure 2.6 (a). However, for the parallel case, it is more complex. Initially, the response is similar to that for the small field, but as the field strength increases, it will hit a critical point where the spin opposite to the field will suddenly reverse. The two spins will then have an angle θ between them while pointing in the field direction. As the field increases further, the angle θ will continuously decrease until both spins are saturated along the external field. This process is called a spin-flop transition and can be seen in Figure 2.6 (b). A special case is when there is strong anisotropy in the antiferromagnetic material, then instead of a spin-flop there is a spin-flip. A spin-flip is when the opposing spins spontaneously align at a critical field value instead of doing it as a function of field as in the spin-flop case, this is illustrated in Figure 2.6 (c). Spin-flop and spin-flip are a type of metamagnetic transition, which will be discussed more later.

Above the Néel temperature, the susceptibility of antiferromagnets is described by the Curie-Weiss formula,

$$\chi = \frac{C}{T - \theta} \tag{4}$$

a modified version of Curie's law, Eq. 2. Here θ is the Weiss temperature. For paramagnets $\theta = 0$, while $\theta > 0$ for ferromagnets and $\theta < 0$ for antiferromagnets.

This directional difference in applied field and response is used in the case of the antiferromagnetic MAX phases Mn_2GaC and $(Mn_{2/3}Sc_{1/3})_2GaC$ in papers I and III.

2.3.3 Ferrimagnetism

Ferrimagnetism (FiM) is similar to antiferromagnetism but has some characteristics of ferromagnetism. Here the magnetic sub-lattices do not fully cancel each other, thus resulting in a net magnetization. This can stem from different atomic species populating the sub-lattices (as in the case of rare-earth transition metal magnets) or antiparallel sub-lattices with different numbers of the same magnetic atom (as is for example the case in Mn intermetallic compounds such as MnGa). This

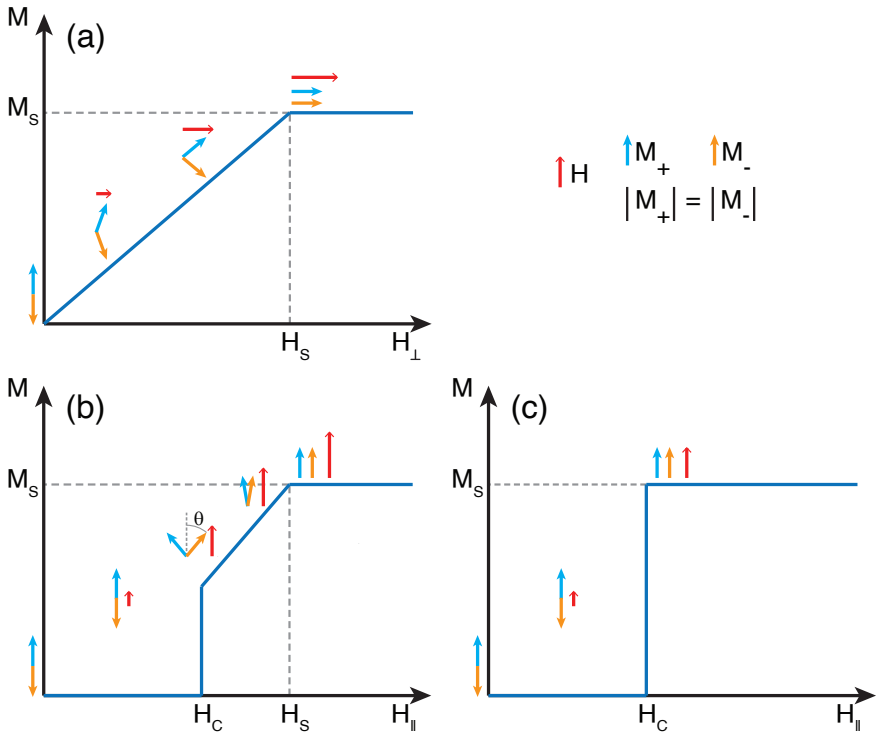

Figure 2.6. Schematic overview of spin-flop and spin-flip. (a) Field applied perpendicular to the spins, causing continuous canting until both spins point in the same direction, thus reaching saturation, M_S, at field value H_S. (b) Spin-flop, the spins remain antiparallel until a critical field H_C, when spin M_- flops over and both spins have angle θ to the external field. The angle θ decreases until saturation field H_S. (c) Spin-flip, with strong anisotropy present, the spins remain antiparallel until M_- flips at H_C, where both spins point in same direction in saturation.

results in a net positive remanent magnetization after the removal of an external field similar to that in ferromagnets. However, they have a more complex temperature dependence, as the two differing groups of spins can respond differently to temperature changes. Like ferromagnetic materials, ferrimagnetic materials also have a critical temperature at which they enter a disorder state and become paramagnets.

2.3.4 Helical ordering

Many types of magnetic ordering exist with more complex non-collinear arrangements of magnetic moments. One such arrangement is helical ordering, where magnetic moments are ferromagnetically aligned within layers, but each layer has its moment rotated by an angle θ with respect to the previous layer. If the interaction between layers is described by a nearest-neighbour exchange constant J_1 and next-nearest-neighbour exchange constant J_2, then the energy of the system can be written as [10]

$$E = -2NS^2(J_1 \cos\theta + J_2 \cos 2\theta) \tag{5}$$

where N is the number of atoms in each layer. The energy is minimized when $\partial E/\partial\theta = 0$, which gives

$$(J_1 + 4J_2 \cos\theta)\sin\theta = 0 \tag{6}$$

This results in on the one hand $\sin\theta = 0$, giving $\theta = 0$ or $\theta = \pi$ for ferromagnetic or antiferromagnetic ordering. On the other hand there is

$$\cos\theta = -\frac{J_1}{4J_2} \tag{7}$$

which gives the helical ordering. This will occur in ferro- or antiferromagnets when $J_2 < 0$ and $|J_1| < 4|J_2|$. The period of rotation can extend over multiple unit cells, making these magnetic structures quite large. As the magnetic moments rotate and complete a period, the net magnetic moments cancel each other out, resulting in no permanent magnetic moment. Therefore, helical ordering could be considered a complex form of antiferromagnetism. A visual representation can be seen in Figure 2.7, where a helical order with a repetition length of 16 (22.5° per plane) is illustrated.

There has recently been evidence that the magnetic ordering of the MAX phase Mn_2GaC is helical [17–19]. This applies to both below the transition temperature of 210 K, where there is ferromagnetic behavior observed, as well as above it, where there is antiferromagnetic behavior with a metamagnetic transition. The helical ordering has different angles θ for the low temperature and room temperature ordering. This is still not a full explanation of the magnetic behavior seen in Mn_2GaC, as the helical ordering does not explain the ferromagnetic response, which is theorized to originate from an additional canting of the magnetic moments.

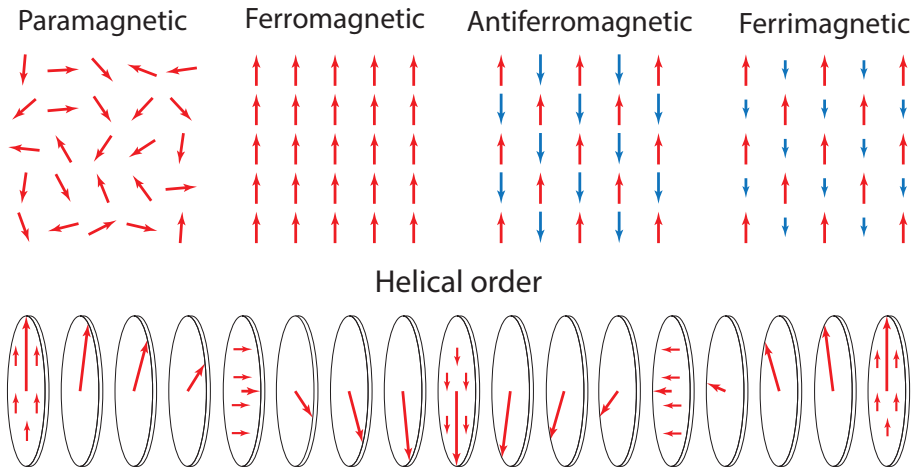

Figure 2.7. An overview of the alignment of magnetic moments in different orderings. Paramagnetic, where thermal motion randomly orients them. Ferromagnetic, where they are all aligned. Antiferromagnetic, two sub-lattices have moments oriented antiparallel to each other. Ferrimagnetic, similar to antiferromagnetic, except one of the sublattices has a smaller moment. Helical order, here different planes in the material have all their moments aligned, however each plane is offset by an angle with respect to the one before.

2.3.5 Metamagnetic transitions

A metamagnetic transition is a sudden transition from antiferromagnetic to ferromagnetic order in a material brought about by a change in the external field at a constant temperature [10]. That is, a small change in the external field can cause a large change in the magnetic state of the material by overcoming a critical energy barrier. Spin flips in antiferromagnets are a type of metamagnetic transition, when the spins suddenly align due to the external field. Figure 2.8 shows a metamagnetic transition in Mn_2GaC, where a high magnetic field causes a transition from an antiferromagnetic ordering to a non-collinear ferromagnetic ordering, which occurs above about 210 K and requires higher fields as the temperature is raised. An example of this is seen in paper I.

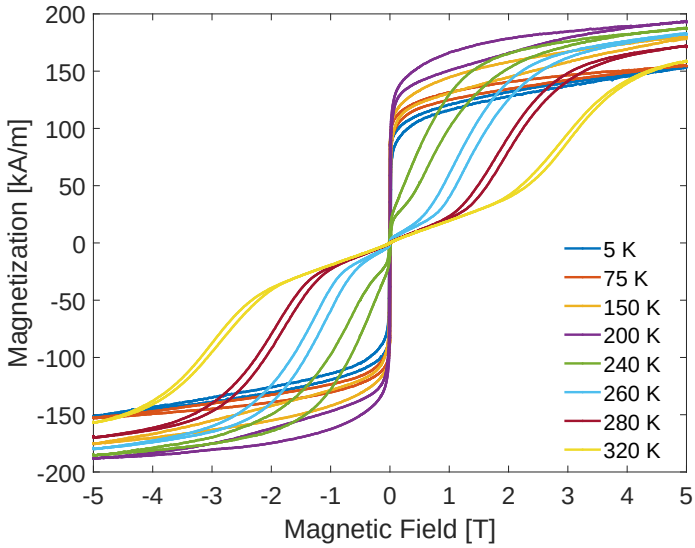

Figure 2.8. Examples of a metamagnetic transition in Mn_2GaC occurring above 200 K. The metamagnetic transition causes the phase to change from antiferromagnetic to ferromagnetic-like behavior with open hysteresis that move to higher fields as temperature is increased.

2.4 Magnetic anisotropy

In many magnetic materials the magnetic moments will preferably align along specific directions within the material and their response to an applied magnetic field will differ, depending on the direction of the field. This is known as magnetic anisotropy and it is a fundamental property of magnets, as well as being important in many applications. Several different factors can contribute to magnetic anisotropy. There is magnetocrystalline anisotropy, where the crystal lattice affects the moment and works to confine it to certain directions. Shape anisotropy results from non-spherical shapes of materials as that has a non-uniform effect on the demagnetizing field. Stress anisotropy is where tensile or compressive stress has an effect on the magnetic behavior of a material due to magnetoelastic coupling. The inverse of stress anisotropy is magnetostriction, where the effects of an external field aligning the spins causes distortions in the crystal lattice where the material experiences changes in length. Finally, exchange anisotropy is the interaction between ferromagnetic and antiferromagnetic materials, which causes a bias to be applied to the

field behavior of the materials. Here only magnetocrystalline and shape anisotropy will be explored further.

Magnetocrystalline anisotropy describes how magnetic materials have a preferred orientation for the spins relative to the crystal lattice. Along some crystal directions the material is easily magnetized, while along other directions a much larger external field is required. These are referred to as the easy and hard axis of a crystal. The easy direction of magnetization of a crystal is typically the direction of spontaneous domain magnetization in the demagnetized state [10]. That is, the domains lie in these directions and when an external field is applied along the easy axis, the domains in the field direction grow via domain wall motion at the expense of domains magnetized in other directions. The domain wall motion does not require a lot of energy and therefore fairly low fields can achieve this. In the case of magnetizing a sample along the hard axis, the field is no longer aligned with a single domain, and a combination of two domains favoring the external field direction grow by domain-wall motion. That only works up to a certain point, and as the field is further increased, the spins in the domains start to rotate. Eventually the domain walls are removed as the spins align with the field and the magnetization is saturated in the field direction. This is much more costly energy wise, as it needs to overcome the crystal anisotropy. The crystal anisotropy energy, E, can be described by.

$$E = K_0 + K_1 sin^2\theta + K_2 sin^4\theta + ... \tag{8}$$

Where K_i are constants that are material specific and θ is the angle between the field direction and crystal axis. K_0 is often ignored as it is independent of angle and the interest is generally related to finding the easy and hard axes, which depend on angle.

The origin of the crystal anisotropy is largely from spin-orbit coupling. The exchange interaction has its origin in spin-spin coupling, where the spins are either parallel or antiparallel, and is related to the angle between spins but independent from the crystal lattice. However, in the presence of spin-orbit coupling, as the external field tries to rotate the spin, it also has an effect on the electron orbit. The orbit of the electron is coupled to the lattice and resists the change in spin direction. The crystal anisotropy energy is the required energy to overcome this as the spin is oriented away from the easy axis.

Table 2.2. The orientation of the easy axis in a hexagonal system as a function of K_1 and K_2.

K_1 and K_2	Easy axis
$K_1 = K_2 = 0$	Isotropic
$K_1 > 0$ and $K_2 > -K_1$	c axis
$K_1 > 0$ and $K_2 < -K_1$	Basal plane
$K_1 < 0$ and $K_2 < -K_1/2$	Basal plane
$K_1 < 0$ and $K_2 > -K_1/2$	Easy cone

For a hexagonal system such as the MAX phases in this thesis, θ is the angle from the c axis. There are three main cases for the easy axis, it can be along the c axis, in the basal plane, or it can be in a form of an easy cone at an angle between 0° and 90°. This is determined by the constants K_1 and K_2, and the resulting cases can be seen in Table 2.2.

In thin films, shape anisotropy invariably plays an important role as it imparts another energy term to the demagnetizing energy

$$E = \frac{1}{2}\mu_0 M^2 \cos^2\theta \tag{9}$$

where θ is the angle between the film normal and M. This has the effect that it is energetically favorable for the magnetization to lie in the plane of the film. Thin films with a hexagonal crystal structure are often grown with the c axis perpendicular to the plane of the film, meaning that the film is $(000l)$ oriented. Then an in-plane easy axis refers to the basal plane, while out-of-plane would be the hard axis. This will be explored in paper I, where in the plane of the film there is a mix of both $(000l)$ and $(10\bar{1}3)$ planes. This gave us the opportunity to probe the easy axis of the MAX phase itself, independent of the shape anisotropy.

2.5 The magnetic hysteresis loop

There are many ways of characterizing magnetic materials experimentally, but perhaps the most fundamental is to measure the magnetic hysteresis loop. A hysteresis loop measurement is performed by sweeping the magnetic field and measuring the resulting magnetization in the material, typically along the same direction as the magnetic field is applied. An

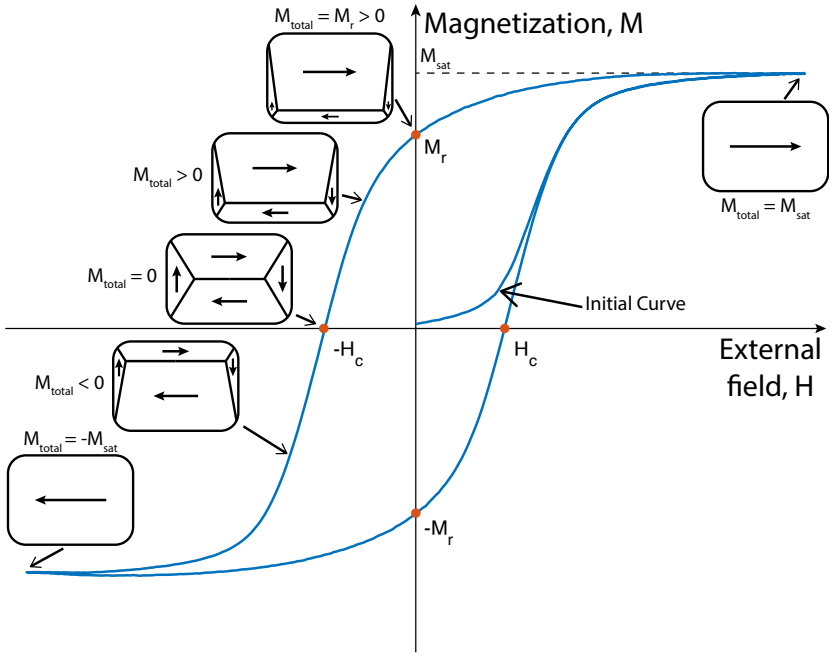

Figure 2.9. An example of a hysteresis curve of a ferromagnet.

example of a basic hysteresis loop in a ferromagnetic material is shown in Figure 2.9. If the material was initially in a demagnetized state, then as the field is ramped up in the positive direction, an initial curve is measured. If the applied field is strong enough, the material will reach saturation, M_s, where all magnetic moments are aligned along the field direction. As the field is decreased, the magnetization in the material will decrease as well; however, some of the aligned spins will retain their orientation as this is a lower-energy state. This will allow some magnetization to remain in the material even when the external field is removed and this is called the magnetic remanence of the material, M_r, making the material a magnet. If the external field is applied in the opposite (negative) direction, then it will start orienting those spins back to a neutral position, removing any remanence and the magnetization in the material returns to zero. The field required for this is called the coercive field, H_c. If the field continues past the coercive field, then the material can reach saturation in the opposite (negative) direction, and the hysteresis loop can be completed by returning again to saturation in the original positive direction.

A number of important parameters can be extracted from the hysteresis loop. The saturation magnetization can be obtained, allowing for calculations of the strength of the effective magnetic moment in the material. Measurements of remanent magnetization as a function of angle, both in-plane and out-of-plane, give information about the anisotropy in the material. The remanent magnetization is often normalized by dividing by the saturation magnetization to facilitate the comparison of the anisotropy of magnets with different strengths. The temperature dependence of the remanence is used to find the critical temperature of the material. The area contained within the hysteresis loop is related to the amount of energy expended to flip the spins. Therefore, the magnitude of the coercivity tells us how hard it is to flip the orientation of the spins. Sometimes it is desirable to have a large coercivity, such as in permanent magnets or magnetic recording media, these are often called hard magnets. While at other times it is desirable to have small coercivity for example in transformers, these are generally called soft magnets.

More complex information can also be extracted from the shape and slope of the hysteresis, and if multiple superimposed magnetic effects occur in the material, then the shape can become a lot more complex than the basic hysteresis shown in 2.9. The humble hysteresis loop is therefore a fountain of information regarding the magnetic properties of a material and is fundamental to all the work done in the four papers.

3 MAX phases

The work presented in this thesis is focused on a class of materials known as MAX phases. Their nanolaminated structure is described in section 3.1, together with a brief overview of the history of research into this unusual materials system. The magnetic properties of MAX phases are of central importance to this work, and a discussion of the various magnetic configurations which have been discovered over the past decade or so, can be found in section 3.2.

3.1 Overview of MAX phases

MAX phases are a family of materials composed of a transition metal (M), an A-group element (A) and either carbon or nitrogen (X) with the chemical formula $M_{n+1}AX_n$, with n ranging from 1 up to 6 [20, 21]. However, to date, no phase pure samples of $n > 3$ have been synthesized [1]. These materials naturally form a distinctive layered structure with highly anisotropic properties. The crystal structure is hexagonal, of space group P63/mmc. Figure 3.1 shows a view along the a-axis of the crystal structures for various ternary MAX phases, including some more complex orderings. For $n = 1$, or M_2AX, the crystal structure is composed of atomic layers with the order M-A-M-X-M-A-M-X. This is the structure that is the focus of this thesis, with Mn_2GaC serving as the base material. We then study solid solutions by partially substituting Mn with other elements. The details of the Mn_2GaC crystal structure will be described in section 3.2.2.

The first report of what would later become known as MAX phases was on Ti_2SC and Zr_2SC in 1960 by Helga Rohde and Heinz Kudielka [22]. However, the group by Hans Nowotny and coworkers pioneered the discovery of new phases during the period from late 1960 to 1969 and discovered close to 50 new materials. After this initial burst of dis-

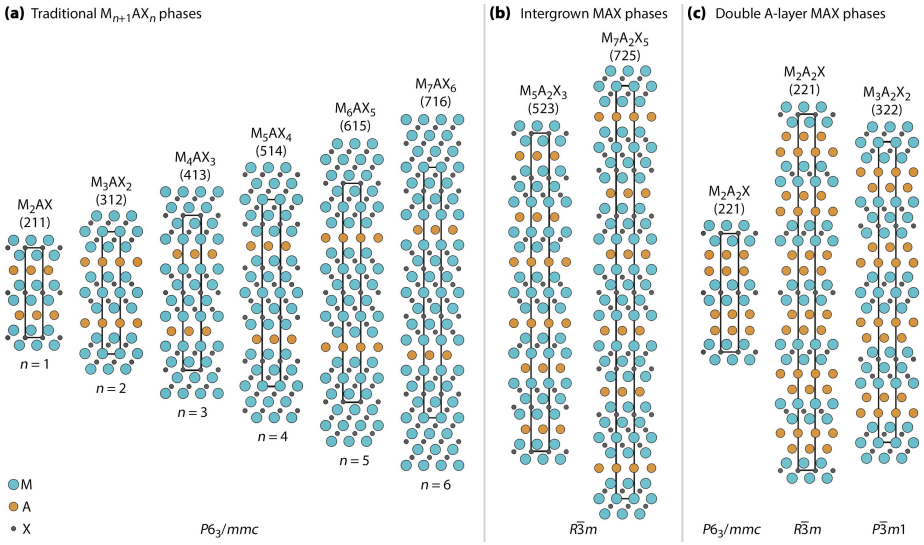

Figure 3.1. Crystal structures of several ternary MAX phases. (a) Traditional phases with a general $M_{n+1}AX_n$ composition, (b) hybrid MAX phases with alternating thickness of $M_{n+1}X_n$ layers, and (c) phases with a double A-layers. M elements are in blue, A in orange, and X in dark grey. All the MAX phases studied in this thesis are of the M_2AX type. Reproduced from Dahlqvist et al. [1] by a creative commons license.

coveries, interest in MAX phases remained low until 1996 when Michel W. Barsoum made high quality samples of Ti_3SiC_2 and highlighted the remarkable properties of this material, which combined attributes of both metals and ceramics [2]. The metallic attributes included good electrical and thermal conductivity, them being easily machinable, relatively soft, and not susceptible to thermal shock, as well as showing plastic behavior at high temperatures. The MAX phase was also resistant to oxidation, refractory and maintained its strength at higher temperatures like a ceramic. Another benefit of this material was that it had lower density than comparable metal alloys, giving it further advantage compared to conventional materials. Upon further investigation, it was realized that these attributes were shared with other MAX phase materials, igniting renewed interest in these novel material system in general.

Starting from the mid 2000s, reports of newly discovered MAX phases started growing rapidly, going from about 50 in 2000 to around 100 in

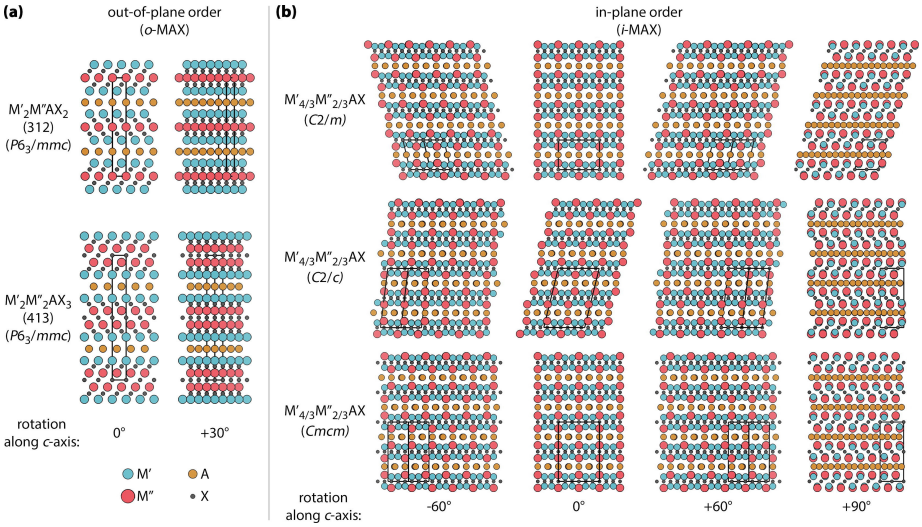

Figure 3.2. Crystal structures of chemically ordered MAX phases. (a) Out-of-plane ordered 312 and 413 o-MAX phases. (b) In-plane ordered i-MAX phase in three different space group representations, depending on the stacking sequence. Angles listed refer to rotation along c-axis to demonstrate the similarities and differences among the different i-MAX space groups. M' is in blue, M" in red, A in orange, and X in grey. Unit cells of each structure is marked by black lines. (Here M^1 and M^2 are denoted as M' and M"). Reproduced from Dahlqvist et al. [1] by a creative commons license.

2010, going over 200 in 2020 and exploding to 342 in 2024 [1]. Part of the rapid expansion of the MAX phase material family is due to the expansion of the material family beyond ternary materials. Ternary phases account for 124 out of 342, with solid solutions for 152 and chemical order with 66. For the solid solutions, all three sites, M, A, and X, have been successfully alloyed. Of the ones currently discovered, a bit more than half involve alloying on the M site, about a third on the A site, a tenth on the X site, and another tenth with multiple sites (M+A or M+X).

Over the years a number of magnetic configurations have been identified, with complex magnetic ordering ranging from helical to antiferromagnetic or ferromagnetic. These will be explored in more detail below.

3.1.1 Chemically ordered MAX phases

It is possible to achieve chemical ordering within the MAX phase layers if the solid solutions are at specific ratios. To date this has only been done on the M layers and has resulted in two types of chemical ordering to appear in MAX phases, ordering of M layers and ordering within M layers. The first such phase was Cr_2TiAlC_2, a 312 phase, discovered in 2014 [23]. Here the Cr and Ti occupy different layers, as can be seen in Figure 3.2 (a). Due to this out-of-plane chemical order, this subclass of MAX phases has been called *o*-MAX phases. Only 11 *o*-MAX phases have been discovered so far [1].

In 2017, the first phase of what would become another new subclass of MAX phase was discovered with $(Mo_{2/3}Sc_{1/3})_2AlC$ by Tao et al. [24]. Unlike the *o*-MAX phases, where there is a chemical order in the out-of-plane direction with defined layers of different M elements, here there is in-plane ordering *within* the M layers and they are therefore referred to as *i*-MAX phases. In these materials, the M sites are shared by two elements, M^1 and M^2 with the common formula $(M^1_{2/3}M^2_{1/3})_2AX$. The M^2 atom also needs to be at least 0.2 Å larger than the M^1 atom. In the resulting crystal structure, M^1 forms a honeycomb pattern in which M^2 is positioned in the center of each hexagon but slightly shifted towards the A-layer. The shift of M^2 towards the A-layer has an impact on the A-layer which then takes on a Kagomé-like pattern [25]. Paper III of this thesis discusses the growth and magnetic properties of one such *i*-MAX phase, namely $(Mn_{2/3}Sc_{1/3})_2GaC$.

3.1.2 MXenes: a subfamily of MAX phases

Another subfamily of related materials should also be mentioned, these are the MXenes. The MAX phases serve as precursors for MXenes where the A layer has been etched away, giving rise to a two dimensional material that has various interesting properties. MXenes have come under increasingly intense research over the past few years due to the parallels with other low-dimensional materials like graphene and transition metal dichalcogenides such as MoS_2. This field has been expanding rapidly as more possible precursor MAX phases are discovered. The study of MXenes is a field of its own and will not be covered more in this work.

3.1.3 Synthesis of MAX phases

The synthesis of MAX phases has been done both with bulk methods such as sintering, arc melting, microwave heating and spark plasma sintering, as well as thin film deposition with various methods such as magnetron sputtering and cathodic arc deposition. Several comprehensive reviews of thin film synthesis of MAX phases have been written over the years, ranging from 2010 to 2021, where the main deposition methods and results are reviewed [26–29]. Bulk samples have been studied extensively for the MAX phases' unusual structural and mechanical properties, while thin film samples have focused more on the potential uses in magnetic or electronic devices. In general, bulk methods have been used more commonly for synthesis than thin-film methods. This is especially true for synthesis where Ga is used, as Ga is liquid at just under 30 °C, making thin film methods using elemental Ga complicated. However, bulk methods can face more challenges in obtaining phase pure samples. This will be expanded on in the next section. Another feature of MAX phases is that different MAX phases often have similar lattice parameters, opening up the possibility of changing one out for another, or stacking different phases on top of one another in multilayer or superlattice structures. This naturally requires thin film deposition techniques.

3.2 Magnetic properties

Magnetic MAX phases can be obtained by including magnetic elements on the M or A sites. The nanolaminated structure of MAX phases introduces anisotropy and competing magnetic interactions within and between layers when magnetic atoms are involved. Additionally, the difference in distance between M atoms in M-A-M layers versus M-X-M layers introduces yet another anisotropy, in the form of symmetry breaking. This allows for more possibilities for magnetic ordering to occur, which can then be influenced by structural properties via strain/stress engineering or by doping and alloying with different materials. This makes magnetic MAX phases an interesting system to explore.

3.2.1 The challenges of magnetic MAX phases

Although the MAX phase structure was initially discovered in the 1960s with a revitalization in 1995, the finding and synthesizing of a magnetic MAX phase did not occur until 2013 by Ingason et al. [30]. There are numerous challenges when it comes to the investigation of magnetic MAX phases. The first major challenge is to find a stable composition for the MAX phase that contains an element with a magnetic moment. Then, those magnetic moments must be able to couple to each other. This can be difficult, as the formation energy of MAX phases is often close to degenerate with other competing phases. The MAX phases, by their ternary nature, contain a minimum of 3 elements, allowing for a large phase space. Therefore, considerable work has been done with DFT and other theoretical calculations to find suitable combinations of materials that can form stable MAX phases. This ties into the second challenge of magnetic MAX phases: even if the MAX phase can form, achieving a phase pure sample can be difficult. A small amount of a competing phase, which is potentially also magnetic, can make the analysis of magnetic behavior much more complex. Likewise, with solid solutions, it can be hard to determine if the magnetic element is properly incorporated into the MAX phase structure, or whether there is some phase segregation with grains or clusters of a pure magnetic element in the sample. Often the magnetic signal from the MAX phases can be small, and therefore a small impurity of a strongly magnetic material could obfuscate the results coming from the MAX phase. As a result, achieving a high quality, single phase and magnetically interesting MAX phase is not straightforward.

This is further compounded when attempting to dope the solid solution with another element. This can be slightly easier with thin film methods, as they typically involve temperatures below 650 °C during synthesis, while bulk methods often use high temperatures over 1000 °C. The elevated temperature of bulk methods can increase the challenge of attaining phase pure materials. If there are magnetic elements in the materials, then even small clusters of competing phases might give rise to a magnetic signal that could overpower the signal from the MAX phase itself if it is weak. Therefore, care must always be taken when attributing magnetic behavior to a material if the phase purity is in question.

An example of where there could be differences between thin film and bulk synthesis is in the case of $(Cr_{1-x}Mn_x)_2AlC$. It was synthesis in thin

film form by Mockute et al. [31] on Al_2O_3 (0001) with $x = 0.2$. This film showed a clear strong magnetic signal, although with no hysteresis, and a transition temperature well above room temperature. However, films synthesized by Hamm et al. [32] by non-conventional bulk methods with x the range from 0 to 0.15 all showed Curie temperatures below 70 K. Although they did not reach the same $x = 0.2$ in their study, the trend of increasing Mn content did not indicate what was observed by Mockute. This might be influenced by the strain experienced by the thin films affecting the lattice constants, as the magnetic properties are highly sensitive with regards to interaction distances for the magnetic moments. Further attempts at bulk synthesis were done by Sobolev et al. [33, 34] in 2021, which concluded that the samples were paramagnetic, there was a ferromagnetic feature below 50 K but that was attributed to a competing phase.

Yet another challenge for magnetic MAX phases is that typical ferromagnetic elements such as Fe, Co and Ni have not been found to form stable phases as the sole *M*-site element in a MAX phase. Solid solutions with a small amount of Fe on the *M*-site have been made recently [32, 35, 36]. In terms of utilizing these elements on the *A*-site, they have been used successfully through an element replacement method after synthesis [37, 38], or in high entropy solid solutions [39, 40]. However, these have all had their critical temperature at or below room temperature. The difficulty of using Fe, Co and Ni has resulted in a large amount of research focused on Mn and Cr as the magnetic elements, both of which can be on the *M*-site with a number of elements on the *A*-site, allowing for a number of solid solutions with other elements incorporated. Table 3.1 contains an overview of results for Mn and Cr solid solutions with different *A*-site elements. As can be seen, a considerable number of solid solutions with either Mn or Cr on the *M*-site have been made, exploring the phase space of these materials in the search of magnetic MAX phases. [41]

Table 3.1. Overview of results for Mn and Cr containing MAX phases.

Material	Main results	References
Mn_2GaC	Helical magnetic structure at at room temperature with T_N = 507 K. Below ∼214 K, undergoes a transition to a different helical structure, likely with canted moments as it exhibits ferromagnetic like response. Metamagnetic behavior above 214 K. Structural change in the c-lattice parameters of ∼0.2% occurs in the region around 214 K transition. Large c-axis magnetostriction of 450 ppm	[8, 17, 19, 42–49]
$(Cr_{1-x}Mn_x)_2GaC$	Synthesized in the range $\mathbf{0.03 \leq x \leq 0.94}$. Strongly ferromagnetic above x = 0.71, with T_C = 489 K for x = 0.12, x = 0.5 weakly ferromagnetic with T_C around room temperature, also has large anisotropy in resistance in-plane versus out-of-plane, ρ_c/ρ_{ab} = 525. For $x \leq 0.45$ in bulk has T_C below 50 K	[31, 50–56]
$(Cr_{1-x}Mn_x)_2AlC$	Synthesized in the range $\mathbf{0.035 \leq x \leq 0.30}$. First Mn containing MAX phase, x = 0.16 in March 2013. For thin film x = 0.2 had canted AFM with strong saturation up to 280 K, with much higher ordering temperature. Bulk x = 0.3 has T_C = 153 K. For $x \leq 0.16$ in bulk, transition temperatures below 50 K or paramagnetic.	[31–34, 41, 57]
$(Cr_{1-x}Mn_x)_2GeC$	Synthesized in the range $\mathbf{0.025 \leq x \leq 0.25}$. First confirmed magnetic MAX phase, x = 0.25 in May 2013. Ferromagnetic behavior, T_C ranges from 43 K to around room temperature for x ranging from 0.025 to 0.20 respectively.	[30, 36, 55, 58–62]
Cr_2AC A = Al, Ga, Ge	These pure Cr M-site phases all exhibit paramagnetic behavior, even at 2 K.	[33, 36, 59, 63–65]

3.2.2 The first magnetic MAX phases

The first magnetic MAX phase to be reported on, was $(Cr_{0.84}Mn_{0.16})_2AlC$ done by Mockute et al. [57] in March 2013, however, at the time no magnetic measurements were performed on it. Therefore, the first MAX phase to be confirmed magnetic was $(Cr_{0.75}Mn_{0.25})_2GeC$, synthesized and reported on in May 2013 by Ingason et al. [30]. $(Cr_{0.8}Mn_{0.2})_2AlC$, was later synthesized and measured to confirm that it was indeed magnetic by Mockute et al. [31] in April 2014. In December 2013, Mn_2GaC was reported on by Ingason et al. [42]. This was the first magnetic MAX phase with a sole magnetic M-site element, as Cr_2AC (A = Ga, Ge, Al) are all non-magnetic [59].

Mn_2GaC has been studied extensively and has very interesting magnetic properties. Figure 3.3 shows the crystal structure of Mn_2GaC drawn using the program VESTA [66], with both a top view along the c-axis and side view along the a-axis. Shown is both the unit cell, which is the smallest possible depiction of the crystal, as well as an extended view of several unit cells. The top view has a hexagon drawn as a guide to the eye to highlight the hexagonal nature of the structure. The layered nature of MAX phases is apparent in the side view, with each layer a different element. As there are twice as many Mn atoms compared to Ga and C, they can be thought of in two groupings, Mn-C-Mn and Mn-Ga-Mn, with a smaller distance between Mn atoms in Mn-C-Mn versus in Mn-Ga-Mn. This causes the exchange interaction between the Mn atoms to be different within these sublayers.

At low temperature it exhibits a ferromagnetic-like response, at 5 K it has a magnetization of 0.38 μ_B/Mn-atom at 5 T field and a remanence of 0.18 μ_B/Mn-atom. This ferromagnetic-like behavior extends up to around $\sim$ 210 K, where it starts undergoing a transition to AFM ordering as the c-lattice parameter expands by $\sim$0.2%. While in this AFM state it undergoes a metamagnetic transition at increasingly high magnetic fields as the temperature is raised. At room temperature, the metamagnetic transition is centered around 2.5 T field. It then has a Néel temperature of 507 K [8].

Since the Mn_2GaC phase was first synthesized, its precise magnetic structure has remained unresolved. Initially it was believed to have a supercell moment composed of 2 Mn-C-Mn layers that are aligned,

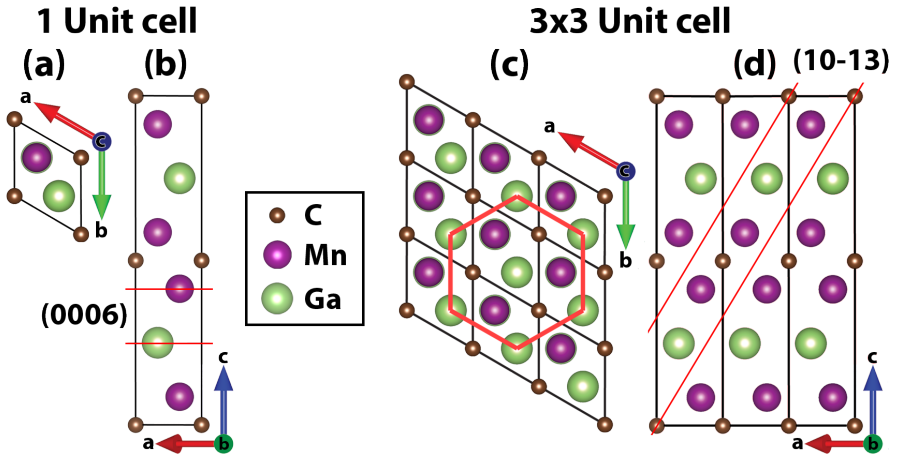

Figure 3.3. The crystal structure of Mn_2GaC. (a) and (c) are a top view down along the c-axis while (b) and (d) is a side view along the a-axis. In (c) a red hexagon has been drawn to highlight the hexagonal nature. The red lines in (b) and (d) indicate the spacing for the (0006) *and* $(10\bar{1}3)$ *planes, which are relevant for the x-ray diffraction analysis in the results section.*

which then flip in the opposite direction with a period of 2 unit cells, as proposed by Dahlqvist et al. [17], with the notation AFM$[0001]^A_4$. In the low temperature regime, the ferromagnetic behavior was explained by a canted moment, which should have been close to degenerate in energy with a collinear moment. This seemed to align with neutron reflectometry measurements done in 2016 [43]. However, the theoretical calculations of AFM$[0001]^A_4$ never aligned perfectly with the observed data. In 2023, nuclear magnetic resonance (NMR) measurements by Dey et al. [18] done on Mn_2GaC at 4.2 K suggested that the magnetic ordering was instead a helical magnetic structure, with a 167.2° angle between Mn-C-Mn super-moments across Ga layers, taking 14 unit cells to complete a single rotation. Very recently, new neutron diffraction measurements by Tao et al. [19], also assign a helical magnetic ordering to Mn_2GaC. However, they find a different angle between the Mn-C-Mn super-moments. This angle varies depending on temperature, at room temperature it is a 120° rotation, while at 1.5 K an additional rotation angle of 92° coexists. However, these results do not explain the ferromagnetic signal present below ∼210 K, which has been suggested to be a result of canting of the

moments. Therefore, it can be seen that although there has been progress with regards to confirming the magnetic ordering in Mn_2GaC, it has not yet been fully resolved.

3.2.3 Search for ferromagnetism above room temperature

Magnetic MAX phases have been studied for just over 10 years and although some interesting magnetic behaviors have been observed in different phases, so far an unambiguous ferromagnetic behavior at or above room temperature has eluded discovery, even though considerable amount of research has been conducted. There have been a few that have come close, such as Ta_2FeC and Nb_2FeC with Curie temperatures of 281 K and 291 K respectively [37]. Additionally, $(V,Mn)_3GaC_2$ was found to have a transition temperature above room temperature, however, it was only measured up to 300 K and therefore the transition temperature remains unknown. The measured saturation moment was also rather weak at only $0.036 \pm 0.004 \mu_B$ per M atom at 100 K [67]. Another one close to room temperature is $(Cr_{0.5}Mn_{0.5})_2GaC$ [52], that was also only measured up to 300 K, with a saturation moment of $0.19 \mu_B$ per M atom at 5 T with $0.004 \mu_B$ per M atom remanence.

There have been some other interesting non-ferromagnetic MAX phases that have their transition temperature above room temperature, such as Ti_3AC_2, A = (Al, Fe) [68], which has a strong superparamagnetic response up to 300 K, however it has not been measured above 300 K. $(Cr_{0.93}Mn_{0.07})_2GaC$ [55] has a strong canted AFM ordering with a transition temperature of 505 K.

In recent years, there has been a large interest in another avenue in tuning the magnetic interactions in MAX phases, that is in the *i*-MAX phases. There have been a number of attempts at using different rare earth elements as the secondary M material, with Re = Gd, Tb, Dy, Ho, Er and more, such as $(Cr_{2/3}Re_{1/3})_2AlC$ [69], $(W_{2/3}Re_{1/3})_2AlC$ [70] and $(Mo_{2/3}Re_{1/3})_2AlC$ [71, 72]. All of these have shown an AFM structure with low transition temperatures below 40 K, except Er and Tm which were paramagnetic. Yet another method for the fabrication of magnetic MAX phases has been to use top down synthesis where generally the A element has been substituted post synthesis via chemical reactions with other elements such as Fe, Co or Ni. This has been a promising avenue,

yielding ferromagnetic phases with Curie temperatures close to room temperature. These include Ta_2FeC at 281 K and Nb_2FeC at 291 K [37], both of which also had relatively strong magnetic moments of 0.74 μ_B and 0.18 μ_B per Fe atom respectively.

High entropy MAX phases could also be a promising avenue to explore in terms of magnetism, as with the increased entropy, it becomes possible to include the more traditional magnetic elements of Fe, Co and Ni. Chen et al. [40] synthesized high entropy phases on the M site, $(Ti_{0.2}V_{0.2}Nb_{0.2}Ta_{0.2}Zr_{0.2})_2FeC$ and $(Ti_{1/3}Nb_{1/3}Ta_{1/3})_2FeC$, both of which were ferromagnetic with Curie temperatures of 248 K and 302 K, respectively. Likewise, Li et al. [39] alloyed on the A site with, $V_2(Fe_xCo_yNi_zSn_{1-x-y-z})C$ and $V_2(Mn_xFe_yCo_zNi_nSn_{1-x-y-z-n})C$, where again both were ferromagnetic with Curie temperature of around 200 K and 100 K respectively.

3.2.4 Applications for magnetic MAX phases

The inherently nanolaminated nature of MAX phases with different interactions between M-X-M and M-A-M layers, offers opportunities to tune their properties for various applications, by either strain engineering or elemental substitution. One such application is in spintronics, the branch of electronics making use of the spin of the electron in addition to its charge. The similarity with magnetic multilayer structures has inspired the idea that it might be possible to achieve giant or tunneling magnetoresistance (GMR or TMR) behavior. GMR structures rely on the spin dependent scattering at interfaces between magnetic and non-magnetic metallic layers and so a natural magnetic nanolaminate could be highly interesting in this respect. Similarly, TMR relies on spin-dependent tunneling between ferromagnetic layers across an insulating layer. It has been shown that MAX phases can have a large electrical anisotropy, in $(Cr_{0.5}Mn_{0.5})_2GaC$, the ratio of resistance in-plane versus out-of-plane was measured to be $\rho_c/\rho_{ab} = 525 \pm 49$ [53]. Therefore, it is possible to envisage TMR-like effects in certain types of MAX phases.

Potential competing interactions in the layers of MAX phases could also form spin textures such as skyrmions which have been suggested for various data storage and manipulation devices. Furthermore, the hexagonal lattice could allow other hexagonal 2D materials to be used in

conjunction to harness the potential of 2D magnetic materials. Another potential use for magnetic MAX phases could be in magnetocalorics. For example, the magnetic phase transition around 210 K in Mn_2GaC has been investigated in this context, however, the maximum of $|\delta S_M|$ at 1 T is about 0.1 J$\cdot$ mol$^{-1}\cdot$K [8] which is small, but could be improved if the transition could be narrowed as it ranges from 180 K to 240 K. Finally, the physical properties of MAX phases with regard to their resistance to thermal shocks, oxidation and machinability make them suitable as magnets in harsh usage conditions. Their lower density compared to traditional magnets offers additional benefits, for example in electric motors, transformers etc., by reducing the overall weight. For comparison, NdFeB, SmCo and AlNiCo have 7.5, 8.2 and 6.9 g/cm^3 respectively, while $(Mn_{1-x}Cr_x)_2GaC$ is around 6.9 g/cm^3. Therefore, it is comparable to AlNico, while being 8.7% and 18.9% lighter than NdFeB and SmCo respectively.

4 Experimental Methods

In this section, an overview will be given of the methods used for synthesis and characterization of the samples. All samples in this thesis were synthesized using DC magnetron sputtering. After synthesis, the structure was then characterized by x-ray diffraction measurements and the magnetic behavior by vibrating sample magnetometry. Select samples had their elemental composition analyzed using energy dispersive x-ray spectroscopy in a scanning electron microscope. Finally, two samples were measured in a transmission electron microscope to confirm the crystal structure and composition.

4.1 Sample synthesis

4.1.1 Magnetron sputtering

Magnetron sputtering is a common physical vapor deposition (PVD) method for coatings or thin film growth, used both in research and industry. Applications can range from corrosion or wear resistant films to custom tailored specialty films such as magnetic coatings of hard drives. It is a relatively simple method with great flexibility depending on the configuration of the vacuum chamber being used, ranging from single magnetron chambers with an elemental or alloy target, to a multi-magnetron chamber for adjustable composition or sequential layers of different materials. This makes it an attractive choice for use in research.

A schematic of a typical magnetron can be seen in Figure 4.1. The magnetron is placed in a vacuum chamber with a working gas at low pressure, typically around 4×10^{-1} Pa, most commonly argon, although other noble gases can be used. The working gas is then ionized and forms a plasma above the target material by supplying a direct current negative voltage of generally 300-500 V to the target. This is aided by the confinement of the plasma by a magnetic field from magnets placed

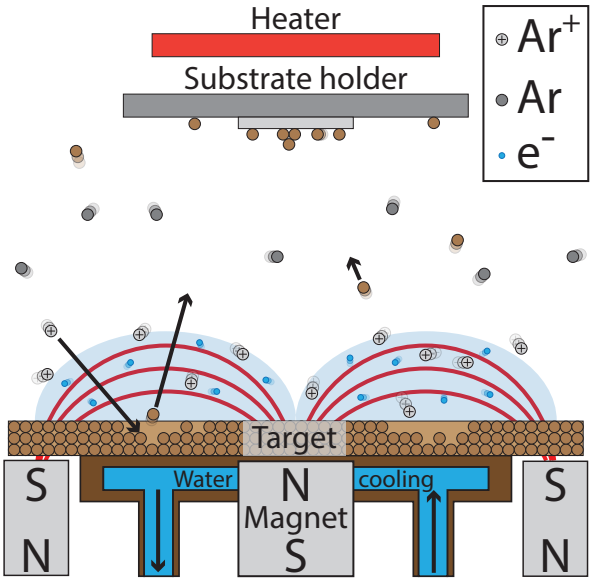

Figure 4.1. Schematic of magnetron sputtering. Voltage applied to the target causes argon atoms to get ionized in a plasma above the target, which is confined by the magnets. This accelerates the argon toward the target where they bombard it, causing the target atoms to sputter outward. Some of these atoms land on the substrate in the substrate holder and if energetic enough, they move slightly around and find a favorable location to stop at. This slowly grows the film on the substrate surface.

under the target. The positively ionized gas atoms then bombard the target material due to the electric field, which results in atoms from the target being sputtered out into the vacuum chamber. The object or substrate to be coated is placed in front of the magnetron, allowing a film to grow on it atom by atom, layer by layer. Typical growth rates range from less than one to tens of Ångström a second.

The most common magnetron sputtering method is direct current magnetron sputtering (dcMS), however, there are a few variations. There is radio frequency (RF) magnetron sputtering, which is used on insulating targets to avoid charge build up on the surface of the target. For this a 13.56 MHz power supply is used. Another variation is high power impulse magnetron sputtering (HiPIMS), which uses a pulsed power supply,

with pulse length from 10-500 μs with frequency from 10 Hz to kHz range. These pulses can have very large power densities on the order of kW·cm^{-2} compared to 1-10 W·cm^{-2} for dcMS. The benefit of this is that a larger proportion of the sputtered atoms get ionized and the sputtered atoms have a higher kinetic energy. The higher energy increases the surface diffusion on the substrate, allowing them to find more favorable positions, which can result in denser films among other things.

The properties of the film being grown can be affected by various sputtering and substrate conditions. One of the main influences is the substrate type and substrate temperature, which can affect crystal quality, solid solution formation, or surface morphology. The pressure of the working gas also has an effect, as a higher pressure results in more collisions between sputtered atoms and the working gas atoms on their way from the target to the substrate, therefore, lowering the energy of incoming atoms. The ability to bias the substrate with voltage can also influence the film by slowing or accelerating the incoming ionized atoms. For magnetic films, it is possible to place magnets near the substrate to induce magnetic ordering in the film. Other considerations include the angle between the magnetron and substrate surface, whether the substrate is being rotated, and the distance between magnetron and substrate, to name a few.

Another feature of magnetron sputtering is the ability to do reactive sputtering, where a reactive gas is added to the working gas during sputtering, often oxygen or nitrogen. By varying the partial pressure of the reactive gas, different stoichiometries in the film can be achieved. The reactive gas has an effect not only on the film that is being grown but also on the target during sputtering. If the partial pressure is raised too high, it can result in poisoning of the target surface, where the reactive gas bonds with the target surface, which can change the sputter rate or even disrupt the formation of the plasma if its surface becomes insulating when using dcMS.

4.1.2 The deposition system

The sputtering of an elemental source of gallium is non-trivial, as the melting point of gallium is only 29.8 °C. Therefore, the vacuum chamber setup has to accommodate the gallium being in a liquid state. This means that the magnetron needs to be located at the bottom of the chamber

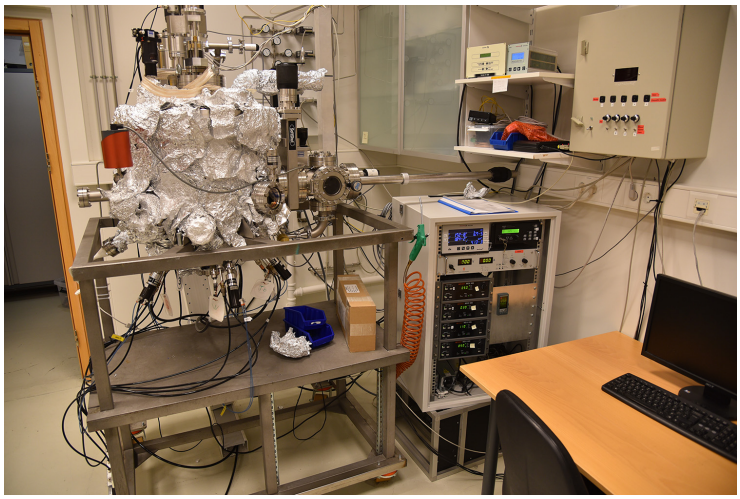

Figure 4.2. Photo of the sputtering chamber, wrapped in aluminum foil for bake-out.

pointing up towards the substrate. The sputtering chamber used in this study can be seen in Figure 4.2. It has five DN100CF flanges arranged in a star pattern around the bottom facing upward, with a 35° degree angle to the substrate normal. These 5 flanges are equipped with three 3" magnetrons and two 2" magnetrons, each with an integrated shutter. In the middle of the bottom of the chamber is a single DN63CF flange directly beneath the substrate equipped with a 2" magnetron. As the DN63CF flange was too small to accommodate an integrated shutter, a manual shutter assembly was fitted in front of the sample holder.

To contain the gallium, a special crucible was machined and attached to the 2" magnetron at the bottom of the chamber. It was made out of copper to ensure good thermal conductance to the cooling block on the magnetron. The crucible was sputter coated with 200 nm of tantalum to make a barrier against the diffusion of gallium into copper. Pellets of 99.9999% gallium were then melted in the crucible by heating on a hot plate. The crucible and melting of Ga can be seen in Figure 4.3.

The sample holder used for sputtering was made out of two molybdenum plates, one as a backplate and the front as a holder machined with 6 seats for substrates, four 10x10 mm and two 5x5 mm seats. This allowed for sputtering on a number of substrates at the same time. The sample holder

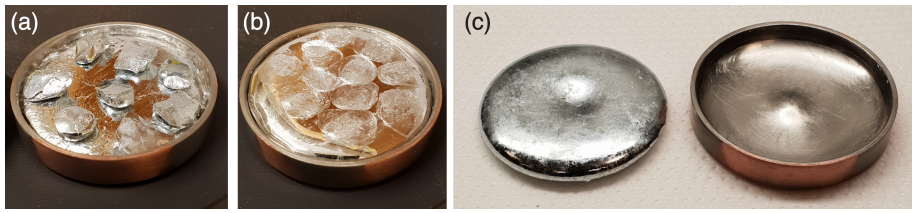

Figure 4.3. Melting of Ga in the Cu crucible. (a) The crucible during the melting of Ga pellets, 99.9999% pure Ga pellets visible on top. (b) Taken just after melting more pellets. (c) The final Ga chunk sitting beside the crucible prior to loading in the deposition chamber

is then mounted below a heater from Momentive, made with pyrolytic boron nitride and pyrolytic graphite. With this system it is possible to reach up to 800 °C on the sample holder. The sample holder is inserted into a rotation stage, allowing it to be rotated $\pm 360^\circ$ at a rate of up to 20 revolutions per minute. However, since there are cables connecting the heater and thermocouple, it is not possible to do continuous rotation, limiting it to a 360° back and forth motion.

4.1.3 Optimization of growth conditions

There were a total of four separate growth sessions conducted over the course of this thesis project.

1. Initial testing of the growth of Mn_2GaC. This session ended up mostly focusing on a series of samples with different power applied to the Ga magnetron. At the end of the session, a few depositions were performed where substituting Ga with Al was attempted. In addition, preliminary work was carried out to test the growth of $Mn_2GaC_xN_y$ using a reactive process.
2. Initial attempts at growing $(Mn_{2/3}Sc_{1/3})_2GaC$, on different substrates and at various temperatures.
3. Further optimization of Mn_2GaC, series as a function of temperature. Further optimization of $(Mn_{2/3}Sc_{1/3})_2GaC$.
4. Attempts at substituting Mn with Fe and Cr, making $(Mn_{1-x}Cr_x)_2GaC$, $(Mn_{1-x}Fe_x)_2GaC$ and $(Mn_{1-x-y}Fe_xCr_y)_2GaC$.

Here we will focus on the procedure for optimizing the growth conditions. The choice of substrate as MgO(1 1 1) was based on the results from Petruhins et al. [52] for $(Mn_{0.5}Cr_{0.5})_2GaC$, where MgO(1 1 1), Al_2O_3 (0 0 0 1) and SiC-4H(0 0 0 1) were tested. The phase formed on all the substrates, but MgO was found to produce the highest quality single crystal films. For the initial deposition parameters, the work by Ingason et al. [30] was used as a reference, therefore, the temperature of 550 °C was selected. Prior to deposition, the substrates were heated at 600 °C for roughly 1 hour before reducing the temperature to 550 °C.

The deposition rate calibration of Mn and C was straightforward where elemental films were grown at different power values at room temperature and their thickness measured by XRR. However, this approach did not work for the Ga target, as sputtering on a clean Si substrate to form a film did not give a smooth film that was measurable by XRR. Therefore, for the first growth session on the Mn_2GaC phase, which was also the first time that the Ga target was used to grow films outside of attempting rate calibration, we decided to try to optimize the Ga from observing the crystal quality as a function of the power applied to the Ga target. For the first attempt, a low power of 20 W was used as a shot in the dark to see if the phase would be obtained, with Mn at 48 W and C at 265 W, calibrated to give a 2:1 ratio of Mn:C. The phase was obtained successfully on the first attempt. However, it was not measurable by XRR because of high surface roughness and thickness. The Mn power was then reduced to 46 W and a series of Ga powers was made. The Mn_2GaC phase was surprisingly stable as a function of Ga power down to about 10 W with fixed Mn and C power, as seen in Figure 4.5. For the highest Ga powers, the competing phase Mn_3GaC was observed, but as the Ga was reduced to 18 W and below, it disappeared.

The competing phase Mn_3GaC will be mentioned several times, as this is the main competing phase that occurred during growth. The crystal structure of the phase can be seen in Figure 4.4, which is an antiperovskite structure. This will mainly be detected as a (1 1 1) peak seen in x-ray diffraction measurements. The presence of this competing phase complicates the magnetic analysis, as it has a magnetic signal in the transition region of Mn_2GaC. It is antiferromagnetic up to around 160 K, where it transitions to a ferromagnetic state with a Curie temperature of a about 260 K, above which it is paramagnetic [73, 74].

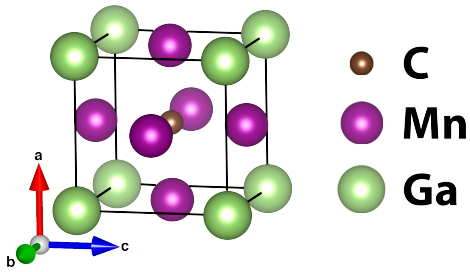

Figure 4.4. The crystal structure of Mn_3GaC, a competing antiperovskite phase. A cubic phase with Ga in the corners, Mn on the faces and C in the middle.

EDX measurements showed that this sample series has a Ga to Mn ratio in the range 40-50%, while the stochiometric value is 33% for Mn_2GaC (excluding C, which can not be quantified by EDX). This showed that sputtering from the Ga target in its liquid state was quite fast. The excess Ga migrates to the surface of the film, seen in SEM as large Ga islands dispersed on the surface of the film, as seen in 4.6. Therefore, some excess Ga during growth seems to be acceptable, but too much results in the appearance of competing phases. In some of the later growth sessions, while making thicker films, this became a slight problem, as it was beneficial to have a slight excess of Ga during growth. However, the build-up this caused over time got worse with long growth times and started degrading the films. Therefore, for some of the thicker films, a slight excess of Ga was used at the start of the growth, and then the growth rate was reduced after a few minutes to be closer to the stoichiometric rates to avoid this build-up. This effect was not studied in more detail, however, doing a series with thinner samples in the future might cast more light on how the initial stages of growth occur.

The initial Ga power series in the first growth session gave a rough idea of the optimal power for the Ga magnetron. In the third growth session, to get a better estimate of the growth rate of Ga, a series of seven Mn_xGa_y films were made using a fixed Mn power, with a known Mn deposition rate at 100 W and varying the Ga power from 5 W to 75 W. The resulting films were flat and gave good measurements in XRR. These films were then measured with EDX in the SEM to get the Mn/Ga ratio, with the percentage of Ga in the films ranging from 16 % to 71 %. Combining the results from XRR and EDX, it was possible to calculate backward the

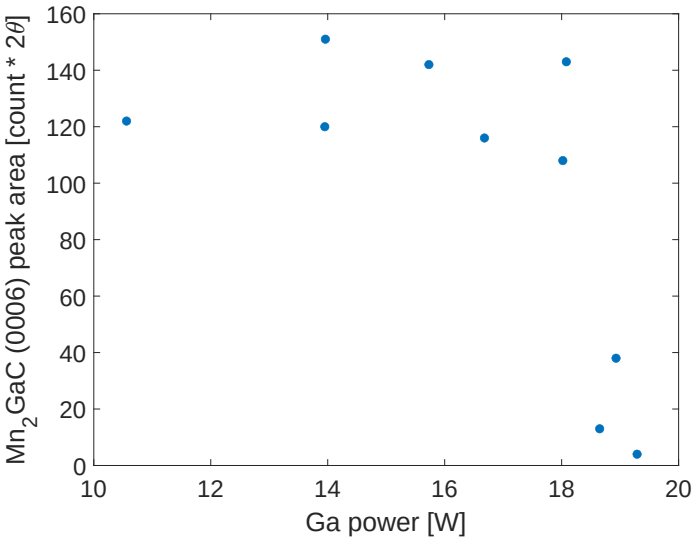

Figure 4.5. XRD peak area intensity extracted from the (0006) *peak of* Mn_2GaC *as a function of Ga magnetron power. Above 18 W the* Mn_3GaC *phase starts to form and the (0006) area intensity drops significantly.*

Ga deposition rate. The Ga deposition rate as a function of Ga power is shown in Figure 4.7.

In addition to the Ga series, a smaller series of Mn_2GaC films was grown where only the power of the Mn and C magnetrons was adjusted while keeping the others fixed to fine tune the optimization of Mn_2GaC crystal. This will not be expounded upon more here as that is a more standard procedure compared to the special needs for the Ga target.

A series of four films were grown between the temperatures of 520 °C to 600 °C to see the effects of temperature on the crystal formation. Figure 4.8 shows the XRD peak area of the (0006) plane as a function of temperature. As the temperature is increased from 550 °C there is a sharp decrease in intensity, concomitant with a peak of the competing phase Mn_3GaC appearing, although that peak is still small compared to peaks from Mn_2GaC. Going below to 520 °C, the peak intensity also decreases, however, there is no Mn_3GaC present at this temperature. The optimal temperature is therefore 550 °C, in agreement with previous results from Ingason et al. [30].

In the fourth and last growth session, while re-optimizing for the Mn_2GaC

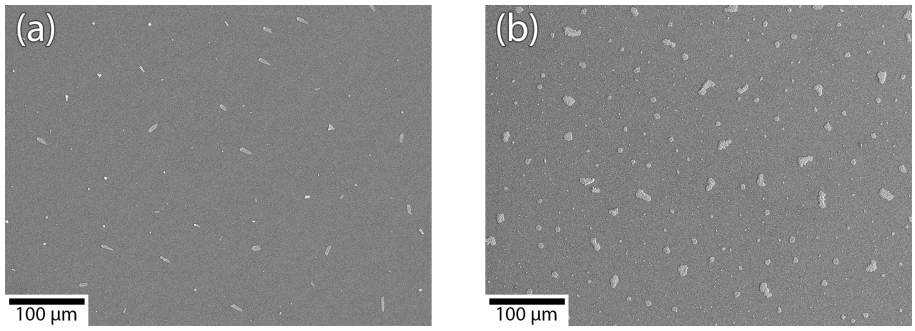

Figure 4.6. Ga islands seen on SEM images for two Mn_2GaC films. (a) is 10 minute sputter time, while (b) is 60 minutes at same power settings. Both films were high quality according to XRD and had the same composition as measured by EDX, 60% Mn and 40% Ga. Expected value for Mn_2GaC should be 33% Ga when excluding C. Therefore, it can be seen that the excess gathers on the surface in islands, which increases with sputter time if not addressed.

phase it proved trickier this time around compared to previous sessions as most of the films had the $(10\bar{1}3)$ peak showing up in the XRD measurements. This is a plane that is tilted 59° degrees to the $(000l)$ planes. This caused the film to contain a set of mixed orientations of the Mn_2GaC phase. Although this complicated the analysis, it also opened the opportunity to study the anisotropy of the Mn_2GaC phase. In hindsight, the reason for this mixed-orientation growth mode in the last session may have been that the power on the magnetrons was increased by roughly 25% compared to the other sessions. This had been done to slightly increase the growth rate to cut down the sputtering duration on thicker samples, which ranged from 30 to 60 minutes.

For films containing Cr and Fe, no additional optimization was done for them other than optimizing the Mn_2GaC phase prior to their growth. These samples also contained the mixed-orientation growth mode seen in the pure Mn_2GaC earlier in the session. This leaves further optimization of these phases open to exploration, especially for the ferromagnetic phase of $(Mn_{1-x}Cr_x)_2GaC$ where $x \leq 0.3$. There may also be interesting optimizations made for the quinternary phase $(Mn_{1-x-y}Fe_x)Cr_y)_2GaC$, as the Cr seemed to stabilize the phase compared to only $(Mn_{1-x}Fe_x)_2GaC$.

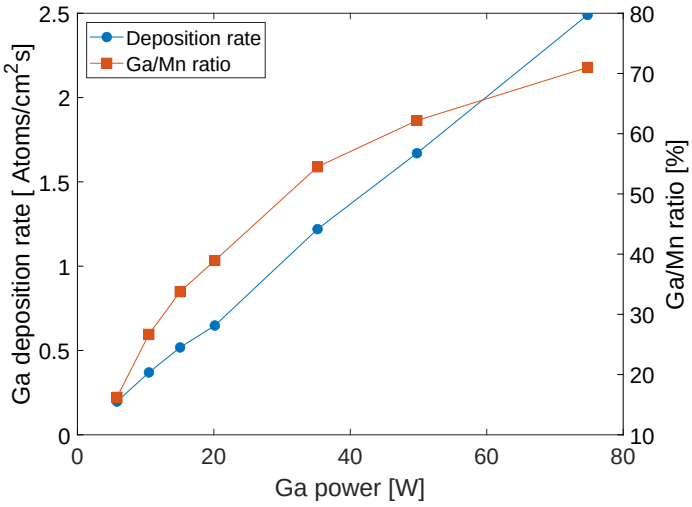

Figure 4.7. Ga/Mn ratio measured by EDX in an SEM as a function of Ga magnetron power on the right axis with the extracted deposition rate on the left axis. The Mn power was fixed at 99 W giving 1.02×10^{15} *atoms/cm*^{2}*s.*

4.2 X-ray characterization

Characterization by x-rays is one of the most common ways to investigate the structure of crystalline films, as the wavelength of x-rays is comparable to the inter-atomic distances, allowing them to interfere constructively/destructively. What follows is a description and examples of the x-ray methods used in this work.

4.2.1 X-ray diffraction

X-ray diffraction (XRD) measurements form the basis for identifying different crystal structures and phases, and the foundation of that is Bragg's law, given by

$$n\lambda = 2d\sin(\theta) \tag{10}$$

which describes for what angles constructive interference between scattered x-rays of wavelength λ occurs. Here θ is the incident and diffracted angle and d is the interatomic distance. The situation is depicted schematically in Figure 4.9. In practice, the incident angle is commonly referred

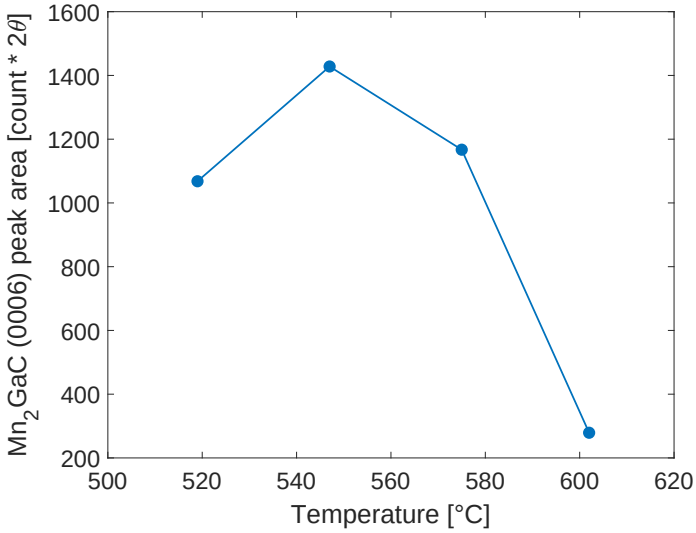

Figure 4.8. XRD peak area intensity as a function of temperature for Mn_2GaC (0006) peak. The optimal temperature is found to be 550 °C.

to as ω while the detector uses 2θ on the diffracted side. To perform a scan, the detected intensity is recorded while the incident and diffracted angles are swept, maintaining the ratio $\omega = \theta$. For systems where the x-ray tube is stationary, the detector moves at twice the speed of the sample. These scans are called $2\theta/\omega$ scans and are the most common way to characterize the crystal structure. The resulting spectrum will give peaks at 2θ angles corresponding to the interatomic spacings in the crystal (sometimes known as Bragg peaks). From these interatomic spacings we can work out the crystal structure. This can be used as a fingerprint for the material, as each material has slightly different interatomic spacing or crystal structure.

Another common scan is the ω scan, where the detector is stationary while ω is swept. This is also sometimes called a rocking curve scan. This is typically done at the 2θ position of a Bragg peak and probes the amount of tilt or mosaic spread in the crystal plane being studied. Yet another scan is a $2\theta/\omega$ scan with an offset in ω. By offsetting ω it is possible to probe crystal planes that are off-specular, that is not along the surface of the crystal. This is used, for example, in reciprocal space maps (RSM) on single crystals, where a map is made with a series of different ω offsets or using a 2D detector to collect the data.

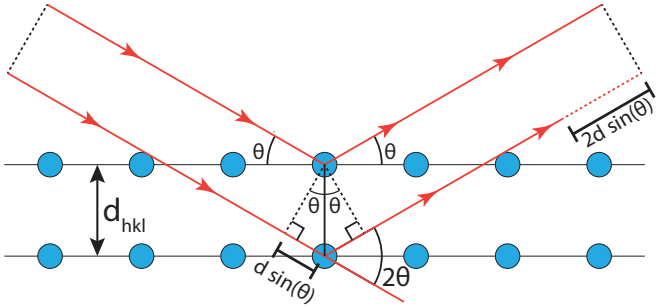

Figure 4.9. Schematic showing Bragg's law with two incident beams and their diffraction.

The system used for XRD measurements was an Empyrean system from Panalytical using Cu K radiation. Depending on the scans performed, the incident optics used were either a hybrid monochromator, centered around the Cu Kα_1 peak at 1.54056 Å, or the iCore optics by Panalytical, which include an x-ray mirror that suppresses the Cu Kβ peak below 1% leaving Cu Kα_1 and Kα_2 as the main source. Various divergence slits were used to limit the beam and increase resolution. On the diffracted side were Panalytical's dCore optics, capable of inserting parallel plate collimators or soller slits in the beam path. The detector used was a Panalytical PIXcel^{3D}, which can be used in 0D, 1D or 2D operational modes.

4.2.2 X-ray reflectivity

X-ray reflectivity measurements are used to find the density, thickness, and roughness of thin films (<300 nm). XRR scans are performed at low angles of 2θ, where a fringe oscillation pattern forms from the interference of x-rays scattered off different interfaces between layers or the substrate. By fitting the pattern, various parameters can be extracted. The density can be read from the angle where the intensity starts dropping after the peak of total reflectance, called the critical angle. Thickness is extracted from the frequency of oscillations and roughness from how the oscillation intensity decays. The amplitude of the oscillations relates to the density contrast between different layers, either between the film and substrate, or if the film has layers of different density.

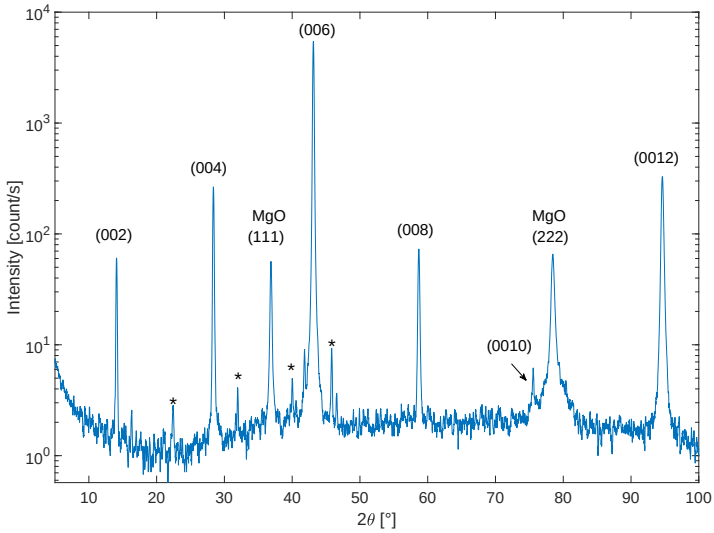

Figure 4.10. Example of an XRD scan. A film of Mn_2GaC on MgO(111) measured with a hybrid monochromator. Star marked peaks are a competing phase of $MnGa_4$.

The program used for the analysis of the XRR scans was Panalytical's Advanced Material Analysis and Simulation Software (AMASS). To perform the simulation it uses database values for the material properties of different elements and a model of the film. This model is set up with the substrate and layer structure along with the expected thickness, density and roughness of each layer. From that starting point an iterative process begins where the programs iterates the parameters to get the best fit to the measured data.

4.2.3 Pole figures

Pole figures can inform about the orientation and crystallinity of a sample, whether it is polycrystalline, textured, or epitaxial. Pole figure measurements are performed at the 2θ value of a given crystal plane and collecting a series of 360° in-plane rotation, ϕ, scans as a function of sample tilt, χ. This probes the possible orientations of the selected crystal plane. If the distribution is uniform, then the film is polycrystalline as there is no preferred orientation of the crystallites. An example of texture would be a ring feature at a given tilt, where there is a well defined out-of-plane order

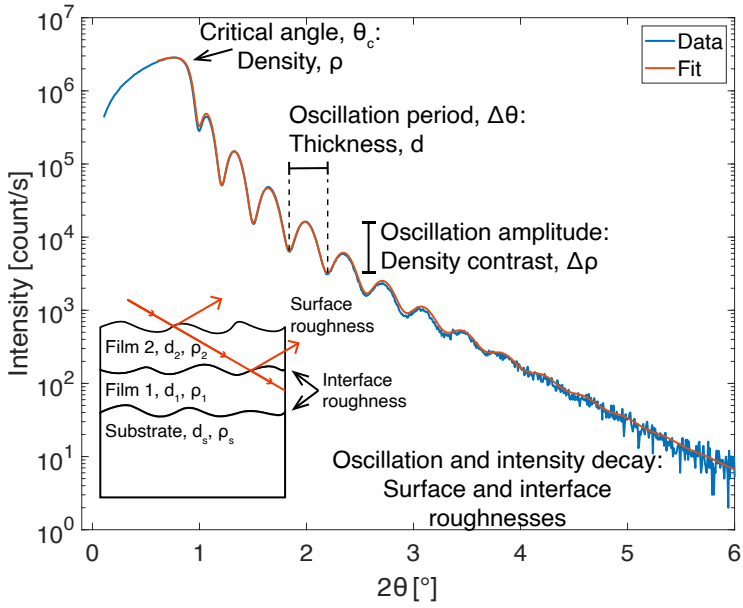

Figure 4.11. Example of an XRR scan on a 22.5 nm thick Pd film with a fitted simulation. Pointed out are the main features a visual inspection of an XRR scan gives information about. The density is related to the position of the critical angle θ_c, where the intensity falls off after maximum intensity. The thickness is related to the oscillation period of the fringes while the amplitude to the density contrast between film components, such as substrate and film layers. The decay of both the oscillations and intensity gives information about the surface and interface roughnesses.

but with random in-place orientation. If there are well defined points for a given tilt angle, then it is single crystalline, with both out-of-plane and in-plane ordering as seen in Figure 4.12.

4.3 Magnetic characterization

4.3.1 Vibrating sample magnetometry

A vibrating sample magnetometer (VSM) is a common instrument for magnetic measurements. It works by vibrating a sample in between two pick-up coils in the presence of an external magnetic field. As

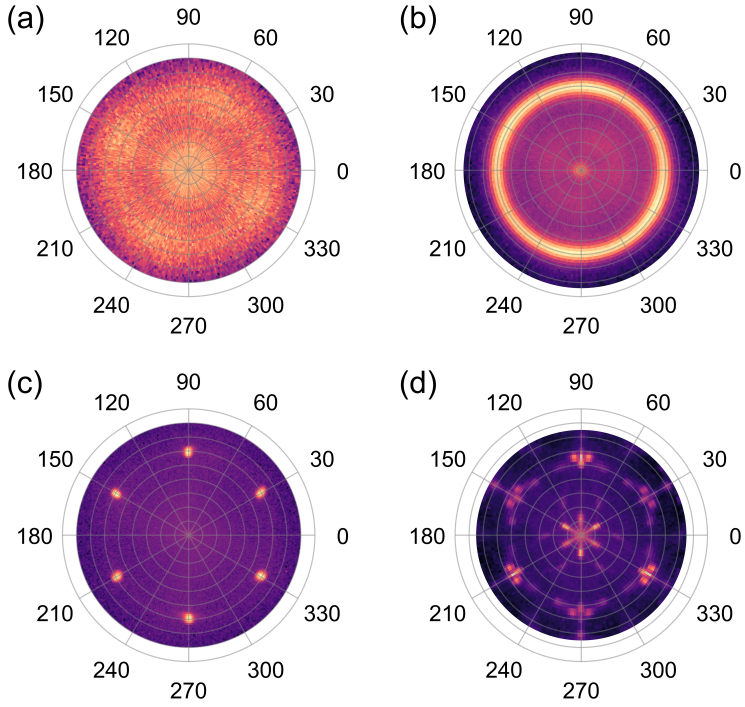

Figure 4.12. Examples of pole figures showing different crystallinity. (a) Polycrystalline film, with minor texture. (b) Textured film. (c) Epitaxial film. (d) Epitaxial film with twinning.

the external field induces magnetization in the sample, the sample in turn induces current in the pick-up coils due to its vibration. This can be measured using a lock-in amplifier at the vibration frequency. The external field is then swept from a positive value to a negative value and back, performing a hysteresis loop measurement. VSM systems are also often equipped with a temperature stage, making magnetization measurements as a function of temperature possible.

Two VSM systems were used for measurements in this theses. A 5 T mini high field cryogen-free magnet system from Cryogenic capable of measuring between 2-320 K, and a Lakeshore 8600 system capable of between 2.8 T and 1.6 T field strengths depending on pole gap setting, and a temperature range of 80-1273 K with a variable temperature inset or oven options.

The Cryogenic system uses a superconducting vertical solenoid that is

always cooled to around 4 K using a closed loop helium cooling circuit. A secondary closed loop helium cooling circuit, driven by the cold head of the primary loop, is used to cool the outside of the sample chamber walls, while inside the sample chamber roughly 50 mbar of helium is used for thermal conductance between the sample and the walls. Measurement samples were mounted on a carbon fiber rod and attached with GE low temperature varnish (C5-101) from Oxford Instruments. The sample size can be up to 10×10 mm^2 in this system over the whole temperature range.

The Lakeshore system uses conventional watercooled electromagnets with an adjustable pole gap. By changing the pole gap, various sizes of samples can be measured, however, the maximum field value will also change depending on the pole gap. The temperature stage used for this system is inserted between the poles and uses nitrogen gas chilled by a liquid nitrogen reservoir to reach temperatures down to 80 K. If the sample is heated above 500 K, then argon gas is used instead to avoid reactions with the sample. The system is also equipped with a rotational head, capable of 360° rotation. This makes it useful either for doing in-plane rotation measurements or measuring the response going from in-plane to out-of-plane. For room temperature measurements the samples were attached to plastic holders using the GE varnish. A quartz rod with the GE varnish was used for low temperature measurements and when expecting to go over 400 K, a CC High Temperature cement from Omega Engineering on a boron nitride rod was used. When using the temperature stage, there was a limit on the sample size, as the diameter of the chamber is only 6.4 mm, therefore the samples were cut to either 5×5 mm^2 or 5×10 mm^2 sizes.

The most common measurement performed with a VSM is a hysteresis loop measurement from which the remanence and coercive field can be extracted, and if the field is high enough, saturation magnetization can be found as well. By performing these measurements over many temperatures we can get a better look at the behavior of materials and help discern what type of magnetism is present. For example, by looking at the remanence as a function of temperature for a ferromagnet, we can find the Curie temperature, where the thermal energy overcomes the magnetic ordering.

Measurement of the magnetic susceptibility of samples can also give insight into the magnetic ordering of the material being studied. These measurements can be performed by setting a fixed field and ramping the temperature or by extracting the slope from a part of a hysteresis loops as a function of temperature. However, care must be taken to ensure that the slope is coming from the film being measured and not the substrate, sample holder, or the glue that is being used.

4.3.2 Background subtraction

Vibrating sample magnetometry measures the total magnetic moment of a sample that is vibrated between the pick-up coils, which includes both the sample and the sample holder. In the case of thin film samples this will include the magnetic moment of both the film and the substrate. Since the film volume is orders of magnitude smaller than the substrate volume, the signal due to the substrate can be significant or even dominating in case of very thin or weakly magnetic films. Therefore, it is important to ensure that careful background subtraction is carried out to extract the true film signal. As for the intensity of the sample holder, that can be minimized if the holder extends both above and below the centerpoint of the pick-up coils, as the contributions from it will cancel out. If that is not possible, then this must also be taken into account when separating the signal from the substrate and thin film.

To perform this separation, a background subtraction is needed to extract the film signal. This must be done carefully to avoid adding an extra signal to the final results. There is a particularly critical need for this for low temperature measurements on MgO substrates, as below 20 K there is a strong paramagnetic signal from the substrate while above this temperature it is diamagnetic, see Figure 4.13 (a). This makes it difficult to extract the signal from the film, seen in (b), unless the background is removed. The procedure for this was to take a clean substrate from the same batch of substrates as the film was grown on, and measure it at the same temperatures as the film. Ideally, the substrate would be measured and then the film grown on it before it was measured again. However, that would take a prohibitive amount of time as measuring the whole temperature range took around 24 hours. Therefore, a single substrate from the substrate batch was used, as the amount of defects and possible contaminations should be similar. The results can be seen in Figure 4.13

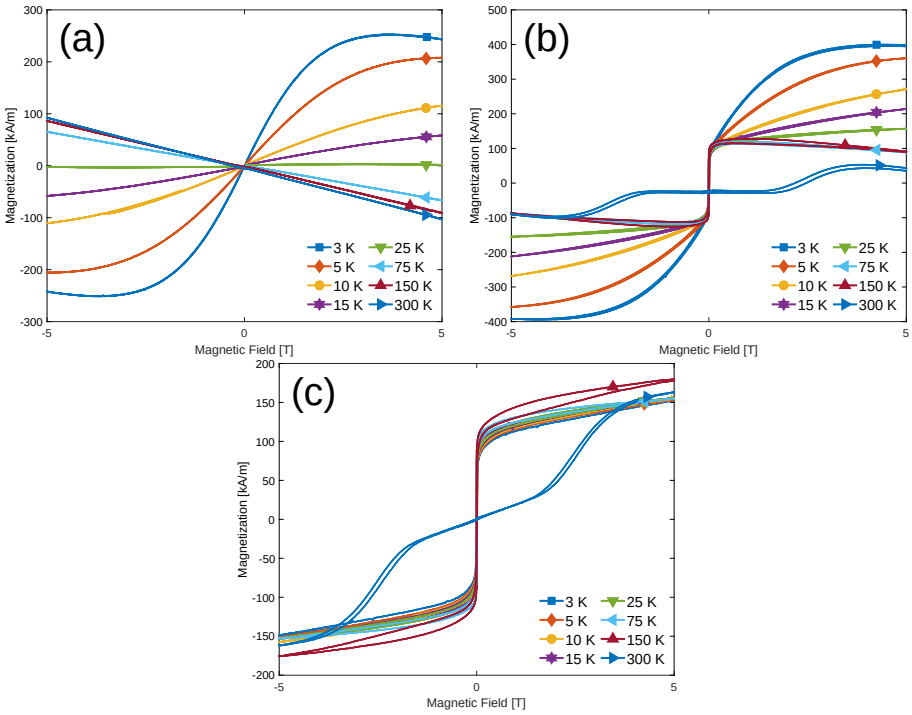

Figure 4.13. Background subtraction for VSM measurements on MgO, shown at different temperatures. (a) Measurement of a clean MgO substrate. (b) Raw measurement of the film signal. (c) The film signal after simply subtracting the measurements in (a) from (b), successfully removing effects of MgO substrate and sample holder.

(c), showing that the background was successfully removed, leaving the film signal. These low temperature measurements were performed in the Cryogenic system, which can accommodate the full 10×10 mm^2 substrate size, therefore the samples were not cut for these measurements.

Some background subtraction was also done for measurements done in the Lakeshore system. Here the sample size is limited to about 5×10 mm^2, therefore the samples must be cut or broken before mounting and care must be taken to have the same size for the film and bare substrate. For susceptibility measurements performed in the Lakeshore system, the background was subtracted by fitting the slope of the clean substrate above 1.5 T and removing that from the measured film. This was done to try to extract meaningful data out of those measurements, as the film

signal was very small. The background measurement on SiC was also done to see if a ferromagnetic signal around zero was coming from the film or potential contaminants from the SiC substrate or the cement used to mount the sample. This ended up confirming that the signal around zero field was not coming from the film but rather the substrate and holder.

4.4 Electron microscopy

4.4.1 Scanning electron microscopy

Scanning electron microscopes (SEM) are able to resolve details on the sample surface down to the order of a few nanometers. This is achieved by accelerating electrons from a tungsten filament at high voltage, often at 20 kV, and focusing them on the sample. This beam of electrons is then scanned across the surface and an image is captured. If an x-ray detector is mounted on the microscope, then it is possible to collect a spectrum of x-rays that can be fitted to elemental fingerprints. As the high energy electrons from the beam hit atoms, they kick out electrons from the electron shell of the atoms, and as the outer electrons fill the gap of the kicked out electron, they emit a characteristic x-ray corresponding to a specific element. With this it is possible to perform energy-dispersive x-ray spectroscopy (EDS) and do chemical analysis of the sample.

The SEM used in this thesis was a Zeiss Supra 25. The main use of the SEM was to perform EDX on a number of samples to confirm the chemical composition while optimizing the growth conditions of the films. EDX measurements are not as sensitive to elements with low atomic numbers, such as carbon, therefore it was mainly used to look at the ratios between the other elements. In particular, it was used to measure the concentration of scandium, chromium and iron when substituting for manganese.

4.4.2 Scanning transmission electron microscopy

A scanning transmission electron microscope (STEM) is a step up from the scanning electron microscope, capable of atomic resolution. This is done by taking a slice from the sample to be measured, called a lamella.

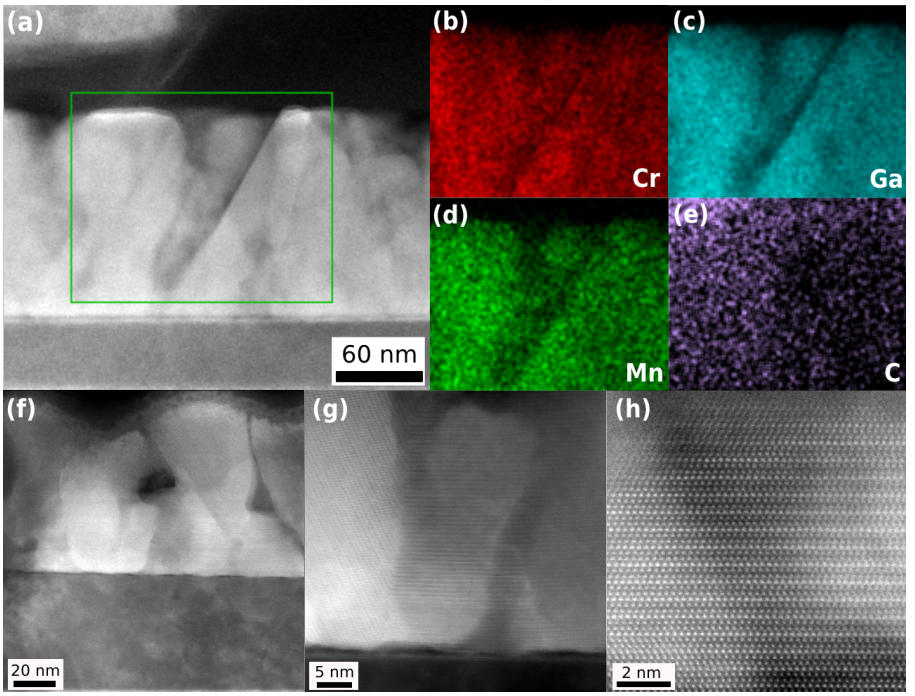

Figure 4.14. An example of a STEM image taken from Paper II showing the $(Mn_{0.78}Cr_{0.22})_2GaC$ phase. (a) STEM-HAADF image with corresponding elemental EDX maps (b-e). (f-h) High resolution images showing atomic resolution capabilities.

The lamella needs to be thinned by ion milling down to around 100 nm or when it has become transmissive to the electron beam. The detector is stationed on the other side of the sample from the electron beam and records the interaction of the electron beam with the sample as it passes through the lamella.

Scanning transmission electron microscopy data for this thesis was collected by a collaborating group at Linköping University using a double corrected, monochromated, high-brightness FEI Titan^3 at 300 kV. The cross-sectional samples were first mechanically polished to a thickness of about 50 μm, followed by ion-beam milling with Ar^+ in a Gatan precision ion polishing system (PIPS) at 5 keV with a final polishing step at 1 keV of ion energies. The results from the STEM were atomic resolution images of the measured films, confirming the MAX phase

crystal structure. Elemental maps with EDX measurements were also done to confirm a uniform distribution of elements in the films, ruling out local clustering or segregation of elements.

5 Overview of results

In this section a brief overview and summary of the main results from the papers will be given. The thought process and initial reasoning for each of the papers will also be discussed. In addition, results from other unpublished or minor experiments will be shown.

5.1 Magnetic ordering in Mn_2GaC

We initially set out to synthesize the Mn_2GaC phase as a starting point before branching out to other solid solutions related to it. However, as the phase was optimized and magnetic measurements performed, it was observed that the low temperature behavior was considerably different from what had previously been reported by Dahlqvist et al. [17]. Previously, the magnetic moment had been seen to increase as the temperature was lowered, increasing to 1.7 μ_B per Mn atom at 3 K and 5 T field. This was contrary to what was observed in these newer films, as they showed only 0.38 μ_B per Mn atom at 5 T field which was fairly constant from 3 K up to about 125 K. This was observed on several samples made at different thicknesses and growth temperatures. This inconsistency in the measurements led us to believe that it was related to the MgO substrate, as minute contamination in the MgO substrates produces a significant signal at low temperatures [75]. Figure 5.1 shows the low temperature measurements on Mn_2GaC films done by Dahlqvist et al. (a) and this work (b). In (b) it can be seen that after subtracting the MgO background, the magnetization at 5 T converges to the same value over the entire temperature range and is mostly linear with no curvature as the field increases. The inset in (b) shows the raw measurements of the film without the background subtraction, where the large effect of the MgO substrate can be seen. If the raw measurements in the inset in (b) are compared to the measurements in (a), it can be seen that the shape of the curves in (a) is quite similar to the MgO background.

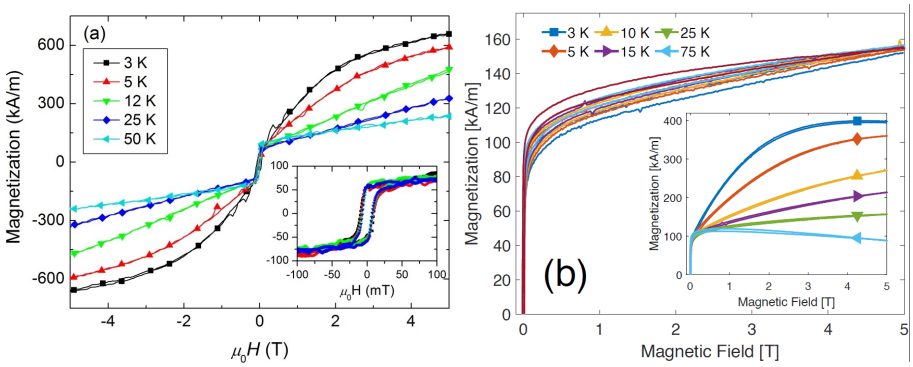

Figure 5.1. Comparison of low temperature measurements of Mn_2GaC with MgO background subtraction. (a) Shows results after background subtraction by Dahlqvist et al., inset is at low field values. (b) Results of background subtraction in Paper I, the inset shows raw measurements where the effects of the MgO substrate on the data can be readily seen. Reprinted (a) with permission from [17], copyright 2016 by the American Physical Society.

In the supplementary data for [17], the background subtraction was described as a bare MgO substrate of the same size and thickness that was measured at several temperatures between 3 K and 15 K. The signal was then expressed as an arctan function with a linear component, which was fitted to the temperatures. This is different from the background subtraction performed in the present work. A bare MgO substrate was measured at every temperature at which the films were measured, and then the background measurement was simply subtracted from the film measurement, resulting in the data seen in Figure 5.1 (b). Considering the results, we believe that this has accurately removed the effects of the MgO substrate. Another factor in the robustness of the background subtraction in this work was that the film thickness was $\sim$ 370 nm while the film measured by Dahlqvist et al. was 100 nm. This gave us a considerably stronger signal to work with but even so, care had to be taken when doing the measurements to ensure everything lined up correctly. In the end, it was concluded that the background subtraction of the MgO substrate in the measurements performed by Dahlqvist et al. did not fully remove the contribution of the substrate. We therefore decided that we should write a paper detailing our findings.

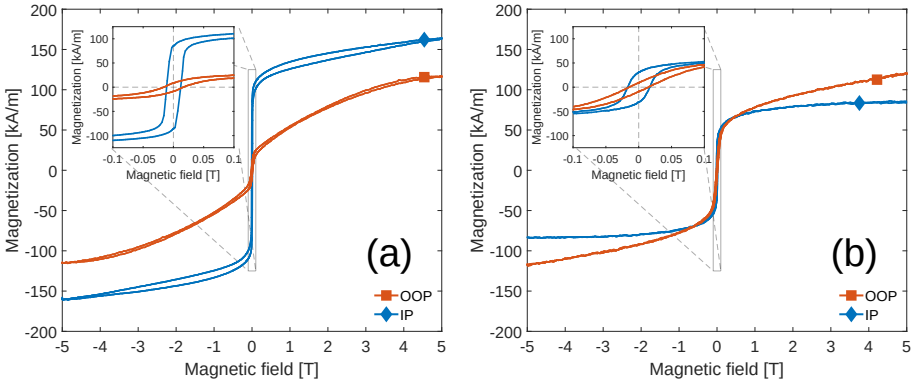

Figure 5.2. Comparison of Mn_2GaC with single or mixed orientations at 100 K with in-plane and out-of-plane measurements. (a) shows the single orientation film, while (b) shows the mixed orientation film. The insets show the low field areas.

However, during optimization before the various Mn-Cr-Fe solid solutions were grown, we obtained several Mn_2GaC samples which were phase pure but had a mixture of two different crystallographic orientations, namely (0006) and $(10\bar{1}3)$. This presented us with the opportunity to investigate the magnetic anisotropy of the phase, which had not been done experimentally before but had been addressed in theoretical calculations [76]. We therefore combined both the low temperature results and magnetic anisotropy results in Paper I.

The mixed orientation film that was synthesized had about 51% of its volume growing with the $(10\bar{1}3)$ orientation parallel to the film plane, while 49% was (0001) oriented. The $(10\bar{1}3)$ plane has an angle of 59° to the (0001) plane. This means that when measuring in the out-of-plane direction on the mixed orientation film, the (0001) planes will be at only a 31° angle to the field, as opposed to 90° for the single orientation film. The result of this can be seen in Figure 5.2. The single orientation film has clear differences in the magnetic response depending on whether measuring in-plane or out-of-plane with respect to the (0001) planes. The mixed orientation film has almost the same behavior whether the field is in- or out-of plane, except for at low field values, where the in-plane has slightly more remanence. This shows that the magnetocrystalline anisotropy has (0001) as easy planes.

5.2 Room temperature ferromagnetism in $(Mn_{1-x}Cr_x)_2GaC$

Both Mn and Cr containing MAX phases have been intensively studied, as described in detail in section 3.2.1. The solid solution of Mn and Cr has been studied considerably before, however, it has always been limited to Cr rich phases while the Mn rich phase has for some reason not been explored before. Density functional theory calculations by Dahlqvist as presented in paper II, showed that for $x \leq 0.5$, the phase could have ferromagnetic ordering, since this magnetic configuration had the lowest formation enthalpy. This was therefore an interesting composition range to study. Previously synthesized samples with $x = 0.5$ were measured from 30 K to 300 K and showed ferromagnetic behavior with magnetization at 5 T of 0.19 μ_B per M atom and remanence of 0.004 μ_B per M atom [52]. The temperature dependence of the remanent and 5 T magnetization in samples with $x = 0.5$ suggested competing magnetic interactions in the system and non-collinear magnetic ordering. Another study of ferromagnetic resonance (FMR) measurements on the $x = 0.5$ phase concluded that there was a ferromagnetic to paramagnetic transition with a critical temperature of ~ 220 K [51]. A study of $x = 0.7$ observed two transitions located at 38 K and 153 K [31]. A bulk synthesis study in the range $0.8 \leq x \leq 0.9$ showed that all the samples had a critical temperature around 50 K. The pure Cr_2GaC phase is paramagnetic [77].

As can be seen in Figure 5.3 as Mn is replaced by Cr, the magnetic properties of the films change considerably. For pure Mn_2GaC, there is a transition from ferromagnetic-like behavior below ~ 210 K to antiferromagnetic behavior with a metamagnetic transition that occurs at higher and higher field values as the temperature is increased. As more Mn is replaced by Cr, this magnetic behavior changes, for $x = 0.06$ it is in an intermediary state with a more complex behavior. When x is increased to 0.12, this complex interaction is replaced by a ferromagnetic behavior. This is where the magnetic signal is at its strongest for these samples, with $T_c = 489$ K. However, as the Cr content is increased further, a decrease in remanence, saturation magnetization and critical temperature is seen. Although there were only four samples synthesized in this work, it has been shown in the literature that for $x = 0.5$ that the critical temperature is already below room temperature at $T_c = 220$ K [51, 52].

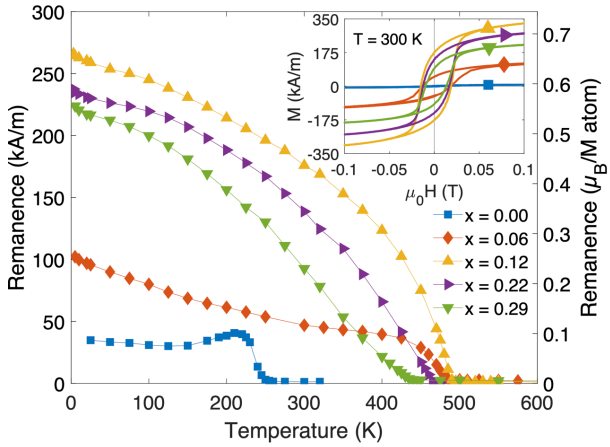

Figure 5.3. Remanence of $(Mn_{1-x}Cr_x)_2GaC$ as a function of temperature. The inset shows the hysteresis loops at 300 K.

From this it can be seen that as the ratio of Cr to Mn in the MAX phase is increased, the critical temperature decreases and trends towards paramagnetic behavior, where $x = 0.29$ has a critical temperature of 440 K, reaching a maximum at $x = 0.12$ at 496 K before decreasing again to 248 K at $x = 0.0$. This is in line with the DFT results in paper II that predict that antiferromagnetism or paramagnetism is more favorable in the high Cr range of the solid solution. Only below $x = 0.5$ does ferromagnetism become the most stable magnetic configuration.

The change in magnetic behavior of the $(Mn_{1-x}Cr_x)_2GaC$ films is linked to changes in the lattice parameters, which affect the exchange interactions both between the atoms within the layers, as well as interactions between layers. This can be seen in Figure 5.4, where the magnetic behavior seems inversely correlated with the change in unit cell volume. The $x = 0.12$ film has the largest magnetization, remanence and critical temperature, while having the smallest volume. The change in the c lattice parameter has a larger effect on the magnetic signal than the a lattice parameter. This can be seen in that a reaches a rather stable value as the amount of Cr is increased, while c is constantly changing.

It would be very interesting to map out the changes in magnetic behavior at low values of x more thoroughly in the future, as well as extending it up to $x = 0.5$, where the signal should go below 300 K.

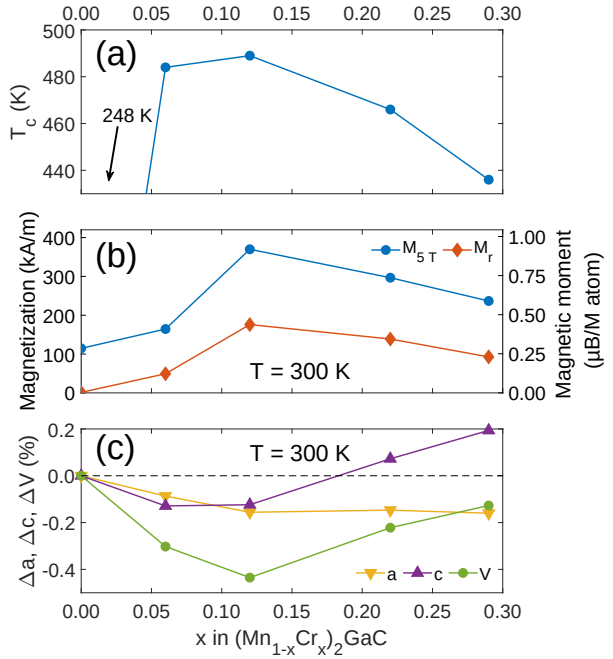

Figure 5.4. Properties of $(Mn_{1-x}Cr_x)_2GaC$ as a function of the composition, x. The top image shows the critical temperature, the middle image shows the magnetization and remanence, while the bottom image shows the changes in the lattice parameters a and c, as well as the unit cell volume V.

Now that a MAX phase with a large ferromagnetic response at and above room temperature has been found, it will open up the possibilities of utilizing MAX phases in applications, such as mentioned in section 3.2.4.

5.3 Magnetic investigation of the *i*-MAX phase $(Mn_{2/3}Sc_{1/3})_2GaC$

We set out to study the $(Mn_{2/3}Sc_{1/3})_2GaC$ MAX phase, as it had not been made in thin film form before and no magnetic measurements had been done on it. Previously, it had been synthesized in bulk by Petruhins et al. [78], and theoretical calculations showed that its magnetic ordering was close to degenerate between FM and AFM, therefore offering interesting prospects for investigations.

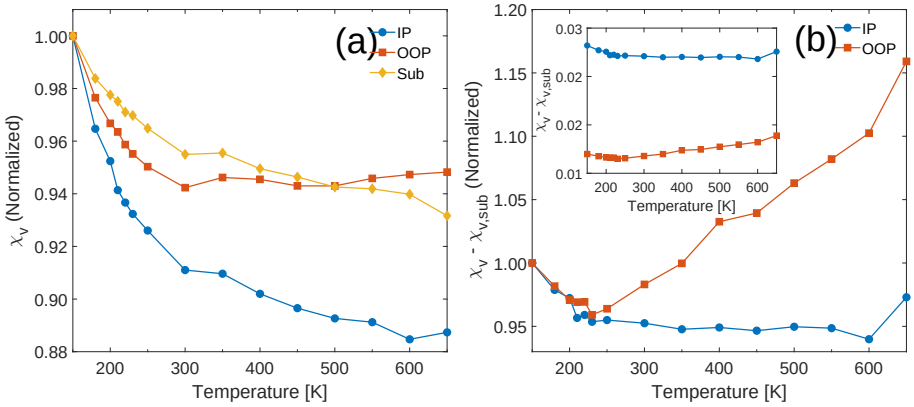

Figure 5.5. Susceptibility measurements of $(Mn_{2/3}Sc_{1/3})_2GaC$. (a) the normalized susceptibility measurements for in-plane and out-of-plane, as well as a bare SiC substrate measured in-plane. (b) The normalized susceptibility after subtracting the substrate measurement. The inset shows the non-normalized data.

During the initial tests of the phase synthesis, several different substrates were used, namely MgO $(1\,1\,1)$, Al_2O_3 $(0\,0\,0\,1)$ and SiC-4H $(0\,0\,1)$. The resulting films were epitaxial on all substrates, but the crystal quality differed considerably, with the $(0\,0\,0\,6)$ XRD peak on SiC-4H$(0\,0\,1)$ having more than twice the area compared to on the MgO and Al_2O_3 substrates. Therefore, most of the focus was on utilizing the SiC substrates during optimization. Initially, the depositions were done at 550 °C, the same as for Mn_2GaC, but it was found that raising the temperature increased the quality of the film slightly and we therefore settled on 720 °C as the optimum temperature. This is a higher temperature than is possible for the pure Mn_2GaC phase, as the competing Mn_3GaC will start forming preferentially once the temperature is increased above 600 °C in that case.

The *i*-MAX structure was confirmed by TEM imaging, but they also revealed that the film formed in grain-like islands. This could also be seen in an SEM image, where there are larger plates with smaller crystals in between.

Magnetic measurements were done on the samples and it could be seen that the films did not have any significant signal. To investigate whether they were paramagnetic or antiferromagnetic, the susceptibility was in-

vestigated as a function of temperature. The susceptibility of the sample decreases more rapidly with temperature at first but notably there is a distinct difference between the in-plane and out-of-plane response. The susceptibility perpendicular to the plane starts to increase with temperature above approximately 200 K whereas the in-plane susceptibility decreases monotonically. This difference is seen clearer with the substrate susceptibility subtracted, as shown in Figure 5.5 (b), revealing the susceptibility of the film only. Here, the susceptibility in the in-plane direction is seen to be almost temperature independent whereas in the out-of-plane direction it increases with temperature. This is consistent with the behavior of antiferromagnets below the Néel temperature where the susceptibility is temperature independent in the direction perpendicular to the magnetization ($\chi_\perp$ constant) and increasing with temperature parallel to the magnetization ($\chi_\parallel$ increasing). Therefore, we concluded that this was antiferromagnetic with the spins aligned with the out-of-plane direction. With the measurements that were done on the samples, we could not confirm the Néel temperature of the phase, and this remains a potential investigation in the future.

Furthermore, considering how a small amount of Mn substituted with Cr in the $(Mn_{1-x}Cr_x)_2GaC$ phase changed the magnetic behavior considerably, from being antiferromagnetic at room temperature to being ferromagnetic up to 480 K, then it might be of interest to perform similar substitution in the future with the $(Mn_{2/3}Sc_{1/3})_2GaC$ phase as well.

5.4 Polycrystalline $(Mn_{1-x}Cr_x)_2GaC$ on Si

Having the ability to synthesize Mn_2GaC-based MAX phases without using single-crystal substrates would expand the utility of them considerably. Therefore, successful growth on Si substrates with the native oxide is an important benchmark.

During the growth session of the $(Mn_{1-x}Cr_x)_2GaC$ films, which was the fourth and final growth session, three substrates were included: MgO which was a known good substrate for Mn_2GaC films, $MgAl_2O_3$ which we had tested before and found to also give good quality films, and Si which had been tested before in the first growth session but had not given good results at the time. The Si substrate was included as a test with low

expectations. However, during optimization of the growth parameters for Mn_2GaC prior to including Cr, the Si substrate surprisingly gave good results. A single test with a SiO_2/Si substrate with 100 nm of thermal oxide was also tested, this also gave a decent quality film but not quite as good as Si with the native oxide. No further growths were done on substrates with thermally grown oxide.

As stated above, some tests with Si substrates were performed during the first growth session, when initially attempting to synthesize the Mn_2GaC phase. Although the phase was successfully made on a MgO substrate, during the same growth, nothing was seen on an a Si substrate. Therefore, no more attempts with Si were made until the fourth growth session. A potential explanation for the different results this time was that the power on the magnetrons was increased, resulting in a higher growth rate compared to the previous three sessions. This was done to decrease the time taken to make thicker films. Along with the high quality films on Si, another difference in the fourth session was that almost all the films in this session had the $(10\bar{1}3)$ orientation also growing in the plane of the films. This was even though the substrates were mainly MgO(111), which should give films with $(000l)$ orientations. Due to the limited time and number of MgO substrates at the time of the fourth session, the effect of growth rate could not be studied in more detail. However, recently while remaking and expanding the Cr doped series, mainly for the purpose of making larger and thicker samples for neutron diffraction measurements, the growth rate was reduced. This caused poor quality films on Si, as well as a greatly reduced amount of $(10\bar{1}3)$ in the plane of the film. This seems to indicate a connection between the growth rate and the formation of the MAX phase on Si substrates.

The initial series grown on Si included $x = 0$, 0.06, 0.12, 0.22 and 0.29. X-ray diffraction measurements on them showed that they were mostly phase pure, with $x = 0.06$ and 0.29 showing minor peaks that seem to belong to Cr. Pole figure measurements showed that they were polycrystalline with $(000l)$ texture.

Magnetic measurements were performed as a function of angle with a VSM, both in-plane and out-of-plane. The in-plane measurements showed that all films were isotropic in the plane of the substrate, as expected from textured films with no in-plane ordering. However, in-

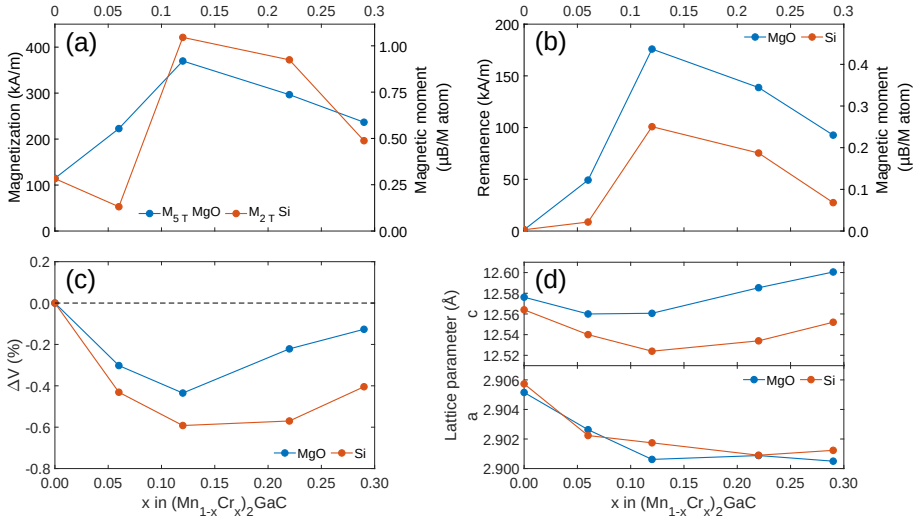

Figure 5.6. Comparison of $(Mn_{1-x}Cr_x)_2GaC$ on MgO and Si as a function of composition x. (a) Magnetization at 5 T for MgO and 2 T for Si (b) Remanence. (c) Relative changes in crystal lattice volume. (d) The a and c lattice parameters.

plane to out-of-plane measurements showed that the films had an easy-plane response along the surface of the films, except for $x = 0.06$, which curiously had a nearly isotropic response. The $x = 0.06$ film is therefore almost completely isotropic in all directions, a stark contrast to the other films as well as the pure Mn_2GaC phase.

As can be seen in Figure 5.6 the saturation magnetization for $x = 0.12$ and $x = 0.22$ was stronger for the Si substrates compared to MgO. However, the remanent moment was considerably smaller for all films on Si substrates, as can be seen in (b). Preliminary measurements of the temperature dependence of the magnetization indicate that the critical temperature is similar to that of films grown on MgO(1 1 1) but this data has not been published yet.

The relative volume change is greater on the Si substrates compared to on MgO, as Figure 5.6 (c) shows. This is caused by a greater change in the *c* lattice constant between the substrates, since the changes in the *a* lattice constant are almost the same whether on the MgO or Si substrates as seen in (d). The changes in the lattice parameters seem to correlate with changes in magnetization, but further work would be needed to expand

upon this further.

This study has shown that a MAX phase with a ferromagnetic response can be grown on Si substrates and is therefore not limited to epitaxial films on crystalline substrates.

5.5 Other unpublished results

Here we present a few other results that have not yet been put together in a manuscript.

5.5.1 Mn_2GaC on Si

The published articles with films grown on Si focused on $(Mn_{1-x}Cr_x)_2GaC$, but an interesting result that did not fit within those publications was the temperature dependence of the magnetization of the pure Mn_2GaC on Si. Figure 5.7 (a) shows from the remanence that the transition temperature from ferromagnetic to antiferromagnetic for Mn_2GaC grown on Si is roughly 25 K lower than on MgO substrates. However, the single and mixed orientation films on MgO found in paper I, had the same (higher) transition temperature.

The main difference between the films grown on MgO and Si, is that the films are single crystalline on MgO while textured on Si. Pole figure measurements presented in papers I and IV show that on MgO the films have well defined crystal orientations, while on Si there is a ring feature showing that the crystallites do not have a preferred in-plane orientation, although aligned in the out-of-plane direction. There is also a minor difference in that the lattice parameters on Si are slightly smaller, resulting in a volume change of -0.28% and -0.07% compared to the single and mixed orientation films, respectively. The difference in lattice parameters and strain state could explain the lower transition temperature in the films grown on Si.

5.5.2 $(Mn_{1-x}Fe_x)_2GaC$

One of the goals of the last growth session was to investigate the possibility of incorporating Fe into the Mn_2GaC MAX phase. Although the main focus ended up being on the $(Mn_{1-x}Cr_x)_2GaC$ phase, some inter-

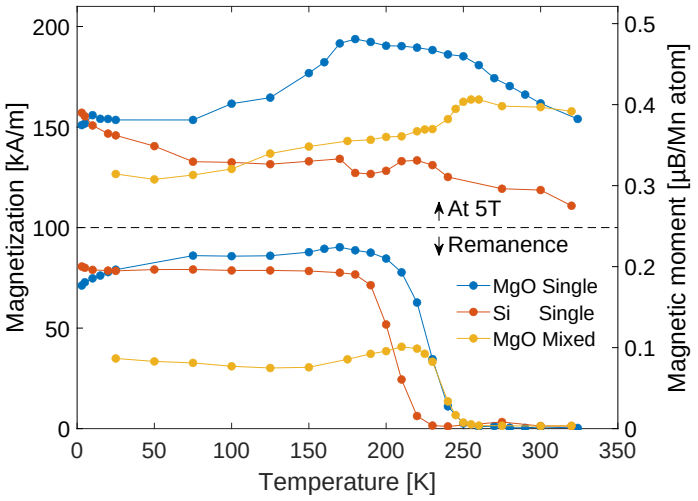

Figure 5.7. Magnetization at 5 T and remanence as a function of temperature for Mn_2GaC on MgO and Si. Shown is both single- and mixed orientation of Mn_2GaC on MgO. The films are not fully saturated at 5 T and the values here are the total magnetization, not just the extracted FM component, which has been presented previously.

esting results also came from a few depositions with Fe. Unpublished theoretical work by Martin Dahlqvist, predicted that up to 25% Fe could be substituted for Mn and these compositions should be ferromagnetic. Another theoretical work by Draganyuk et al. predicts the same up to 12.5% [79]. This was the motivation for the following samples.

X-ray diffraction measurements in Figure 5.8 show that Fe is being substituted into the MAX phase, since there is a concomitant shift in the $(10\bar{1}3)$ and (0006) peak position with increasing Fe ratio. However, there is also an immediate formation of an $(Mn_{1-x}Fe_x)_3GaC$ antiperovskite phase [80, 81]. It can be seen that the MAX phase remains even up to $x = 0.21$, in line with the theoretical calculations, however at $x = 0.38$ it is completely gone. A peak appears for $x = 0.10$ and above marked by a black square that could belong to either Fe_3Ga or $FeGa_3$.

Further optimization of the growth conditions could not be done due to time constraints. Possible changes in the sputter rate or temperature of the deposition could improve the formation conditions of the $(Mn_{1-x}Fe_x)_2GaC$ MAX phase over the $(Mn_{1-x}Fe_x)_3GaC$ antiperovskite

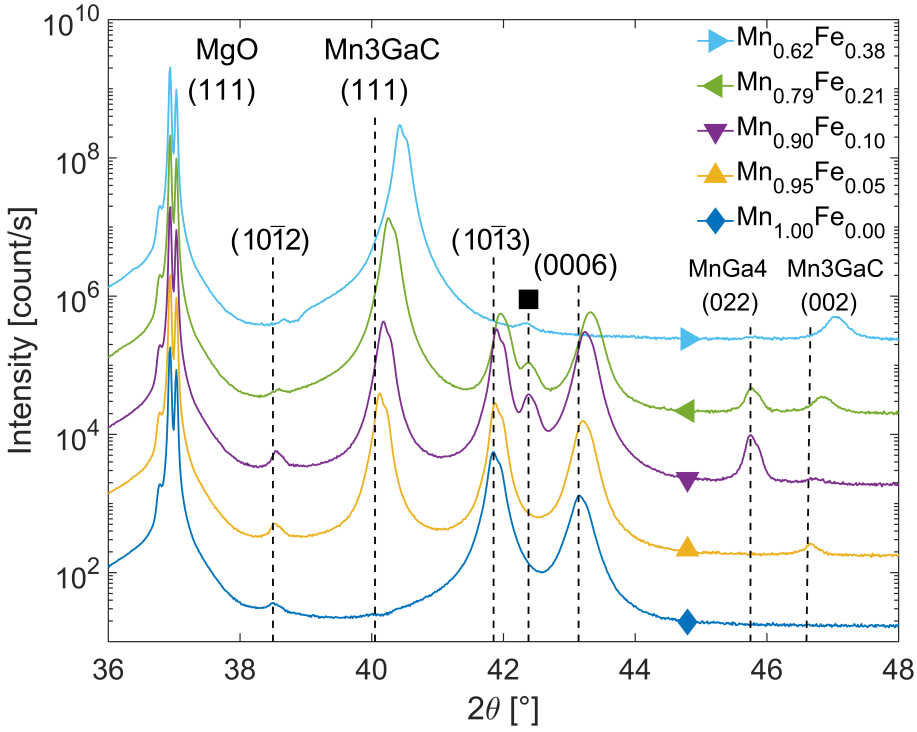

Figure 5.8. XRD of $(Mn_{1-x}Fe_x)_2GaC$ in the range $x = 0$ to $x = 0.38$. Peak marked by the black square are unconfirmed. Not measured with a monochromator, resulting in both Kα1 and Kα2 peaks being present.

phase. For example, at or above 600 °C there is an increased formation of Mn_3GaC while depositing for Mn_2GaC. Therefore, it might still remain possible to achieve a phase pure sample of $(Mn_{1-x}Fe_x)_2GaC$, for example by lowering the temperature, but this will require further study.

Due to the presence of the antiperovskite $(Mn_{1-x}Fe_x)_3GaC$ competing phase, magnetic measurements of $(Mn_{1-x}Fe_x)_2GaC$ samples may not be fully representative of the $(Mn_{1-x}Fe_x)_2GaC$ MAX phase. Figure 5.9 shows the VSM measurements of the films. To give a comparison with the $(Mn_{1-x}Cr_x)_2GaC$ series, the $(Mn_{88}Cr_{12})_2GaC$ is also included in the figure, as that was the film with the highest magnetic moment of that series. All Fe-containing films showed ferromagnetic behavior but their critical temperatures were below the transition temperature of 210 K for Mn_2GaC, as can be seen from the remanent magnetization in Figure 5.9. It remains unknown how much the antiperovskite phase contributes to

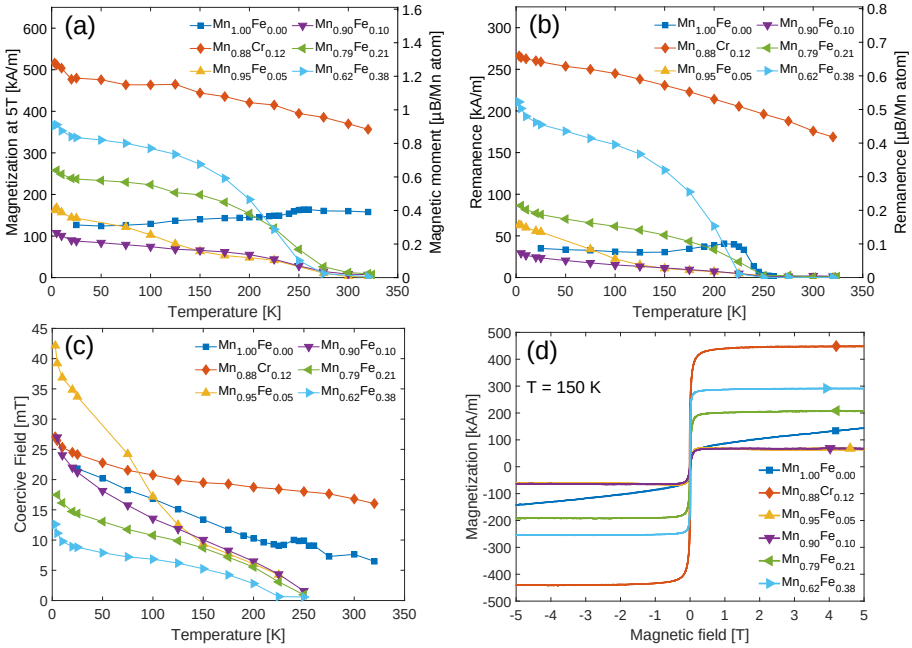

Figure 5.9. VSM results as a function of temperature for $(Mn_{1-x}Fe_x)_2GaC$ in the range $x = 0$ to $x = 0.38$. Included also are the pure Mn_2GaC phase, as well as $(Mn_{0.88}Cr_{0.12})_2GaC$ for reference. (a) Saturation magnetization, (b) remanence, (c) coercive field and (d) Hysteresis loops done at 150 K.

the total signal and therefore the data is simply presented as is. The observed trend is that as the Fe ratio is increased, so does the saturation magnetization and remanence, while the coercive field decreases. It should also be remembered that at $x = 0.38$, the MAX phase no longer forms. It is therefore clear that even if the signal from films with $x \leq 0.21$ originates from the MAX phase, it is much weaker than that from the Cr containing film.

It can be seen from these preliminary results that this avenue of research into the solid solution of Fe in Mn_2GaC is still quite interesting.

5.5.3 $(Mn_{1-x-y}Fe_xCr_y)_2GaC$

The x-ray characterization of the $(Mn_{1-x}Cr_x)_2GaC$ and $(Mn_{1-x}Fe_x)_2GaC$ series showed that both Fe and Cr could be substituted for Mn in the

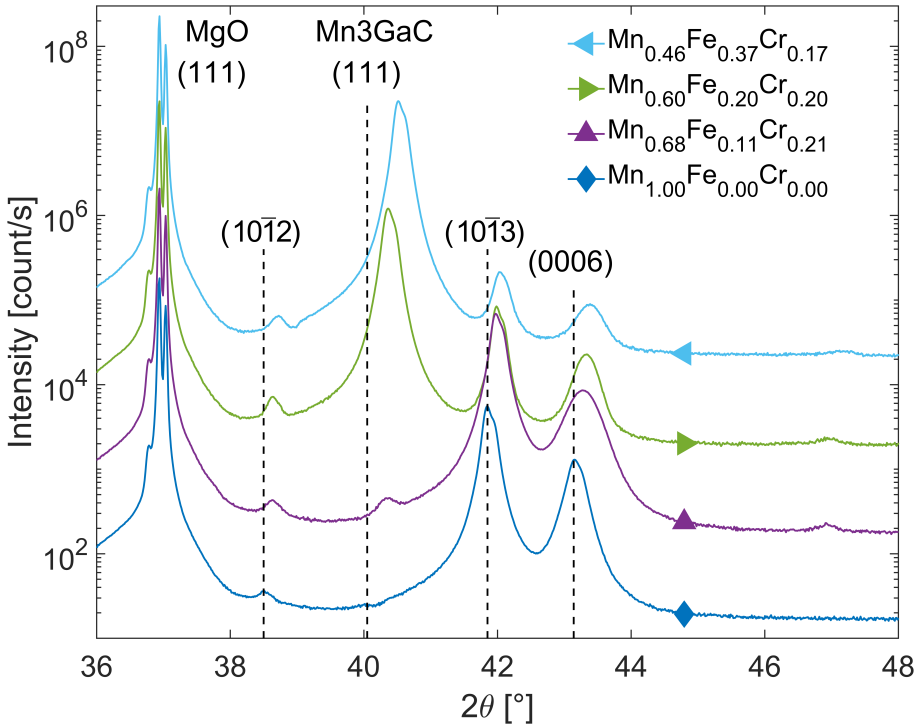

Figure 5.10. XRD of $(Mn_{1-x-y}Fe_xCr_y)_2GaC$ with x from 0 to 0.37 and $y \sim 0.20$. Not measured with a monochromator, resulting in both Kα1 and Kα2 peaks being present.

Mn_2GaC phase but while Cr substitution gave phase pure MAX phase films, Fe substitution resulted in the formation of an antiperovskite competing phase. This led to the idea that more Fe could potentially be incorporated in the MAX phase by alloying with both Fe and Cr at the same time. The Cr value of $y = 0.2$ was chosen and a limited growth series was made with varying Fe content.

Figure 5.10 shows the XRD results. It can be seen that all films show the formation of the MAX phase, even at $x = 0.37$, $y = 0.17$. However, only $x = 0.11$, $y = 0.21$ remained mostly phase pure, with both the other films having significant antiperovskite competing phase. This shows that Cr has a stabilizing effect on the inclusion of Fe in the solid solution, since even $x = 0.05$ without Cr was enough to form the competing phase.

The results from magnetic measurements on the films can be seen in

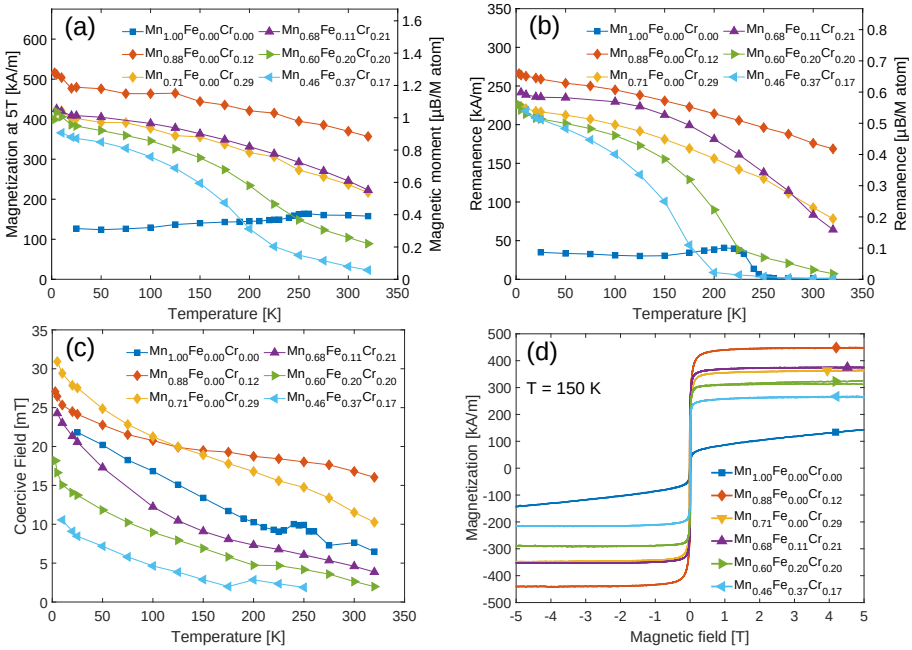

Figure 5.11. VSM results as a function of temperature for $(Mn_{1-x-y}Fe_xCr_y)_2GaC$ with x between 0 to 0.37 and $y \sim 0.20$. Included also are the pure Mn_2GaC phase, as well as $(Mn_{1-y}Cr_y)_2GaC$ with y = 0.12 and 0.22 for reference. (a) Saturation magnetization at 5 T, (b) remanence, (c) coercive field and (d) Hysteresis loops done at 150 K.

Figure 5.11. Also included are both the pure Mn_2GaC phase (squares) as well as two films from the $(Mn_{1-y}Cr_y)_2GaC$ phase (diamonds), y = 0.12 which was the strongest magnetization, as well as $y = 0.29$, which has roughly the same Mn concentration as the $x = 0.11$ film. Figure 5.11 (a) shows the magnetization at 5 T field. The almost phase pure film of $x = 0.11$, $y = 0.21$, which has the highest magnetization of this series, is comparable to the $x = 0$, $y = 0.29$. Therefore, this substitution of Cr for Fe does not have a large impact on the magnetization, although it can be seen in (b) that the remanence is slightly higher at low temperatures but falls off faster as the temperature is increased. The $x = 0$, $y = 0.29$ film has a critical temperature of $T_c = 436$ K, while we roughly estimate that T_c for the corresponding Fe containing film is 380 K (by extrapolation of the curve to zero remanent magnetization). In (c), it can be seen that adding Fe instead of Cr significantly lowers the coercive field for all

the films. For the other two Fe containing films, it can be seen in both magnetization and remanence that they have a change in slope around 225 K and 200 K for the $x = 0.20$ and 0.37 respectively. This might stem from different contributions from the MAX phase and antiperovskite phase.

These initial results are quite interesting and with with further optimization of the growth conditions, perhaps it is possible to reduce the amount of antiperovskite phase present in the films, but that remains the subject of a future study. Additionally, showing that Cr can stabilize some inclusion of Fe in the Mn_2GaC phase, also opens up the question of whether Ni or Co could also be stabilized, instead of Fe?

6 Conclusions & outlook

This thesis has investigated the MAX phase Mn_2GaC and several variations of it by substituting Mn with other elements. The overall aim has been to explore how the magnetic properties of this interesting materials system can be tuned and the magnetization enhanced by alloying with other transition metals on the M site. To this end, thin MAX phase films were grown by direct-current magnetron sputtering (dcMS) with elemental targets, with a specially made crucible and setup for the liquid Ga target. This allowed for good control over the composition of the deposited films.

Initially, the plan was not to investigate Mn_2GaC beyond a successful synthesis as a basis to branch out from and confirm the results from the literature. After the first samples were synthesized and while doing magnetic measurements, it was noted that the low temperature response did not align with the previous results in the literature. This was found to be due to insufficient background subtraction of the MgO background at low temperature, below 50 K, inflating the measured moment. This result was presented in paper I. This paper also investigated two thin films of Mn_2GaC on MgO (001) substrates, one with only (0001) planes and another with a mix of $(10\bar{1}3)$ and (0001) planes parallel to the substrate surface. This allowed for a comparison of the behavior of the in- and out-of-plane magnetic responses to show that Mn_2GaC has an (0001) easy magnetic plane. This result had previously been predicted by theory [76] but has now been confirmed experimentally.

As an interesting magnetic system, Mn_2GaC has been studied considerably before [8, 17, 19, 42–47, 49]. However, the nature of its magnetic ordering remains uncertain to this day, with helical ordering currently the most likely structure, both above and below its magnetic transition around 210 K [18, 19]. This thesis does not tackle this aspect of the MAX phase, however, a series of samples with different thicknesses deposited on both MgO and Si during this work could help to refine the current

understanding thanks to NMR measurements which are being carried out by collaborators.

The *i*-MAX phase $(Mn_{2/3}Sc_{1/3})_2GaC$ was synthesized in thin film form for the first time. Theoretical calculations had predicted that its magnetic ordering could be close to degenerate between ferromagnetism and antiferromagnetism [78]. Bulk samples that had been synthesized before by Petruhins et al. [78] were not phase pure enough for magnetic measurements and therefore the question of the magnetic order remained. The results in paper III, show that the phase is antiferromagnetic, with indications that the spins align out of the plane.

We investigated a compositional region in which a small fraction of Mn in Mn_2GaC was substituted by Cr, producing the phase $(Mn_{1-x}Cr_x)_2GaC$ over the range $0.06 < x < 0.29$. This region had not been studied before, however, several studies had been performed for $x = 0.5$ and above [41, 50–55, 58]. Previous results for $x = 0.5$ showed weak ferromagnetism with critical temperatures between 220 K [50] and up to around room temperature [52]. For $x \geq 0.7$, all had critical temperatures below 160 K with Cr_2GaC being paramagnetic [77]. The new results for $x < 0.3$ showed a significant ferromagnetic response well above room temperature, with all samples having critical temperatures between 440 K and 490 K. The one at $x = 0.12$ had the strongest moment, with M_s and M_r of 370 kA/m and 176 kA/m, respectively, and a coercive field of 16.8 mT at room temperature. This is the first time a strongly ferromagnetic MAX phase with a critical temperature above room temperature has been characterized.

With films deposited at the same time on both MgO and Si, the Si substrates showed stronger magnetization values for $x = 0.12$ (+14%) and 0.22 (+25%), while having considerably lower remanence in all samples. The critical temperature for the films grown on Si is similar to that of the films on MgO. This shows that the MAX phase is not limited to epitaxial depositions only. With its decently strong ferromagnetic response and critical temperatures reaching ~ 215 °C (489 K), $(Mn_{1-x}Cr_x)_2GaC$ can be seriously considered for practical applications.

An interesting future prospect is to continue with a more detailed study of the $(Mn_{1-x}Cr_x)_2GaC$ compound, where more values of x will be investigated to fully map out the magnetic response as a function of Cr content. It would be interesting to examine both the very low x range,

where it transitions from the Mn_2GaC behavior to having a ferromagnetic-like response above room temperature at $x = 0.06$, as well as studying the region around $x = 0.12$ to find the true maximum in moment. At the time of writing, this work is ongoing with a new batch of samples. However, more detailed measurements are still needed. In addition, the precise nature of the magnetic ordering in the $(Mn_{1-x}Cr_x)_2GaC$ phase is still unknown. For example, the bulk magnetometry measurements cannot distinguish between ferromagnetism, ferrimagnetism or other more complex non-collinear magnetic arrangements. Therefore, neutron diffraction measurements are underway, which should be able to address this question.

The incorporation of Fe in the $(Mn_{1-x}Fe_x)_2GaC$ phase was investigated. X-ray results show that Fe does indeed seem to be going into the MAX phase structure, however, even at a low concentration of 0.05% Fe a competing antiperovskite phase appears. Perhaps it might be possible to reduce this competing phase by altering the growth conditions, as these samples were simply deposited with the same settings as for Mn_2GaC. Following on from the Fe series, another promising avenue was studied where Fe was incorporated along with Cr in $(Mn_{1-x-y}Fe_xCr_y)_2GaC$. The result was that Cr seems to have a stabilizing effect on the MAX phase formation. An almost phase pure film with $x = 0.11$, $y = 0.21$ was synthesized. The small three-sample series already done shows promise with further optimization possible. Having already seen some promise with Fe, it might be possible to try a similar approach with either Ni or Co as well, instead of Fe.

Yet another question would be the impact of making an *i*-MAX phase with $(Mn_{1-x}Cr_x)$. For example, is it possible for $((Mn_{1-x}Cr_x)_{2/3}Sc_{1/3})_2GaC$ to be made? We have shown that $(Mn_{1-x}Cr_x)_2GaC$ has a ferromagnetic response, but how is the response after disturbing the M-planes with *i*-MAX ordering?

Several interesting avenues have now opened up with a confirmed ferromagnetic MAX phase above room temperature and there are various ways to try to improve or change the magnetic behavior in future studies. The realm of magnetic MAX phases still contains numerous mysteries to unravel.

Bibliography

(1) Dahlqvist, M.; Barsoum, M. W.; Rosen, J. *Materials Today* **2024**, *72*, 1–24.

(2) Barsoum, M. W.; El-Raghy, T. *Journal of the American Ceramic Society* **1996**, *79*, 1953–1956.

(3) Sokol, M.; Natu, V.; Kota, S.; Barsoum, M. W. *Trends in Chemistry* **2019**, *1*, 210–223.

(4) Naguib, M.; Barsoum, M. W.; Gogotsi, Y. *Advanced Materials* **2021**, *33*, 2103393.

(5) VahidMohammadi, A.; Rosen, J.; Gogotsi, Y. *Science* **2021**, *372*, eabf1581.

(6) Salim, O.; Mahmoud, K. A.; Pant, K. K.; Joshi, R. K. *Materials Today Chemistry* **2019**, *14*, 100191.

(7) Subba, C. B.; Rai, D. P.; Tursunov, M. E.; Dekhkonov, A. T.; Pachuau, Z. *Qeios* **2025**, DOI: 10.32388/A3QP41.

(8) Novoselova, I. P.; Petruhins, A.; Wiedwald, U.; Ingason, Á. S.; Hase, T.; Magnus, F.; Kapaklis, V.; Palisaitis, J.; Spasova, M.; Farle, M.; Rosen, J.; Salikhov, R. *Scientific Reports* **2018**, *8*, 2637.

(9) Zurek, S., *Encyclopedia Magnetica*, https://www.e-magnetica.pl, 2023.

(10) Cullity, B. D.; Graham, C. D., *Introduction to Magnetic Materials*, 2nd ed.; Wiley-IEEE Press: 2008.

(11) Zurek, S., *Bethe-Slater Curve, CC0, via Wikimedia Commons*, https://commons.wikimedia.org/wiki/File:Bethe-Slater_curve_by_Zureks.svg, 2009.

(12) Slater, J. C. *Phys. Rev.* **1930**, *36*, 57–64.

(13) Slater, J. C. *Phys. Rev.* **1930**, *35*, 509–529.

(14) Mader, S.; Nowick, A. S. *Applied Physics Letters* **1965**, *7*, 57–59.

(15) Blundell, S., *Magnetism in Condensed Matter*; Oxford University Press: 2001.

(16) Ashcroft, N. W.; Mermin, N. D., *Solid State Physics*; Holt, Rinehart and Winston: 1976.

(17) Dahlqvist, M.; Ingason, A. S.; Alling, B.; Magnus, F.; Thore, A.; Petruhins, A.; Mockute, A.; Arnalds, U. B.; Sahlberg, M.; Hjörvarsson, B.; Abrikosov, I. A.; Rosen, J. *Phys. Rev. B* **2016**, *93*, 014410.
(18) Dey, J.; Jedryka, E.; Kalvig, R.; Wiedwald, U.; Farle, M.; Rosen, J.; Wójcik, M. *Phys. Rev. B* **2023**, *108*, 054413.
(19) Tao, Q.; Mockute, A.; Orlandi, F.; Khalyavin, D.; Manuel, P.; Palsson, G.; Ouladdiaf, B.; Rosen, J.; Boothroyd, A. T. *Journal of Physics: Condensed Matter* **2025**, *37*, 175802.
(20) Zhang, J.; Liu, B.; Wang, J. Y.; Zhou, Y. C. *Journal of Materials Research* **2009**, *24*, 39–49.
(21) Lin, Z.; Zhuo, M.; Zhou, Y.; Li, M.; Wang, J. *Journal of the American Ceramic Society* **2006**, *89*, 3765–3769.
(22) Kudielka, H.; Rohde, H. *Z. Kristallogr., Kristallgeom., Kristallphys., Kristallchem* **1960**, *114*, 447–456.
(23) Liu, Z.; Wu, E.; Wang, J.; Qian, Y.; Xiang, H.; Li, X.; Jin, Q.; Sun, G.; Chen, X.; Wang, J.; Li, M. *Acta Materialia* **2014**, *73*, 186–193.
(24) Tao, Q.; Dahlqvist, M.; Lu, J.; Kota, S.; Meshkian, R.; Halim, J.; Palisaitis, J.; Hultman, L.; Barsoum, M. W.; Persson, P. O.; Rosen, J. *Nature Communications* **2017**, *8*, 14949.
(25) Dahlqvist, M.; Lu, J.; Meshkian, R.; Tao, Q.; Hultman, L.; Rosen, J. *Science Advances* **2017**, *3*, e1700642.
(26) Eklund, P.; Beckers, M.; Jansson, U.; Högberg, H.; Hultman, L. *Thin Solid Films* **2010**, *518*, 1851–1878.
(27) Ingason, A. S.; Petruhins, A.; Rosen, J. *Materials Research Letters* **2016**, *4*, 152–160.
(28) Eklund, P.; Rosen, J.; Persson, P. O. Å. *Journal of Physics D: Applied Physics* **2017**, *50*, 113001.
(29) Biswas, A.; Natu, V.; Puthirath, A. B. *Oxford Open Materials Science* **2021**, *1*, itab020.
(30) Ingason, A. S.; Mockute, A.; Dahlqvist, M.; Magnus, F.; Olafsson, S.; Arnalds, U. B.; Alling, B.; Abrikosov, I. A.; Hjörvarsson, B.; Persson, P. O. Å.; Rosen, J. *Phys. Rev. Lett.* **2013**, *110*, 195502.
(31) Mockute, A.; Persson, P. O. Å.; Magnus, F.; Ingason, A. S.; Olafsson, S.; Hultman, L.; Rosen, J. *physica status solidi (RRL) – Rapid Research Letters* **2014**, *8*, 420–423.
(32) Hamm, C. M.; Bocarsly, J. D.; Seward, G.; Kramm, U. I.; Birkel, C. S. *Journal of Materials Chemistry C* **2017**, *5*, 5700–5708.

(33) Sobolev, K.; Gorshenkov, M.; Manfrinetti, P.; Peddis, D.; Pazniak, A.; Rodionova, V. *Ceramics International* **2021**, *47*, 21069–21076.
(34) Sobolev, K.; Pazniak, H.; Farle, M.; Rodionova, V.; Wiedwald, U. *Journal of Materials Chemistry C* **2021**, *9*, 16516–16522.
(35) Pazniak, H.; Stevens, M.; Dahlqvist, M.; Zingsem, B.; Kibkalo, L.; Felek, M.; Varnakov, S.; Farle, M.; Rosen, J.; Wiedwald, U. *ACS Applied Nano Materials* **2021**, *4*, 13761–13770.
(36) Lin, S.; Huang, Y.; Zu, L.; Kan, X.; Lin, J.; Song, W.; Tong, P.; Zhu, X.; Sun, Y. *Journal of Alloys and Compounds* **2016**, *680*, 452–461.
(37) Li, Y. et al. *Applied Physics Reviews* **2021**, *8*, 031418.
(38) Li, Y. et al. *The Journal of Physical Chemistry Letters* **2023**, *14*, 481–488.
(39) Li, Y.; Lu, J.; Li, M.; Chang, K.; Zha, X.; Zhang, Y.; Chen, K.; Persson, P. O. Å.; Hultman, L.; Eklund, P.; Du, S.; Francisco, J. S.; Chai, Z.; Huang, Z.; Huang, Q. *Proceedings of the National Academy of Sciences* **2020**, *117*, 820–825.
(40) Chen, L.; Li, Y.; Zhao, B.; Liu, S.; Zhang, H.; Chen, K.; Li, M.; Du, S.; Xiu, F.; Che, R.; Chai, Z.; Huang, Q. *Advanced Science* **2023**, *10*, 2206877.
(41) Mockute, A.; Lu, J.; Moon, E. J.; Yan, M.; Anasori, B.; May, S. J.; Barsoum, M. W.; and, J. R. *Materials Research Letters* **2015**, *3*, 16–22.
(42) Ingason, A. S.; Petruhins, A.; Dahlqvist, M.; Magnus, F.; Mockute, A.; Alling, B.; Hultman, L.; Abrikosov, I. A.; Persson, P. O. Å.; Rosen, J. *Materials Research Letters* **2014**, *2*, 89–93.
(43) Ingason, A. S.; Pálsson, G. K.; Dahlqvist, M.; Rosen, J. *Phys. Rev. B* **2016**, *94*, 024416.
(44) Lyaschenko, S.; Maximova, O.; Shevtsov, D.; Varnakov, S.; Tarasov, I.; Wiedwald, U.; Rosen, J.; Ovchinnikov, S.; Farle, M. *Journal of Magnetism and Magnetic Materials* **2021**, *528*, 167803.
(45) Berzins, A.; Smits, J.; Petruhins, A.; Grube, H. *Materials Chemistry and Physics* **2021**, *272*, 124972.
(46) Jönsson, H. J. M.; Ekholm, M.; Leonov, I.; Dahlqvist, M.; Rosen, J.; Abrikosov, I. A. *Physical Review B* **2022**, *105*, 035125.
(47) Vysotin, M. A.; Tarasov, I. A.; Fedorov, A. S.; Varnakov, S. N.; Ovchinnikov, S. G. *JETP Letters* **2022**, *116*, 323–328.

(48) Thorsteinsson, E. B.; Ingason, A. S.; Magnus, F. *Phys. Rev. Mater.* **2023**, *7*, 034409.
(49) Tarasov, I.; Visotin, M.; Nazarova, Z.; Nazarov, A.; Varnakov, S.; Ovchinnikov, S. *physica status solidi (RRL) – Rapid Research Letters* **2025**, *19*, 2400279.
(50) Lai, C.-C.; Tao, Q.; Fashandi, H.; Wiedwald, U.; Salikhov, R.; Farle, M.; Petruhins, A.; Lu, J.; Hultman, L.; Eklund, P.; Rosen, J. *APL Materials* **2018**, *6*, 026104.
(51) Salikhov, R.; Semisalova, A. S.; Petruhins, A.; Ingason, A. S.; Rosen, J.; Wiedwald, U.; Farle, M. *Materials Research Letters* **2015**, *3*, 156–160.
(52) Petruhins, A.; Ingason, A. S.; Lu, J.; Magnus, F.; Olafsson, S.; Rosen, J. *Journal of Materials Science* **2015**, *50*, 4495–4502.
(53) Flatten, T.; Matthes, F.; Petruhins, A.; Salikhov, R.; Wiedwald, U.; Farle, M.; Rosen, J.; Bürgler, D. E.; Schneider, C. M. *Applied Physics Letters* **2019**, *115*, 094101.
(54) Yan, M.; Li, C.; Zou, Y.; Yang, M. *Journal of Wuhan University of Technology-Mater. Sci. Ed.* **2020**, *35*, 363–367.
(55) Maniv, A.; Reyes, A. P.; Ramakrishna, S. K.; Graf, D.; Huq, A.; Potashnikov, D.; Rivin, O.; Pesach, A.; Tao, Q.; Rosen, J.; Felner, I.; Caspi, E. N. *Journal of Physics: Condensed Matter* **2020**, *33*, 025803.
(56) Thorsteinsson, E. B.; Dahlqvist, M.; Elsukova, A.; Petruhins, A.; Persson, P. O. Å.; Rosen, J.; Ingason, A. S.; Magnus, F. *APL Materials* **2023**, *11*, 121102.
(57) Mockute, A.; Dahlqvist, M.; Emmerlich, J.; Hultman, L.; Schneider, J. M.; Persson, P. O. Å.; Rosen, J. *Physical Review B* **2013**, *87*, 094113.
(58) Lin, S.; Tong, P.; Wang, B. S.; Huang, Y. N.; Lu, W. J.; Shao, D. F.; Zhao, B. C.; Song, W. H.; Sun, Y. P. *Journal of Applied Physics* **2013**, *113*, 053502.
(59) Liu, Z.; Waki, T.; Tabata, Y.; Nakamura, H. *Physical Review B* **2014**, *89*, 054435.
(60) Tao, Q. Z.; Hu, C. F.; Lin, S.; Zhang, H. B.; Li, F. Z.; Qu, D.; Wu, M. L.; Sun, Y. P.; Sakka, Y.; Barsoum, M. W. *Materials Research Letters* **2014**, *2*, 192–198.

(61) Rivin, O.; Caspi, E. N.; Pesach, A.; Shaked, H.; Hoser, A.; Georgii, R.; Tao, Q.; Rosen, J.; Barsoum, M. W. *Materials Research Letters* **2017**, *5*, 465–471.
(62) Waki, T.; Liu, Z.; Tabata, Y.; Nakamura, H. *Journal of Physics: Conference Series* **2017**, *868*, 012007.
(63) Boucher, R.; Berger, O.; Leyens, C. *Surface Engineering* **2016**, *32*, 172–177.
(64) Siebert, J. P.; Mallett, S.; Juelsholt, M.; Pazniak, H.; Wiedwald, U.; Page, K.; Birkel, C. S. *Mater. Chem. Front.* **2021**, *5*, 6082–6091.
(65) Liu, Z.; Takao, K.; Waki, T.; Tabata, Y.; Nakamura, H. *Journal of Physics: Conference Series* **2017**, *868*, 012016.
(66) Momma, K.; Izumi, F. *Journal of Applied Crystallography* **2011**, *44*, 1272–1276.
(67) Tao, Q.; Salikhov, R.; Mockute, A.; Lu, J.; Farle, M.; Wiedwald, U.; Rosen, J. *APL Materials* **2016**, *4*, 086109.
(68) Gou, B.; Wang, L.; Ye, B.; Meng, C.; Li, X.; Chen, Q.; Yang, T.; Xu, W. *Journal of Materials Science: Materials in Electronics* **2021**, *32*, 13081–13088.
(69) Sun, S.; Ma, Z.; Chen, Z.; Liu, P.; Song, Y.; Lu, Q.; Fu, X.; Wang, Q.; Cui, W. *Acta Materialia* **2023**, *242*, 118479.
(70) Chen, Z.; Chong, H.; Sun, S.; Yang, J.; Yao, G.; Wang, Q.; Zhu, J.; Yang, S.; Cui, W. *Scripta Materialia* **2022**, *213*, 114596.
(71) Panda, K.; Potashnikov, D.; Pesach, A.; Barbier, M.; Eyal, A.; Ouisse, T.; Keren, A.; Bachar, N. Magnetic Order and Magneto-Elasticity in the Electronic Excitations of Gd-i-MAX, 2024.
(72) Yahav, D.; Maniv, A.; Potashnikov, D.; Pesach, A.; Caspi, E. N.; Reyes, A. P.; Tao, Q.; Rosen, J.; Maniv, E. Hidden magnetic phases in i-MAX compounds, 2024.
(73) Petruhins, A.; Ingason, A. S.; Olafsson, S.; Rosen, J. *Materials Research Express* **2020**, *7*, 106102.
(74) Lewis, L. H.; Yoder, D.; Moodenbaugh, A. R.; Fischer, D. A.; Yu, M.-H. *Journal of Physics: Condensed Matter* **2006**, *18*, 1677.
(75) Khalid, M.; Setzer, A.; Ziese, M.; Esquinazi, P.; Spemann, D.; Pöppl, A.; Goering, E. *Phys. Rev. B* **2010**, *81*, 214414.
(76) Dahlqvist, M.; Rosen, J. *Scientific Reports* **2020**, *10*, 11384.
(77) Liu, Z.; Waki, T.; Tabata, Y.; Yuge, K.; Nakamura, H.; Watanabe, I. *Phys. Rev. B* **2013**, *88*, 134401.

(78) Petruhins, A.; Dahlqvist, M.; Lu, J.; Hultman, L.; Rosen, J. *Crystal Growth & Design* **2020**, *20*, 55–61.
(79) Draganyuk, O. N.; Zamkova, N. G.; Zhandun, V. S. *Journal of Magnetism and Magnetic Materials* **2022**, *563*, 169860.
(80) Medkour, Y.; Roumili, A.; Saoudi, A.; Louail, L.; Maouche, D. *MATEC Web of Conferences* **2013**, *5*, 04042.
(81) Ivanovskii, A. L.; Sabiryanov, R. F.; Skazkin, A. N. *Physics of the Solid State* **1998**, *40*, 1516–1519.

7 Publications

Paper I

Magnetic ordering and magnetocrystalline anisotropy in epitaxial Mn_2GaC MAX phase thin films

E.B. Thorsteinsson, A. S. Ingason, F. Magnus

Physical Review Materials, 2023, Vol. 7, 034409

https://doi.org/10.1103/PhysRevMaterials.7.034409

Contributions: Synthesized the samples, performed all measurements, carried out all data analysis and co-authored the paper.

Magnetic ordering and magnetocrystalline anisotropy in epitaxial Mn_2GaC MAX phase thin films

Einar B. Thorsteinsson [1], Arni S. Ingason [2], and Fridrik Magnus [1]
[1]Science Institute, University of Iceland, Dunhaga 3, 107 Reykjavik, Iceland
[2]Grein Research ehf., Dunhaga 5, 107 Reykjavik, Iceland

(Received 16 December 2022; revised 22 February 2023; accepted 24 February 2023; published 23 March 2023)

Mn_2GaC is a MAX phase belonging to a family of naturally nanolaminated materials with formula $M_{n+1}AX_n$ ($n = 1, 2, 3$), where M is a transition metal, A is an A-group element, and X is carbon or nitrogen. It has a complex magnetic phase diagram, and there are many open questions regarding its magnetic properties. Here we study epitaxial films of Mn_2GaC with two different crystal orientations on MgO(1 1 1) substrates: a (0 0 0 l) dominated orientation and a mixed (0 0 0 l) and (1 0 $\bar{1}$ 3) orientation. Magnetic measurements between 3 and 320 K are presented for in-plane and out-of-plane magnetic fields on both types of film, which show that Mn_2GaC has a magnetocrystalline anisotropy with (0 0 0 l) as easy planes. This provides clear experimental evidence of the anisotropic properties associated with the nanolaminated structure of a MAX phase. In addition, a close look at the magnetic response at low temperature shows that the noncollinear magnetic state is unchanged below 50 K, contrary to previous results, with a magnetic moment of 0.38 μ_B per Mn atom at a temperature of 3 K and applied field of 5 T.

DOI: 10.1103/PhysRevMaterials.7.034409

I. INTRODUCTION

Low-dimensional magnetism has seen a surge in interest in recent years fueled by the discovery of an increasing number of layered van der Waals crystals [1–3]. The reduced dimensions and potential for competing interactions open up the possibility of exotic magnetic ordering beyond conventional ferro- or antiferromagnetism. MAX phases are another family of naturally nanolaminated materials composed of a transition metal (M), an A-group element (A), and either carbon or nitrogen (X) with the chemical formula $M_{n+1}AX_n$ ($n = 1, 2, 3$) [4]. They have an atomically layered structure which for $n = 1$ has the order M-A-M-X-M-A-M-X. The first magnetic MAX phase, $(Cr_{0.75}Mn_{0.25})_2GeC$, was synthesized [5] in 2013, and since then a small number of other phases containing either Mn or Cr on the M site have shown interesting magnetic properties [6–11]. These properties arise due to the frustrated coupling between M-site atoms both within the M-X-M trilayers and across the A layers. Such frustrated magnetic systems can be a source of complex spin textures such as spin spirals and skyrmions, which could potentially be used in magnetic storage and logic devices [12].

In particular, Mn_2GaC has been shown to have a rich magnetic phase diagram which makes it of interest not only in magnetoelectric applications but also for magnetocalorics [6,11,13]. At low temperature it exhibits noncollinear antiferromagnetic ordering, and at ~210 K it undergoes a magnetic phase transition to collinear antiferromagnetic ordering. The magnetic phase transition coincides with a structural phase transition, where an abrupt change in the c-axis lattice parameter takes place [6]. The coupled magnetic and structural phase transition can also be induced by applying a magnetic field at temperatures above 210 K. This complex magnetic behavior is a result of competing ferromagnetic and antiferromagnetic exchange interactions within and between the M layers as shown by first-principles calculations and Monte Carlo simulations. However, many questions remain about its magnetic ordering, particularly the noncollinear antiferromagnetic state at low temperature [14,15]. Furthermore, there has yet to be presented any experimental evidence of magnetocrystalline anisotropy in Mn_2GaC, despite its highly anisotropic nanolaminated structure [9,16]. Both subjects are important to gain the thorough understanding of this materials system which is necessary if its properties are to be tuned to a specific application.

Here we examine the magnetic ordering and anisotropy in epitaxial films of Mn_2GaC. We use two single-phase Mn_2GaC samples with different epitaxial relationships with the substrate to determine the presence of magnetocrystalline anisotropy. Furthermore, we carefully characterize the magnetic response of Mn_2GaC at low temperature in order to elucidate the low-temperature magnetic state.

II. EXPERIMENT

The films were grown by direct current magnetron sputtering (dcMS) on 1×1 cm^2 MgO(111) substrates from a 7.5-cm-diameter 99.9% manganese target, a 7.5-cm 99.99% carbon target, and a liquid gallium target made from 99.9999% gallium pellets. The Ga was held in a specially made 5.0-cm copper crucible which was mounted on a standard circular magnetron at the bottom of the vacuum chamber. During sputtering the Ga target was maintained in liquid form by limiting the flow of cooling water through the magnetron. The magnetrons were arranged in a confocal geometry with a target-substrate distance of approximately 160 mm. The sputtering was carried out in a 20-SCCM (cubic centimeters per minute at STP) flow of 99.999% purity argon gas using a throttle valve to adjust the pressure to 0.40 Pa. The vacuum chamber had a base pressure of below 5×10^{-7} Pa; however,

at the growth temperature of 550 °C the base pressure rose to 5×10^{-6} Pa. For the duration of the growth the sample holder was rotated by ±360° at a rate of 12 rpm. The substrates were cleaned in an ultrasonic bath for 5 min in acetone followed by 5 min of ethanol and then annealed *in situ* in vacuum at 600 °C for 60 min immediately prior to growth.

The Mn and C growth rates were determined by growing single films of Mn and C and measuring thickness by x-ray reflectometry (XRR). This approach is not applicable to Ga due to its low melting point, and therefore its growth rate was estimated by growing a series of $MnGa_x$ films with a known Mn rate and performing composition analysis with energy dispersive x-ray spectroscopy (EDS) in a scanning electron microscope (SEM). In all cases, an excess of Ga is needed to form the MAX phase, which ends up diffusing to the surface of the film. This is consistent with other MAX phases, where an excess of the A-group element (A) is often critical [17,18].

Two representative films with different crystallographic orientations are discussed here (see below). Film 1 was grown with power values of 45 W for Mn, 10.6 W for Ga, and 206 W for C, giving an estimated atomic flux of 4.60×10^{14}, 3.55×10^{14}, and 2.35×10^{14} atoms/cm^2 s, respectively. The thickness of film 1 was estimated to be 375 nm. This estimation was achieved by growing a thinner film which was measurable by XRR and then scaling that thickness with the increased growth duration of the thicker film. Film 2 was grown with approximately 35% higher flux of Mn and C and 20% higher flux of Ga. Film 2 was estimated to be 140 nm by a similar process as before.

The structural properties of the films were investigated by x-ray diffraction using a Panalytical Empyrean diffractometer in line focus mode. For diffraction, the incident side had a two-bounce hybrid monochromator with a 1/8° divergence slit, and the diffracted side had a PIXcel^{3D} detector operating in one-dimensional (1D) mode. For pole figures, the same incident side optics were used, but a 0.04-rad Soller slit and a 0.27° parallel plate collimator were used on the diffracted side with the detector in open mode. The magnetic properties were measured by vibrating sample magnetometry (VSM) in the range from 3 to 320 K with a 5 T cryogen-free magnet system from Cryogenic.

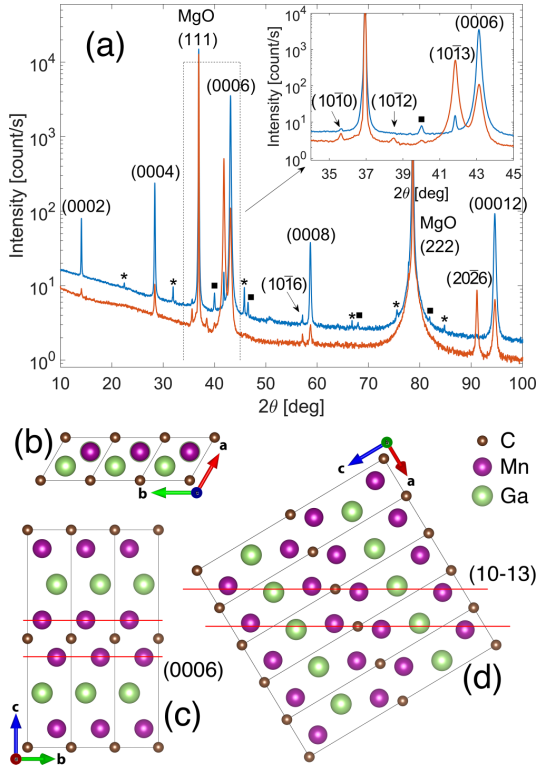

FIG. 1. (a) XRD scans of the two films, where the blue top curve is the single-orientation film and the red bottom curve is the mixed-orientation film. Peaks marked with a star are from $MnGa_4$, whereas squares are from Mn_3GaC. The inset is focused on the (0 0 0 6) and (1 0 $\bar{1}$ 3) peaks. Below are crystal structure schematics of Mn_2GaC: (b) and (c) have three unit cells visible, while (d) has six. (b) shows the top view, while (c) and (d) show the side views with the (0 0 0 6) and (1 0 $\bar{1}$ 3) lattice spacing highlighted, respectively.

III. RESULTS AND DISCUSSION

A. Film structure

Figure 1(a) shows x-ray diffraction (XRD) measurements for the two samples. Both films are an almost phase-pure Mn_2GaC MAX phase with film 1 only having very minor contaminants of Mn_3GaC and $MnGa_4$. These are thermodynamically stable competing phases which are often present in varying amounts in Mn_2GaC samples. The relative intensities of the Mn_3GaC and $MnGa_4$ peaks are consistent with randomly oriented polycrystalline phases. By comparing the area of the Mn_3GaC(1 1 1) and $MnGa_4$(2 2 0) peaks with that of the Mn_2GaC(0 0 0 6) peak, which are the 100, 100, and 18% relative intensity peaks of their respective phase, we can estimate that the concentration of Mn_3GaC is 0.024% and the concentration of $MnGa_4$ is 0.032%. Film 1 grows epitaxially with the (0 0 0 l) planes parallel to the MgO(1 1 1) planes. A very small peak corresponding to the (1 0 $\bar{1}$ 3) planes is also seen in film 1, indicating that 0.05% of grains grow with the (1 0 $\bar{1}$ 3) planes parallel to the MgO(111) planes. These "tilted grains" have been observed previously in other epitaxial MAX phase films such as Cr_2GeC [17]. The nucleation of (1 0 $\bar{1}$ 3) oriented grains probably occurs at film dislocations, which are ubiquitous due to the relatively large lattice mismatch between the film and the substrate. The adatom mobility and A-group element concentration could also be contributing factors [17]. Film 2 has no detectable contaminant phases but has a significant portion of (1 0 $\bar{1}$ 3) oriented grains parallel to the substrate surface. The relative x-ray peak intensities of the (1 0 $\bar{1}$ 3) and (0 0 0 6) planes are 100 and 18%, respectively. Integrating the area under the peaks, we can estimate that in film 2 the (1 0 $\bar{1}$ 3) oriented grains account for 51% of the film with 49% being (0 0 0 6). From reciprocal space map measurements (not shown) on film 1 we find that the lattice parameters are $c = 12.574 \pm 0.002$ Å and $a = 2.906 \pm 0.002$ Å, and for film 2 fitting the (1 0 $\bar{1}$ 3) and

(0 0 0 6) peaks in the XRD scan results in $c = 12.576 \pm 0.002$ Å and $a = 2.905 \pm 0.002$ Å. Both films have relatively large mosaicity, as seen by the full width at half maximum (FWHM) of the rocking curves on their principal peaks, which is around 1.3° (not shown) for both (0 0 0 6) peaks and 2.4° for the (1 0 $\bar{1}$ 3) peak. This is significantly larger than the FWHM of the MgO(111) rocking curve. However, we stress that both films are single-phase Mn_2GaC (discounting the minuscule amounts of impurity phases) and only the epitaxial relationship with the substrate differs. Film 1 we refer to as having a *single orientation*, whereas film 2 has *mixed orientations*.

Figures 1(b)–1(d) are schematics of the crystal structure of Mn_2GaC illustrating the *M*-*A*-*M*-*X*-*M*-*A*-*M*-*X* layered nature, drawn using the program Visualization for Electronic and Structural Analysis (VESTA) [19]. Figure 1(b) shows a top view of the unit cells, and Fig. 1(c) shows a side view, where the red lines indicate the distance between the (0 0 0 6) planes. Film 1 is almost entirely oriented with the *c* lattice vector of the MAX phase perpendicular to the film plane as shown in Fig. 1(c). The orientation of the tilted grains in film 2 is shown in Fig. 1(d), where the tilted (1 0 $\bar{1}$ 3) lattice planes are indicated with red lines. Film 2 is composed of grains with both (0 0 0 6) and (1 0 $\bar{1}$ 3) orientations.

Pole figures were obtained to examine the epitaxial relationship of the film and substrate further. The measurements were performed at $2\theta = 41.84°$, i.e., for the (1 0 $\bar{1}$ 3) planes, which are at an azimuthal angle of $\chi = 59.0°$ with respect to the (0 0 0 l) planes, as seen in Fig. 2(a). The single-crystal nature of film 1 can be seen from the discrete sixfold symmetric points. Film 2 in Fig. 2(b), which has a mixed orientation, has (1 0 $\bar{1}$ 3) peaks both in the center and at $\chi = 59.0°$. Additional peaks on both sides of the principal peaks can also be seen which are most likely a result of twinning. However, it should be noted that Fig. 2 is on a logarithmic scale and on a linear scale these additional peaks are barely visible with the peak in the center being dominant.

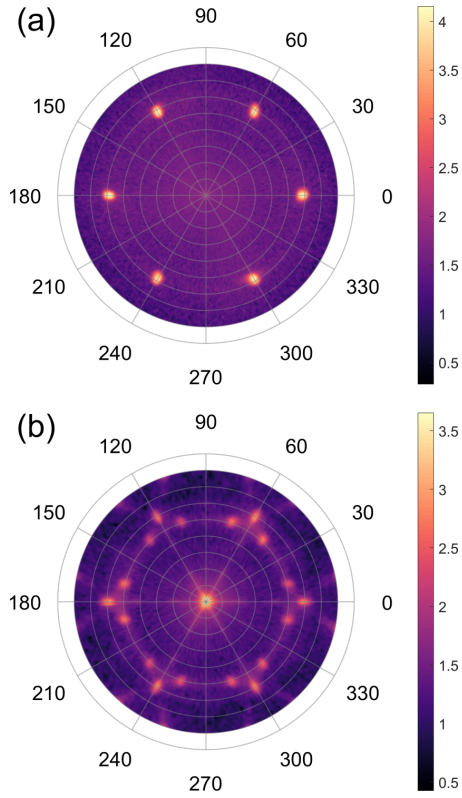

FIG. 2. Pole figures at $2\theta = 41.84°$ for the (1 0 $\bar{1}$ 3) peak of the films. (a) is a single orientation (0 0 0 6) film, while (b) has (1 0 $\bar{1}$ 3) and (0 0 0 6) mixed orientations. It should be noted that the intensity scale is logarithmic and in (b) most of the intensity is in the center spot.

B. Magnetic properties

Mn_2GaC has a complex magnetic phase diagram which has been studied previously both experimentally and theoretically, but questions remain about the nature of the magnetic ordering at different temperatures [6,11,13,20,21]. Figure 3(a) shows the in-plane magnetic response of the single-orientation sample at high temperatures showcasing the metamagnetic transition. The inset shows out-of-plane measurements at the same temperatures. At low temperatures the film exhibits ferromagnetic-like (FM-like) behavior with a significant remanent magnetization of 0.18 μ_B/Mn atom. At ∼210 K a magnetic phase transition occurs to an antiferromagnetic (AFM) state, but a metamagnetic transition is observed at increasingly high fields with increasing temperature. These results are broadly the same as in previous studies, although the increased film thickness gives a significantly improved signal-to-noise ratio. The low amount of impurity phases (see above) means that their contribution to the measured magnetic signal is negligible. $MnGa_4$ has recently been shown to be antiferromagnetic with a Néel temperature of 393 K [22], but in the concentrations found here its magnetic signal is not measurable. Similarly, Mn_3GaC is known to be antiferromagnetic below 170 K and then ferromagnetic between 170 and 270 K [23]. We do not see any clear signs of this in our data due to the minute amounts of Mn_3GaC in our samples. This, together with the near-single-phase nature of our films, means that the measured magnetic signal can only originate from the Mn_2GaC.

The magnetic model presented in Ref. [6] to explain the high-temperature regime is denoted as AFM$[0001]_4^A$ and has four adjacent Mn layers with collinear spins with a spin flip across every second Ga layer (the *A* layer). This is an AFM configuration with zero remanent moment. Theory suggests that the low-temperature magnetic state is a so-called canted AFM$[0001]_4^A$ state, where each block of four collinear Mn spins is canted by a small angle in the same direction, thus producing a net remanent magnetic moment at zero field. The AFM and canted AFM states are almost degenerate in energy for small angles, and therefore an applied magnetic field can nudge the system from fully AFM to canted AFM, which is the observed metamagnetic transition at high temperatures [6,16,24]. Ferrimagnetic ordering was also considered but was found to be less stable than both the FM and AFM

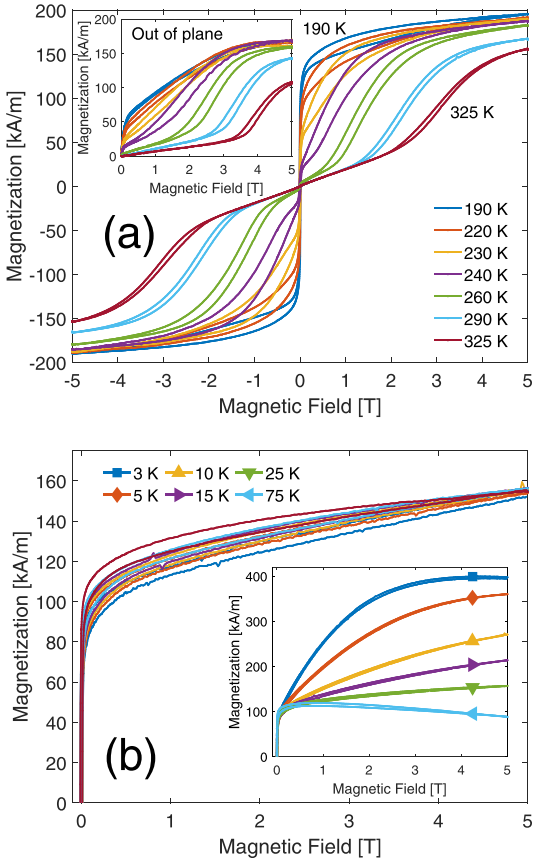

FIG. 3. (a) In-plane magnetization measurements for selected temperatures above the magnetic phase transition, with the inset showing out-of-plane measurements. All the measurements have had the MgO background subtracted. (b) Magnetization measurements at low temperatures (below the magnetic phase transition) with the background from the MgO substrate subtracted. The inset shows the raw measurements without background subtraction.

configurations [6]. However, a recent study has found that at low temperatures the coupling of the magnetic moments of the Mn across Ga layers is more complex than previously thought [14], and therefore there is still some doubt as to the precise magnetic ordering at low temperatures.

Previous studies have shown that the high-field magnetization (sometimes referred to as the saturation magnetization) increases sharply at temperatures below 50 K, which has been interpreted as an increase in the canting angle of the noncollinear AFM state [6]. However, low-temperature measurements of the magnetic properties of epitaxial Mn_2GaC films are complicated by the fact that the MgO substrate itself has a significant and increasing S-shaped magnetic response as the temperature is reduced below 50 K. This is due to magnetic impurities which are invariably present in single-crystal MgO substrates [5,6,11]. This means that to extract the magnetic hysteresis loop of the film at low temperatures, it is necessary to account for the MgO background signal accurately. Figure 3(b) shows magnetization measurements between 3 and 75 K with the MgO background subtracted for the single-orientation film, while the inset shows the raw data. Background subtraction was done by measuring a MgO substrate from the same batch at the same temperatures as the film, and this signal was then subtracted from the film measurements. Care is needed to match the position and orientation of both film and substrate in the VSM, in order not to overcompensate or undercompensate the MgO contribution. Our results show that the magnetization at 5 T remains almost constant throughout this temperature range, at a value of 155 kA/m or 0.38 μ_B/Mn atom. This is contrary to what has been previously reported by Dahlqvist *et al.* [6], where an increasing magnetization was observed with decreasing temperature, up to 1.7 μ_B/Mn atom at 3 K and 5 T field, which is more than four times the magnetization seen here. However, since the thickness of the films studied here is almost four times larger than in previous studies, the background subtraction is much more robust, and therefore these results provide convincing evidence that the magnetization is in fact relatively constant over the entire low-temperature regime. This in turn shows that if the low-temperature state is that of canted AFM spins, the canting angle is constant with temperature.

Another hitherto unresolved question is that of magnetic anisotropy in MAX phases. MAX phases are naturally nanolaminated, which means that they have a highly anisotropic crystal structure. Theoretical calculations by Dahlqvist and Rosen [16] for Mn_2GaC predict that the easy axis is along the (0 0 0 l) planes and that the magnetic anisotropy energy can be affected by strain engineering [21]. Previous experimental studies of magnetism in MAX phases have been on either bulk samples with randomly oriented crystal grains or on epitaxial thin films with the *c*-axis perpendicular to the film plane [25]. Neither case is ideal for determining the magnetocrystalline anisotropy. Randomly oriented grains will give a net zero anisotropy, and in the epitaxial films the shape anisotropy is parallel with the Mn-C-Mn laminae, which means that it is impossible to separate shape anisotropy from magnetocrystalline anisotropy. Therefore the single-orientation and mixed-orientation films studied here present a unique opportunity to compare the magnetic responses along different well-defined crystallographic directions.

Figure 4 shows such a comparison of the magnetic response of the two films at 100 K when the field is applied parallel and perpendicular to the film plane. For the single-orientation film in Fig. 4(a) there is a considerable difference between in-plane (IP) and out-of-plane (OOP) measurements. The remanent magnetization is very small perpendicular to the film plane, and the magnetization at 5 T is also considerably smaller in the OOP direction. This is a fingerprint of in-plane magnetic anisotropy, but since the shape anisotropy favors in-plane magnetization, we cannot draw any conclusions about the possible contribution from magnetocrystalline anisotropy. The result for the mixed-orientation film [Fig. 4(b)] is strikingly different. Here the hysteresis curves are very similar in the IP and OOP directions, although the remanence is still greater in plane. From the structural characterization we

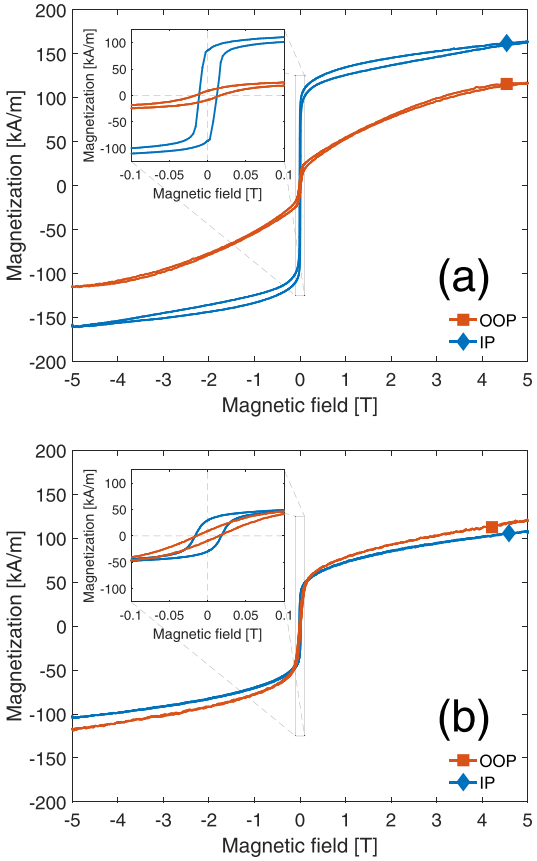

FIG. 4. Hysteresis measurements at 100 K. (a) and (b) show the in-plane and out-of-plane measurements of the single- and mixed-orientation films, respectively. The insets show a smaller field range around zero.

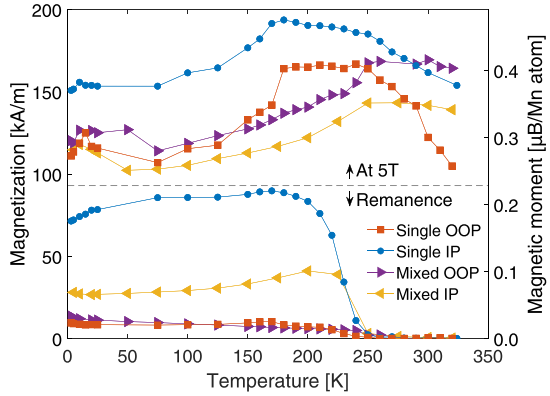

FIG. 5. Magnetization at 5 T and remanence as a function of temperature for the single- and mixed-orientation films in both in-plane and out-of-plane measurements.

estimated that 51% of the mixed-orientation film is composed of (1 0 $\bar{1}$ 3) oriented grains which are at an angle of 59° with respect to the (0 0 0 l) planes. This means that in 51% of the film, the (0 0 0 l) planes are at an angle of only 31° with respect to the film normal, i.e., the OOP direction. It is clear that this has a significant effect on the magnetic response, lowering the energy barrier against rotating the magnetization perpendicular to the plane. This shows that Mn_2GaC has a magnetocrystalline anisotropy with (0 0 0 l) as the easy planes.

The same qualitative differences between IP and OOP magnetization in the single- and mixed-orientation films are observed over the entire temperature range studied. The mixed-orientation film has similar hysteresis loops IP and OOP, whereas the single-orientation film shows clear differences in magnetic response depending on whether the field is applied parallel or perpendicular to the (0 0 0 l) planes. This is also evident in the AFM high-temperature regime, where the metamagnetic transition occurs at a higher field in the OOP measurements, as can be seen in Fig. 3(a). It should be noted that neither film appears to be fully saturated at the maximum field of 5 T, and this applies both IP and OOP.

Figure 5 shows the magnetization at 5 T as well as the remanence over the range 3–320 K. At the noncollinear to collinear AFM phase transition the remanence decreases sharply down to close to zero. The mixed-orientation film has considerably lower remanence in the IP direction than the single-orientation film over the whole range; however, both are similarly low in the OOP direction. The magnetization at 5 T is larger OOP than IP for the mixed-orientation sample which is opposite to what is observed for the single-orientation sample. As noted previously, this is because the mixed-orientation sample has a large fraction of (1 0 $\bar{1}$ 3) oriented grains, which means that the (0 0 0 l) easy planes are closer to the OOP direction than the IP direction. The steep drop in magnetization in the single-orientation sample OOP is a manifestation of the metamagnetic transition shifting to fields above 5 T, which means that we are unable to complete the metamagnetic transition with the maximum available field.

IV. CONCLUSIONS

We have synthesized epitaxial films of Mn_2GaC with two different growth orientations on MgO(1 1 1) substrates. The samples are either (0 0 0 l) dominated or a mix of (0 0 0 l) and (1 0 $\bar{1}$ 3) orientations, as shown by detailed XRD characterization. Magnetization measurements were carried out in the range 3–320 K. By careful subtraction of the MgO background we were able to show that the high-field magnetization (at 5 T) is almost constant at temperatures below 50 K instead of increasing sharply, as has been previously reported, indicating a temperature-independent canting angle in the noncollinear AFM state. Comparison of the magnetic response of the differently oriented films shows that Mn_2GaC has a magnetocrystalline anisotropy with (0 0 0 l) as the easy planes, which is in agreement with theoretical calculations in the literature. These results demonstrate

how the nanolaminated structure of a MAX phase results in anisotropic magnetic properties. This key insight further secures the place of magnetic MAX phases among low-dimensional magnetic materials.

ACKNOWLEDGMENTS

This work was funded by the University of Iceland Research Fund and the Icelandic Research Fund (Grants No. 174271 and No. 217843).

[1] N. Samarth, Magnetism in flatland, Nature (London) **546**, 216 (2017).

[2] B. Huang, G. Clark, E. Navarro-Moratalla, D. R. Klein, R. Cheng, K. L. Seyler, D. Zhong, E. Schmidgall, M. A. McGuire, D. H. Cobden, W. Yao, D. Xiao, P. Jarillo-Herrero, and X. Xu, Layer-dependent ferromagnetism in a van der Waals crystal down to the monolayer limit, Nature (London) **546**, 270 (2017).

[3] C. Gong, L. Li, Z. Li, H. Ji, A. Stern, Y. Xia, T. Cao, W. Bao, C. Wang, Y. Wang, Z. Q. Qiu, R. J. Cava, S. G. Louie, J. Xia, and X. Zhang, Discovery of intrinsic ferromagnetism in two-dimensional van der Waals crystals, Nature (London) **546**, 265 (2017).

[4] M. W. Barsoum, The $M_{N+1}AX_N$ phases: A new class of solids: Thermodynamically stable nanolaminates, Prog. Solid State Chem. **28**, 201 (2000).

[5] A. S. Ingason, A. Mockute, M. Dahlqvist, F. Magnus, S. Olafsson, U. B. Arnalds, B. Alling, I. A. Abrikosov, B. Hjörvarsson, P. O. Å. Persson, and J. Rosen, Magnetic Self-Organized Atomic Laminate from First Principles and Thin Film Synthesis, Phys. Rev. Lett. **110**, 195502 (2013).

[6] M. Dahlqvist, A. S. Ingason, B. Alling, F. Magnus, A. Thore, A. Petruhins, A. Mockute, U. B. Arnalds, M. Sahlberg, B. Hjörvarsson, I. A. Abrikosov, and J. Rosen, Magnetically driven anisotropic structural changes in the atomic laminate Mn_2GaC, Phys. Rev. B **93**, 014410 (2016).

[7] R. Meshkian, A. S. Ingason, U. B. Arnalds, F. Magnus, J. Lu, and J. Rosen, A magnetic atomic laminate from thin film synthesis: $(Mo_{0.5}Mn_{0.5})_2GaC$, APL Mater. **3**, 076102 (2015).

[8] A. Petruhins, A. S. Ingason, J. Lu, F. Magnus, S. Olafsson, and J. Rosen, Synthesis and characterization of magnetic $(Cr_{0.5}Mn_{0.5})_2GaC$ thin films, J. Mater. Sci. **50**, 4495 (2015).

[9] R. Salikhov, A. S. Semisalova, A. Petruhins, A. S. Ingason, J. Rosen, U. Wiedwald, and M. Farle, Magnetic anisotropy in the $(Cr_{0.5}Mn_{0.5})_2GaC$ MAX phase, Mater. Res. Lett. **3**, 156 (2015).

[10] A. Mockute, P. O. Å. Persson, F. Magnus, A. S. Ingason, S. Olafsson, L. Hultman, and J. Rosen, Synthesis and characterization of arc deposited magnetic $(Cr,Mn)_2AlC$ MAX phase films, Phys. Status Solidi RRL **8**, 420 (2014).

[11] A. S. Ingason, A. Petruhins, M. Dahlqvist, F. Magnus, A. Mockute, B. Alling, L. Hultman, I. A. Abrikosov, P. O. Å. Persson, and J. Rosen, A nanolaminated magnetic phase: Mn_2GaC, Mater. Res. Lett. **2**, 89 (2014).

[12] X. Z. Yu, Y. Onose, N. Kanazawa, J. H. Park, J. H. Han, Y. Matsui, N. Nagaosa, and Y. Tokura, Real-space observation of a two-dimensional skyrmion crystal, Nature (London) **465**, 901 (2010).

[13] I. P. Novoselova, A. Petruhins, U. Wiedwald, r. S. Ingason, T. Hase, F. Magnus, V. Kapaklis, J. Palisaitis, M. Spasova, M. Farle, J. Rosen, and R. Salikhov, Large uniaxial magnetostriction with sign inversion at the first order phase transition in the nanolaminated Mn_2GaC MAX phase, Sci. Rep. **8**, 2637 (2018).

[14] J. Dey, M. Wójcik, E. Jędryka, R. Kalvig, U. Wiedwald, R. Salikhov, M. Farle, and J. Rosen, Non-collinear magnetic structure of the MAX phase Mn_2GaC epitaxial films inferred from zero-field NMR study (CE-5:L05), Ceram. Int. (2022).

[15] H. J. M. Jönsson, M. Ekholm, I. Leonov, M. Dahlqvist, J. Rosen, and I. A. Abrikosov, Correlation strength, orbital-selective incoherence, and local moments formation in the magnetic MAX-phase Mn_2GaC, Phys. Rev. B **105**, 035125 (2022).

[16] M. Dahlqvist and J. Rosen, Impact of strain, pressure, and electron correlation on magnetism and crystal structure of Mn_2GaC from first-principles, Sci. Rep. **10**, 11384 (2020).

[17] P. Eklund, M. Bugnet, V. Mauchamp, S. Dubois, C. Tromas, J. Jensen, L. Piraux, L. Gence, M. Jaouen, and T. Cabioc'h, Epitaxial growth and electrical transport properties of Cr_2GeC thin films, Phys. Rev. B **84**, 075424 (2011).

[18] A. S. Ingason, A. Petruhins, and J. Rosen, Toward structural optimization of MAX phases as epitaxial thin films, Mater. Res. Lett. **4**, 152 (2016).

[19] K. Momma and F. Izumi, VESTA3 for three-dimensional visualization of crystal, volumetric and morphology data, J. Appl. Crystallogr. **44**, 1272 (2011).

[20] S. Lyaschenko, O. Maximova, D. Shevtsov, S. Varnakov, I. Tarasov, U. Wiedwald, J. Rosen, S. Ovchinnikov, and M. Farle, Optical and magneto-optical properties of epitaxial Mn_2GaC MAX phase thin film, J. Magn. Magn. Mater. **528**, 167803 (2021).

[21] M. A. Vysotin, I. A. Tarasov, A. S. Fedorov, S. N. Varnakov, and S. G. Ovchinnikov, On the possible magnetic properties of ultrathin Mn_2GaC films on Al_2O_3 substrates, JETP Lett. **116**, 323 (2022).

[22] V. Y. Verchenko, A. A. Tsirlin, D. Kasinathan, S. V. Zhurenko, A. A. Gippius, and A. V. Shevelkov, Antiferromagnetic ground state in the $MnGa_4$ intermetallic compound, Phys. Rev. Mater. **2**, 044408 (2018).

[23] A. Petruhins, A. S. Ingason, S. Olafsson, and J. Rosen, Mn_3GaC inverse perovskite thin films by magnetron sputtering from elemental targets, Mater. Res. Express **7**, 106102 (2020).

[24] A. S. Ingason, G. K. Pálsson, M. Dahlqvist, and J. Rosen, Long-range antiferromagnetic order in epitaxial Mn_2GaC thin films from neutron reflectometry, Phys. Rev. B **94**, 024416 (2016).

[25] R. Salikhov, R. Meshkian, D. Weller, B. Zingsem, D. Spoddig, J. Lu, A. S. Ingason, H. Zhang, J. Rosen, U. Wiedwald, and M. Farle, Magnetic properties of nanolaminated $(Mo_{0.5}Mn_{0.5})_2GaC$ MAX phase, J. Appl. Phys. **121**, 163904 (2017).

Paper II

Room temperature ferromagnetism in the nanolaminated MAX phase $(Mn_{1-x}Cr_x)_2GaC$

E.B. Thorsteinsson, M. Dahlqvist, A. Elsukova, A. Petruhins, P. O. Å. Persson, J. Rosen, A. S. Ingason, F. Magnus

APL Materials, 2023, Vol. 11, 121102

https://doi.org/10.1063/5.0176571

Contributions: Synthesized the sample, performed all measurements except TEM, carried out data analysis and co-authored the paper.

Room temperature ferromagnetism in the nanolaminated MAX phase $(Mn_{1-x}Cr_x)_2GaC$

Cite as: APL Mater. 11, 121102 (2023); doi: 10.1063/5.0176571
Submitted: 14 September 2023 • Accepted: 13 November 2023 •
Published Online: 4 December 2023

View Online Export Citation CrossMark

E. B. Thorsteinsson,[1] M. Dahlqvist,[2] A. Elsukova,[2] A. Petruhins,[2] P. O. Å. Persson,[2] J. Rosen,[2] A. S. Ingason,[3] and F. Magnus[1,a)]

AFFILIATIONS

[1] Science Institute, University of Iceland, Dunhaga 3, 107 Reykjavik, Iceland
[2] Department of Physics, Chemistry and Biology, Linköping University, SE-58183 Linköping, Sweden
[3] Grein Research ehf., Dunhaga 5, 107 Reykjavik, Iceland

[a)] Author to whom correspondence should be addressed: fridrikm@hi.is

ABSTRACT

MAX phases are a class of intrinsically nanolaminated materials, which combine features of metals and ceramics, owing to the alternating metallic and covalent bonding between atomic layers. Magnetic MAX phases have been known for a decade, but ferromagnetism at room temperature in this highly anisotropic system has been elusive, limiting their value as magnets in practice. Here, we show that a MAX phase with a strong ferromagnetic response is obtained by substituting Mn with Cr on the M-site in the well-known Mn_2GaC. The ferromagnetic response is observed in $(Mn_{1-x}Cr_x)_2GaC$ with $0.06 < x < 0.29$ up to temperatures well exceeding room temperature (489 K). The strongest magnetization is achieved with $x = 0.12$, reaching a saturation moment of 1.25 μ_B and a remanence of 0.67 μ_B per M-atom at 3 K and maintaining 0.90 and 0.44 μ_B per M-atom, respectively, at 300 K. This is the first experimental report of a significant ferromagnetic response in a MAX phase at room temperature. The results open the door to the use of MAX phases in a broad range of applications, from bulk magnets in power electronics to spintronic devices.

I. INTRODUCTION

Layered materials show a richness of properties, brought about by confinement, broken symmetry at interfaces, and interlayer interactions. Artificial multilayer and superlattice structures have been engineered for decades to exploit these effects, and, more recently, layered van der Waals crystals have appeared on the scene. MAX phases are a family of inherently laminated materials on the nanoscale, composed of a transition metal (M), an A-group element (A), and either carbon or nitrogen (X) with the chemical formula $M_{n+1}AX_n$ $(n = 1, 2, 3)$.[1] The structure is hexagonal, and for $n = 1$, the elements naturally arrange in distinct atomic layers with the order M–A–M–X–M–A–M–X in the *c*-axis direction. The M–A bonds are metallic-like, whereas the M–X bonds are covalent, resulting in a highly anisotropic structure with mechanical properties combining many of the salient features of both metals and ceramics.[2] Furthermore, the A-layers can, in some cases, be selectively etched to produce 2D M–X–M lamellae collectively known as MXenes.[3,4] Theoretical models predict that the laminated structure should result in anisotropic optical, electrical, and magnetic properties, but demonstrating such effects experimentally requires highly oriented single crystal samples and is, therefore, a formidable task. Nonetheless, MAX phases have shown promise in a wide range of contexts, for example as damage tolerant structural materials[5] and for spintronics.[6]

The interest in low-dimensional magnetism[7–9] has fueled the search for new MAX phases exhibiting magnetic order. Only a handful of such phases have been discovered, with magnetic elements in the form of Mn, Cr, or Fe on the M-site[6,10–20] or Mn, Fe, Co, and/or Ni on the A-site.[21–23] In magnetic MAX phases, the anisotropic

layered structure gives rise to competing magnetic interactions within the M–X–M trilayers and across the A layers, resulting in complex magnetic ordering. As an example, the most studied of these phases is Mn_2GaC, which exhibits non-collinear magnetic ordering with a sizable remanent magnetization below 210 K, where it undergoes a magnetic phase transition to antiferromagnetic ordering.[11] The delicate balance between the two magnetic states means that a metamagnetic transition from the antiferromagnetic to the non-collinear state can be induced above 210 K by applying a magnetic field. In addition, it has recently been shown that Mn_2GaC has a magneto-crystalline anisotropy, with the magnetization preferably lying parallel to the Mn–C–Mn planes.[17,24] In another magnetic MAX phase group, $V_2(Sn, A)C$ with (A = Fe, Co, Ni, and Mn), a small remanent magnetization is observed at 2 K, but no remanence is seen at room temperature.[22] Similar results have been obtained for $(Cr_{0.75}Mn_{0.25})_2GeC$ and $(Mo_{0.5}Mn_{0.5})_2GaC$.[10,12] However, no MAX phase has yet been demonstrated to be ferromagnetic with a significant magnetic moment at room temperature. This has prevented their use in practical applications as bulk magnets or in spintronic devices.

Here, we show that a MAX phase in a previously unexplored composition range, $(Mn_{1-x}Cr_x)_2GaC$ with $x < 0.3$, is strongly ferromagnetic up to temperatures far exceeding room temperature. We use first-principles calculations to predict over which range of compositions, ferromagnetism is expected to be the most stable magnetic configuration. We then synthesize these compositions as epitaxial thin films and demonstrate a strong ferromagnetic response. The result is the first MAX phase, which can be used as a magnet in room temperature applications, with great scope for further tuning of its magnetic properties.

II. RESULTS

A. Stability predictions

First-principles calculations based on density functional theory were carried out to determine the stability of $(Mn_{1-x}Cr_x)_2GaC$ with $0 \le x \le 1$. Different magnetic configurations were taken into account in the stability calculations to determine the most likely magnetic ordering. The configurations considered were paramagnetic (PM), ferromagnetic (FM), and several antiferromagnetic (AFM) arrangements, i.e., multilayered AFM ordering of α consecutive M layers (where $\alpha = 2, 4$) with the same spin direction before changing sign upon crossing an A layer ($AFM[0001]_2^A$ and $AFM[0001]_4^A$) and antiparallel spins within one M layer (in-AFM1). These magnetic configurations are schematically shown in Fig. 1. Since we are interested in the stability upon substituting Mn by Cr in $(Mn_{1-x}Cr_x)_2GaC$, the identified set of most competing phases for $0 < x < 1$ is a linear combination of Mn_2GaC and Cr_2GaC. The corresponding isostructural formation enthalpies ΔH_{iso} are calculated with Eq. (1) (see Sec. V). Figure 1 shows ΔH_{iso} (at 0 K) and isostructural Gibbs free energy of formation, ΔG_{iso} (estimated at 1000 K with the addition of configuration entropy), for the entire composition range. Since the focus is on the quaternary system with a disorder of Mn and Cr on the M site and the synthesis of MAX phases is performed at elevated temperature, ΔG_{iso} is the more relevant parameter in terms of stability.

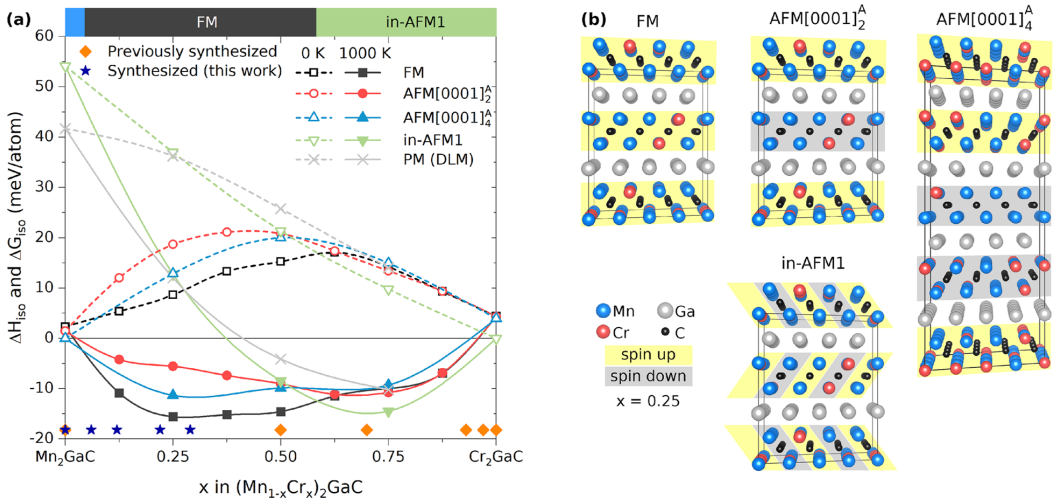

FIG. 1. First-principles spin-dependent stability calculations. (a) Calculated isostructural formation enthalpy at 0 K, $\Delta H_{iso}^{disorder}$ (open symbols with dashed lines), and Gibbs free energy of formation estimated at 1000 K, $\Delta G_{iso}^{disorder}$ (solid symbols with solid lines), as functions of x for $(Mn_{1-x}Cr_x)_2GaC$. Five different spin configurations are considered, and the lowest energy configuration is indicated at the top of the graph. Experimentally synthesized MAX phase compositions are marked by orange diamonds for previous studies and blue stars for this work. (b) Schematics of the SQS supercells used for the calculations, for the composition $x = 0.25$, illustrating the layered MAX phase structure and the magnetic configurations.

$(Mn_{1-x}Cr_x)_2GaC$ is found to be stable for all x, but with different spin configurations giving the lowest energy for different values of x. The in-AFM1 configuration is of lowest energy in the Cr-rich region, i.e., for $x > 0.6$. For Mn-rich conditions, FM is favored but with AFM$[0001]_4^A$ close in energy. For pure Mn_2GaC, AFM$[0001]_4^A$ is the lowest energy spin configuration. Both Mn_2GaC and Cr_2GaC have been synthesized before and found to be thermodynamically stable.[16,25–27] Mn_2GaC has experimentally been shown to be in an AFM$[0001]_4^A$-like magnetic configuration at room temperature,[11,17] whereas Cr_2GaC is thought to be paramagnetic.[28] Some compositions of the $(Mn_{1-x}Cr_x)_2GaC$ solid solution have also been previously synthesized both as thin films[11,13,16,27] ($x = 0.5$) and in bulk ($x \geq 0.7$),[15,25,29,30] as shown by the orange diamonds in Fig. 1(a). These compositions have been found to be weakly ferro- or ferrimagnetic at well below room temperature. However, the composition range of $0 < x < 0.5$, where our calculations show that the FM configuration is lowest in energy, has hitherto not been studied.

B. Film structure

$(Mn_{1-x}Cr_x)_2GaC$ films were synthesized by DC magnetron sputtering as described in Sec. V and found to have x in the range 0.00–0.29 by energy dispersive x-ray spectroscopy (EDX) measurements. Figure 2(a) shows the XRD overview scans of the sample series. The characteristic MAX phase (000l) basal plane peaks are seen in all the samples, and there are no detectable competing phases present. In addition to the (000l) peaks, we observe peaks corresponding to the $(10\bar{1}3)$ and $(20\bar{2}6)$ planes, showing that the films have two distinct growth orientations. The $(10\bar{1}3)$ plane has a tilt of 59° with respect to the (0006) plane, and this is, therefore, referred to as the tilted phase. From the known difference in the relative intensity of the $(10\bar{1}3)$ and (0006) peaks in Mn_2GaC (100% and 18%, respectively), we estimate that the films have between 49% and 71% of $(10\bar{1}3)$ oriented grains parallel to the substrate plane (see the supplementary material for details). This tilted growth has previously been seen in pure Mn_2GaC grown on MgO(111) substrates,[17] as well as in other epitaxial MAX phase films.[31]

The inset of Fig. 2(a) highlights the $(10\bar{1}3)$ and (0006) peaks, showing the progression as the Cr content is increased. The peaks broaden with increasing Cr content, indicating a reduction in crystallite size. From these XRD scans, the a and c lattice parameters were extracted from the $(10\bar{1}3)$ and (0006) peak positions (see the supplementary material), which allows us to quantify the changes in unit cell volume upon substituting Mn by Cr.

Figure 2(b) shows a pole figure of the $(10\bar{1}3)$ peak in the $x = 0.12$ film. This figure is representative of all the films in the sample series, as all of them show the same features. There is a large peak in the center from the grains with the $(10\bar{1}3)$ planes parallel to the film plane and a set of sixfold symmetric discrete peaks at $\chi = 59°$. This shows the epitaxial nature of the film, albeit with mixed crystal orientations. The additional satellite peaks are due to twinning and have previously been seen in the pure Mn_2GaC phase.[17] This behavior is observed when two growth orientations coexist, with both (000l) and $(10\bar{1}3)$ oriented grains in the plane of the film.

To investigate the local film structure and elemental composition, the film with $x = 0.22$ was characterized using transmission electron microscopy (TEM). Figures 3(a)–3(e) show a high-angular annular dark field scanning TEM (HAADF-STEM) image with the corresponding elemental maps obtained by energy-dispersive x-ray spectroscopy (EDX). The maps show a uniform distribution of Mn and Cr and no phase segregation. This, together with the shift in the x-ray diffraction peaks, strongly indicates that the Cr is substituting the Mn uniformly throughout the film and is not forming a secondary phase. High-resolution HAADF-STEM images with increasing magnification are shown in Figs. 3(f)–3(h). The lowest magnification shows the presence of multiple grains, and the two distinct $(10\bar{1}3)$ and (0006) orientations of the grains are clearly

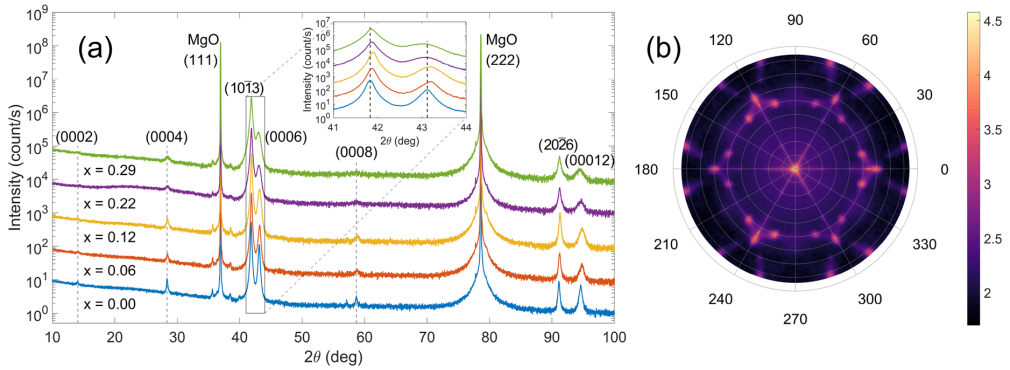

FIG. 2. Phase analysis and crystal structure. (a) XRD overview scans of $(Mn_{1-x}Cr_x)_2GaC$ with x in the range 0.00–0.29. All samples show distinctive MAX phase peaks. The inset is an enlargement of the region containing the main film peaks of $(10\bar{1}3)$ and (0006). The peaks are broadened and slightly shifted with increasing Cr content. In both figures, the scans are each shifted vertically by a factor of ten successively, with the $x = 0.00$ scan as measured. (b) Pole figure of the $(Mn_{1-x}Cr_x)_2GaC$ sample with x = 0.12, for the $(10\bar{1}3)$ peak at $2\theta = 41.84°$. The figure shows the epitaxial relationship between the film and the substrate and is representative of the sample series. The intensity is on a logarithmic scale.

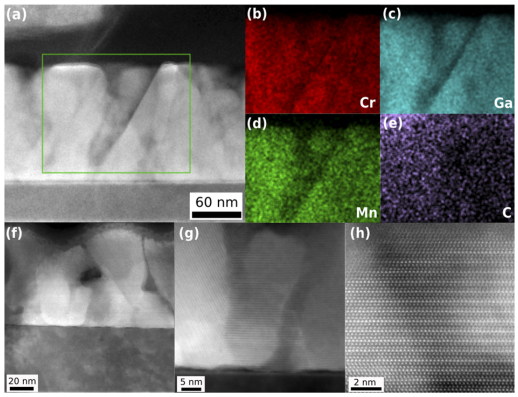

FIG. 3. Local structure and chemical composition. (a) STEM-HAADF image of a $(Mn_{1-x}Cr_x)_2GaC$ film with $x = 0.22$ with the corresponding Cr–$K\alpha$ (b), Ga–$K\alpha$ (c), Mn–$K\beta$ (d), and C–$K\alpha$ (e) elemental EDX maps. No segregation of the elements is observed. (f)–(h) High resolution STEM-HAADF images showing the MAX phase structure with mixed orientations.

visible at intermediate magnification. At high magnification, the laminated MAX phase structure within the crystal grains is apparent.

C. Magnetic properties

Figure 4(a) shows the magnetic hysteresis measurements performed at 300 K, with the MgO background subtracted (for details of this procedure, see Sec. V and Ref. 17). The diamagnetic and paramagnetic signals have also been removed. All the Cr containing films exhibit a strong ferromagnetic (FM) response at room temperature, as evidenced by the clear remanent magnetization, a coercivity, and S-shaped hysteresis loops. This behavior is qualitatively the same in the temperature range studied (see below). This is in stark contrast to the pure Mn_2GaC film, which undergoes a transition from a non-collinear magnetic state to an antiferromagnetic state at around 210 K. In the AFM state, it exhibits a metamagnetic transition that moves to higher fields as the temperature is increased. This can be seen in the 300 K data in Fig. 4(a) at 2.5 T (blue curve).

The remanent magnetization of the films, M_r, is shown in Fig. 4(b) as a function of temperature. The samples with $x = 0.00$ and $x = 0.06$ have an unusual temperature dependence, with the non-collinear to AFM transition being evident in the pure Mn_2GaC sample starting at 210 K. For samples with $0.12 \leq x \leq 0.29$, a typical FM temperature dependence is seen, with a gradual decrease in the remanent magnetization with increasing temperature. Interestingly, the remanent magnetization peaks for $x = 0.12$ and then decreases as the Cr content is increased further. This is also the case for the saturation magnetization $M_{5\,T}$ (at 5 T), which can be seen in the supplementary material. There is a sharp increase in remanence between $x = 0.06$ and 0.12 before it slowly decreases as more Cr is added. The magnetization of $(Mn_{1-x}Cr_x)_2GaC$ with $x = 0.12$ is the strongest of the series, reaching a saturation magnetization of 1.25 μ_B/M-atom at 3 K and maintaining 0.90 μ_B/M-atom at 300 K.

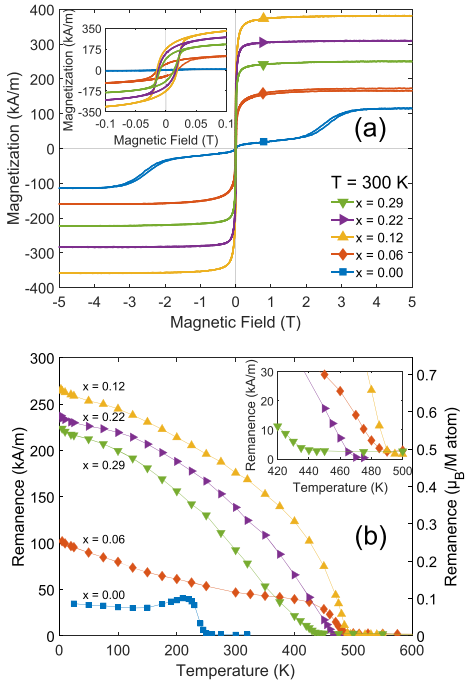

FIG. 4. Magnetic properties. (a) Magnetic hysteresis loops for all the $(Mn_{1-x}Cr_x)_2GaC$ samples at 300 K. The sample with $x = 0.00$ has the distinctive metamagnetic transition seen in the pure Mn_2GaC phase, but with increasing Cr content, a typical ferromagnetic response is obtained. The inset shows a zoomed-in view of the hysteretic part of the loop, demonstrating a large remanent magnetization for all Cr containing samples. All the measurements have had the MgO background subtracted. (b) Remanent magnetization as a function of temperature for the sample series. The inset shows a zoomed-in view of the critical temperature region. Samples with $x = 0.12$ and above show a typical ferromagnetic behavior, and the magnetization is largest for $x = 0.12$.

Similarly, it has the largest remanent magnetization of 0.67 μ_B/M-atom at 3 K and 0.44 μ_B/M-atom at 300 K. Here, M in μ_B/M-atom refers to the sum of Mn and Cr located at the M sites of the MAX phase (M_2AX).

Figure 5 shows the critical temperature T_c, the magnetization at 5 T and remanence together with the measured change in lattice parameters and unit cell volume, all as a function of Cr content. The critical temperature is defined as the temperature where the remanent magnetization is reduced to zero (also known as the Curie temperature in a ferromagnetic material) and can be considered a measure of the (mean) magnetic interaction strength J. The critical temperature peaks for $x = 0.12$ at 489 K (216 °C), which is also the composition having the largest magnetization. The resistivity follows a similar but opposite trend, as shown in the supplementary material, with a minimum of ~360 $\mu\Omega$ cm in the range $0.06 \leq x \leq 0.12$. There is a clear correlation between T_c, the magnetization,

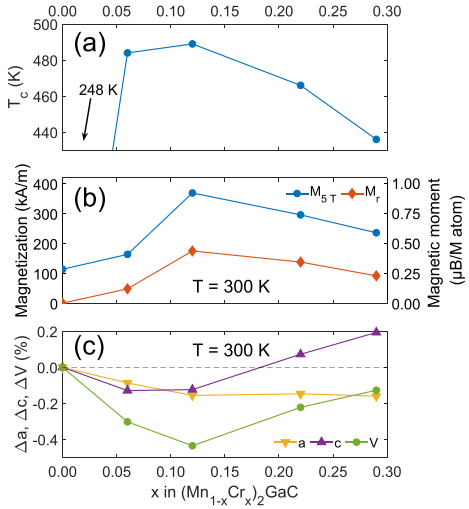

FIG. 5. Linking structure and magnetic interaction strength. (a) The critical temperature T_c (or exchange constant J) as a function of Cr content. (b) Magnetization at 5 T and remanence as a function of Cr content at 300 K. (c) The change in the lattice parameters a and c as well as the unit cell volume V as a function of Cr content, also at 300 K. The peak in T_c and magnetization coincides with the smallest unit cell volume.

and the change in unit cell volume. As x is increased, the volume reaches a minimum at $x = 0.12$ due to a contraction in both a and c. With further increasing x, the c lattice parameter expands. The resulting minimum in volume is accompanied by a maximum in T_c and magnetization.

III. DISCUSSION

The spin-dependent stability calculations are in remarkably good agreement with the experimental results. The calculations predict phase stability over the entire range of $0 \le x \le 1$, which is confirmed by the thin film synthesis (presented here and elsewhere). Furthermore, theory suggests that ferromagnetic ordering of the M-site moments is the most stable configuration in the range $0.06 < x \le 0.50$. Our magnetic characterization shows that films with $0.06 < x \le 0.29$ are, indeed, strongly ferromagnetic. However, it should be noted that we cannot rule out that the ferromagnetic response observed experimentally is non-collinear in nature. At $x = 0.06$, there are clear signs of competing interactions, which result in a magnetic response that is neither clearly ferromagnetic nor antiferromagnetic. This is consistent with the calculations that show that the FM and AFM$[0001]_4^A$ configurations are close to degenerate for this composition. For Cr content below 6 at. % or above 50 at. %, the AFM configurations are the lowest in energy. However, the closeness of the different configurations can explain why metamagnetic transitions and non-collinear magnetic order and/or very low critical temperatures are observed in these cases.

It has previously been shown for Mn_2GaC that the magnetization is sensitive to a change in the lattice parameters[6,24] and that the magnetic transition from AFM- to FM-like ordering coincides with a contraction in the c lattice parameter. The calculations show that in the $(Mn_{1-x}Cr_x)_2GaC$ system, the FM configuration has the smallest c lattice parameter (see the supplementary material). The experimental data are in partial agreement with these results although we observe a maximum in the critical temperature and magnetization where there is a minimum in the film volume rather than in the c lattice parameter. In the case of epitaxial thin films, the a lattice parameter is constrained due to the bonding with the substrate, as shown in Fig. 5. This results in anisotropic strain, which counteracts the contraction of the c lattice parameter, and this may explain the discrepancy between theory and experiments. However, the general trends observed in the lattice parameters are qualitatively consistent with theory. This implies that strain engineering may be a feasible way to control the strength of the FM interaction, thus allowing us to tune the critical temperature and magnetization, as previously suggested by Dahlqvist and Rosen.[24] The large number of isostructural MAX phases with similar lattice parameters, which could be combined in epitaxial heterostructures, makes this a highly appealing prospect.

IV. CONCLUSIONS

Phase pure thin films of $(Mn_{1-x}Cr_x)_2GaC$ were synthesized in the range from $x = 0.00$ to $x = 0.29$ on MgO(111) substrates, and their structural and magnetic properties were characterized. Partial substitution of Mn with Cr on the M-site results in a MAX phase, which is strongly ferromagnetic at room temperature. Its saturation magnetization of 1.25 μ_B/M-atom at 3 K is almost 35 times larger than the previously reported magnetization of the $(V,Mn)_3GaC_2$ MAX phase (0.036 μ_B/M-atom at 100 K and 0.026 μ_B/M-atom at 300 K).[32] To put this into context, the magnetic moment of Fe and Ni at 0 K is 2.22 and 0.61 μ_B/atom, respectively, giving a magnetization of 1745 kA/m for Fe and 521 kA/m for Ni at 0 K. The magnetization of $(Mn_{0.88}Cr_{0.12})_2GaC$ is 516 kA/m at 3 K, making it comparable to Ni at low temperatures, but the magnetization falls off faster as the temperature is increased due to a lower critical temperature of 489 K vs 627 K for Ni. The ferromagnetic response is associated with a contraction in the unit cell volume, suggesting that the magnetization might be even further enhanced with strain engineering using different substrates and/or MAX-phase heterostructures. In addition, $(Mn_{0.88}Cr_{0.12})_2GaC$ is significantly lighter than Fe and Ni, which means that its mass magnetization values compare even more favorably with those of typical magnetic metal alloys, such as transformer steel. Furthermore, the inherently laminated structure results in high resistivity values of ~360 $\mu\Omega$ cm, which is, for example, important for reducing eddy currents in transformer core applications. These magnetic properties, combined with the mechanical advantages of the MAX phase structure, make this material a serious contender for bulk magnets in power electronics.

V. METHODS

A. Thin film synthesis

The $(Mn_{1-x}Cr_x)_2GaC$ films were grown by direct current magnetron sputtering (dcMS) on 1 × 1 cm^2 MgO(111) substrates from a 7.5 cm diameter 99.9% pure Mn target, a 7.5 cm 99.99% C target, a 5.0 cm 99.95% Cr target, and a liquid Ga target made from 99.9999%

Ga pellets in a specially made 5.0 cm crucible. During sputtering, the Ga target was maintained in liquid form. The working gas was 99.999% purity argon at a flow rate of 20 sccm, and a throttle valve was used to adjust the growth pressure to 0.40 Pa. The vacuum chamber used has a base pressure of $<5 \times 10^{-7}$ Pa; however, at the growth temperature of 550 °C, the base pressure rose to 2×10^{-6} Pa after preheating the substrate for 60 min. For the duration of the growth, the sample holder was rotated by ±360° at a rate of 12 revolutions per minute. These growth conditions are the same as in a previous study of Mn_2GaC films;[17] except here, Mn is partially substituted by Cr. This includes the growth temperature, pressure, and a slight excess of Ga, which diffuses to the surface of the films.

The Mn, Cr, and C targets were rate-calibrated to get the composition in the correct range prior to the growth of a series of $(Mn_{1-x}Cr_x)_2GaC$ samples. The chemical composition was then determined by energy dispersive x-ray spectroscopy (EDX) in a Zeiss Supra 25 electron microscope as $x = 0.00$, 0.06, 0.12, 0.22, and 0.29. It should be noted that the C and Ga content cannot be measured with any certainty because C content is not reliably determined by EDX and the samples contain an excess of Ga on the surface. The thickness of the films was found to be 140 ± 4 nm from x-ray reflectivity (XRR) measurements.

B. Structural characterization

The structural properties of the films were investigated by x-ray diffraction (XRD) and x-ray reflectivity (XRR) using a Panalytical Empyrean diffractometer in line focus mode. For diffraction, the incident side had a two-bounce hybrid monochromator with 1/8° divergence slit; on the diffracted side was a PIXcel^{3D} detector operating in 1D mode.

Scanning transmission electron microscopy (STEM) imaging and energy dispersive x-ray spectroscopy (EDX) were performed in the Linköping double-corrected, monochromated, high-brightness, FEI Titan^3, equipped with a Super-X EDX detector and operated at 300 kV. The specimen for TEM examination was prepared by mechanical grinding followed by Ar^+-ion milling using a Gatan Precision Ion Polishing System.

C. Magnetic and electrical characterization

The magnetic properties were measured using vibrating sample magnetometry (VSM) in the temperature range from 3 to 300 K in a 5 T cryogen free magnet system from Cryogenic and in the range from 300 to 750 K in a Lake Shore 8600 system with a single stage variable temperature option and a 2 T electromagnet. The magnetization was calculated by dividing the measured moment by the film volume, and to convert to units of Bohr magnetons, we used the measured unit cell volume, which contains four M atoms. The temperature dependence of the magnetization and the remanent magnetization were determined by performing full hysteresis loops at each temperature. The MgO background signal was removed by measuring full hysteresis loops on a bare substrate for temperatures ≤300 K. To join together measurements from both systems, a linear fit of data above ±4.5 T for the cryogenic system and ±1.5 T for the Lake Shore system was performed to remove dia- and paramagnetic effects. This mainly affects x = 0.00, which might not be fully saturated at 5 T, as well as x = 0.06, which has some paramagnetic behavior.

The resistivity of the films was measured using a Jandel four-probe system with equally spaced probes arranged in a straight line geometry. Full current–voltage curves were recorded to ensure that good ohmic contacts were obtained and the resistivity calculated from the sheet resistance using the film thickness.

D. First-principles modeling

All first-principles calculations were performed by means of density functional theory (DFT) and the projector augmented wave method,[33,34] as implemented within the Vienna *Ab initio* Simulation Package (VASP) version 5.4.1.[35–37] We used the spin polarized generalized gradient approximation (GGA) as parameterized by Perdew–Burke–Ernzerhof (PBE) for treating the electron exchange and correlation effects.[38] We considered selected spin configurations based on results for Cr_2GaC and Mn_2GaC,[11,39] namely ferromagnetic (FM) and several antiferromagnetic (AFM) configurations; multilayered AFM ordering of α consecutive M layers (where $\alpha = 2, 4$) with the same spin direction before changing sign upon crossing an A layer (AFM$[0001]_2^A$ and AFM$[0001]_4^A$) and antiparallel spins within one M layer (in-AFM1). In addition, paramagnetism (PM) has been modeled using the disorder local moment (DLM)[40] approach where the spin-correlation functions are equal to zero for at least the first 10M-coordination shells. For Mn_2GaC, this corresponds to disordered magnetic moments in $(Mn\uparrow_{0.5}Mn\downarrow_{0.5})_2GaC$ being simulated by means of the special quasi-random structure (SQS) method[41] using a supercell with 64 Mn, 32 Ga, and 32 C atoms, i.e., $4 \times 4 \times 1$ or 16 M_2AX unit cells. For $(Mn_{1-x}Cr_x)_2GaC$, DLM was modeled using $4 \times 4 \times 2$ unit cells with initial disordered Mn moments. The plane wave energy cutoff was set at 400 eV, with k-point grids with a spacing of 0.05 $Å^{-1}$ according to the Monkhorst–Pack method.[42] The total energy is minimized through the relaxation of the unit-cell shape and volume and internal atomic positions.

To model chemical disorder of Mn and Cr on the M sublattice for $(Cr_{1-x}Mn_x)_2GaC$, we used the SQS method[41] with supercell sizes consisting of $2 \times 2 \times 2$, $4 \times 2 \times 1$, $4 \times 3 \times 1$, $4 \times 4 \times 1$, and $4 \times 4 \times 2$ unit cells, i.e., 72–256 atoms per supercell. Convergence tests show that these supercells give a qualitatively accurate representation and a quantitative convergence in terms of calculated formation enthalpies and lattice parameters.

The thermodynamic stability of quaternary MAX phases is investigated at 0 K with respect to decomposition into Mn_2GaC and Cr_2GaC. This is motivated since both are experimentally known and have been predicted to be stable.[16,27] The stability of the quaternary MAX phase is quantified in terms of isostructural formation enthalpy ΔH_{iso} by comparing its energy to the energy of Mn_2GaC and Cr_2GaC, according to

$$\Delta H_{iso}^{\text{disorder}} = E((Mn_{1-x}Cr_x)_2GaC) - (1-x)E(Mn_2GaC) - (x)E(Cr_2GaC). \quad (1)$$

A phase is concluded stable when $\Delta H_{iso}^{\text{disorder}} < 0$. Here, $E((Mn_{1-x}Cr_x)_2GaC)$ represents the chemically disordered MAX phase structure of lowest energy. When $T \neq 0$ K, the contribution from configurational entropy due to disorder of Mn and Cr on the M sublattice will decrease the isostructural Gibbs free energy $\Delta G_{iso}^{\text{disorder}}$ as approximated by

$$\Delta G_{iso}^{\text{disorder}}[T] = \Delta H_{iso}^{\text{disorder}} - T\Delta S, \quad (2)$$

where the entropic contribution ΔS, assuming an ideal solution of Mn and Cr on the M-sites, is given by

$$\Delta S = -2k_B[x \ln(x) + (1-x)\ln(1-x)], \quad (3)$$

where k_B is the Boltzmann constant and x is the concentration of Cr on the M-sublattice.

SUPPLEMENTARY MATERIAL

The supplementary material contains additional results from first-principles calculations, including lattice parameters (Fig. S1, Table S1) and magnetic moments (Fig. S2). It also includes measured lattice parameters and critical temperatures for the film series (Table S2), a wider area TEM elemental EDX map examining the chemical uniformity over larger length scales (Fig. S3), further magnetic measurements showing the saturation magnetization (Fig. S4) and coercive field (Fig. S5) as a function of temperature, and the measured resistivity of the films (Fig. S6).

ACKNOWLEDGEMENTS

This work was funded by the University of Iceland Research Fund and the Icelandic Research Fund (Grant Nos. 174271 and 217843). The authors acknowledge ARTEMI, the Swedish National Infrastructure in Advanced Electron Microscopy, supported by the Swedish Research Council and the Swedish Foundation for Strategic Research (Grant Nos. 2021-00171 and RIF21-0026). The calculations were carried out using supercomputer resources provided by the Swedish National Infrastructure for Computing (SNIC) at the National Supercomputer Center (NSC), partially funded by the Swedish Research Council through Grant Agreement No. 2018-05973. J.R. acknowledges the support from the Swedish Research Council (Grant No. 2019-04233) and the Göran Gustafsson Foundation for Research in Natural Sciences and Medicine.

AUTHOR DECLARATIONS

Conflict of Interest

The authors have no conflicts to disclose.

Author Contributions

E. B. Thorsteinsson: Conceptualization (equal); Formal analysis (lead); Investigation (lead); Software (equal); Visualization (equal); Writing – original draft (equal); Writing – review & editing (lead). **M. Dahlqvist**: Conceptualization (equal); Formal analysis (lead); Methodology (lead); Software (equal); Visualization (equal); Writing – review & editing (equal). **A. Elsukova**: Formal analysis (equal); Investigation (equal); Visualization (equal). **A. Petruhins**: Investigation (supporting). **P. O. Å. Persson**: Funding acquisition (equal); Writing – review & editing (equal). **J. Rosen**: Conceptualization (equal); Funding acquisition (equal); Writing – review & editing (equal). **A. S. Ingason**: Conceptualization (equal); Writing – review & editing (equal). **F. Magnus**: Conceptualization (equal); Funding acquisition (equal); Project administration (lead); Supervision (lead); Writing – original draft (equal); Writing – review & editing (lead).

DATA AVAILABILITY

The data that support the findings of this study are available from the corresponding author upon reasonable request.

REFERENCES

[1] M. W. Barsoum, Prog. Solid State Chem. **28**, 201 (2000).
[2] M. Sokol, V. Natu, S. Kota, and M. W. Barsoum, Trends Chem. **1**, 210 (2019).
[3] M. Naguib, M. Kurtoglu, V. Presser, J. Lu, J. Niu, M. Heon, L. Hultman, Y. Gogotsi, and M. W. Barsoum, Adv. Mater. **23**, 4248 (2011).
[4] A. VahidMohammadi, J. Rosen, and Y. Gogotsi, Science **372**, eabf1581 (2021).
[5] M. Barsoum, T. Zhen, S. Kalidindi, M. Radovic, and A. Murugaiah, Nat. Mater. **2**, 107 (2003).
[6] I. P. Novoselova, A. Petruhins, U. Wiedwald, A. S. Ingason, T. Hase, F. Magnus, V. Kapaklis, J. Palisaitis, M. Spasova, M. Farle, J. Rosen, and R. Salikhov, Sci. Rep. **8**, 2637 (2018).
[7] N. Samarth, Nature **546**, 216 (2017).
[8] B. Huang, G. Clark, E. Navarro-Moratalla, D. R. Klein, R. Cheng, K. L. Seyler, D. Zhong, E. Schmidgall, M. A. McGuire, D. H. Cobden, W. Yao, D. Xiao, P. Jarillo-Herrero, and X. Xu, Nature **546**, 270 (2017).
[9] C. Gong, L. Li, Z. Li, H. Ji, A. Stern, Y. Xia, T. Cao, W. Bao, C. Wang, Y. Wang, Z. Q. Qiu, R. J. Cava, S. G. Louie, J. Xia, and X. Zhang, Nature **546**, 265 (2017).
[10] A. S. Ingason, A. Mockute, M. Dahlqvist, F. Magnus, S. Olafsson, U. B. Arnalds, B. Alling, I. A. Abrikosov, B. Hjorvarsson, P. O. A. Persson, and J. Rosen, Phys. Rev. Lett. **110**, 195502 (2013).
[11] M. Dahlqvist, A. S. Ingason, B. Alling, F. Magnus, A. Thore, A. Petruhins, A. Mockute, U. B. Arnalds, M. Sahlberg, B. Hjorvarsson, I. A. Abrikosov, and J. Rosen, Phys. Rev. B **93**, 014410 (2016).
[12] R. Meshkian, A. S. Ingason, U. B. Arnalds, F. Magnus, J. Lu, and J. Rosen, APL Mater. **3**, 076102 (2015).
[13] A. Petruhins, A. S. Ingason, J. Lu, F. Magnus, S. Olafsson, and J. Rosen, J. Mater. Sci. **50**, 4495 (2015).
[14] R. Salikhov, A. S. Semisalova, A. Petruhins, A. S. Ingason, J. Rosen, U. Wiedwald, and M. Farle, Mater. Res. Lett. **3**, 156 (2015).
[15] A. Mockute, P. O. A. Persson, F. Magnus, A. S. Ingason, S. Olafsson, L. Hultman, and J. Rosen, Phys. Status Solidi RRL **8**, 420 (2014).
[16] A. S. Ingason, A. Petruhins, M. Dahlqvist, F. Magnus, A. Mockute, B. Alling, L. Hultman, I. A. Abrikosov, P. O. A. Persson, and J. Rosen, Mater. Res. Lett. **2**, 89 (2014).
[17] E. B. Thorsteinsson, A. S. Ingason, and F. Magnus, Phys. Rev. Mater. **7**, 034409 (2023).
[18] C. M. Hamm, J. D. Bocarsly, G. Seward, U. I. Kramm, and C. S. Birkel, J. Mater. Chem. C **5**, 5700 (2017).
[19] H. Pazniak, M. Stevens, M. Dahlqvist, B. Zingsem, L. Kibkalo, M. Felek, S. Varnakov, M. Farle, J. Rosen, and U. Wiedwald, ACS Appl. Nano Mater. **4**, 13761 (2021).
[20] S. Lin, Y. Huang, L. Zu, X. Kan, J. Lin, W. Song, P. Tong, X. Zhu, and Y. Sun, J. Alloys Compd. **680**, 452 (2016).
[21] Y. Li, S. Zhu, E. Wu, H. Ding, J. Lu, X. Mu, L. Chen, Y. Zhang, J. Palisaitis, K. Chen, M. Li, P. Yan, P. O. A. Persson, L. Hultman, P. Eklund, S. Du, Y. Kuang, Z. Chai, and Q. Huang, J. Phys. Chem. Lett. **14**, 481 (2023).
[22] Y. Li, J. Lu, M. Li, K. Chang, X. Zha, Y. Zhang, K. Chen, P. O. A. Persson, L. Hultman, P. Eklund, S. Du, J. S. Francisco, Z. Chai, Z. Huang, and Q. Huang, Proc. Natl. Acad. Sci. U. S. A. **117**, 820 (2020).
[23] L. Chen, Y. Li, B. Zhao, S. Liu, H. Zhang, K. Chen, M. Li, S. Du, F. Xiu, R. Che, Z. Chai, and Q. Huang, Adv. Sci. **10**, 2206877 (2023).

[24]M. Dahlqvist and J. Rosen, Sci. Rep. **10**, 11384 (2020).
[25]J. Etzkorn, M. Ade, D. Kotzott, M. Kleczek, and H. Hillebrecht, J. Solid State Chem. **182**, 995 (2009).
[26]B. Manoun, S. Kulkarni, N. Pathak, S. K. Saxena, S. Amini, and M. W. Barsoum, J. Alloys Compd. **505**, 328 (2010).
[27]A. Petruhins, A. S. Ingason, M. Dahlqvist, A. Mockute, M. Junaid, J. Birch, J. Lu, L. Hultman, P. O. A. Persson, and J. Rosen, Phys. Status Solidi RRL **7**, 971 (2013).
[28]J. P. Siebert, L. Bischoff, M. Lepple, A. Zintler, L. Molina-Luna, U. Wiedwald, and C. S. Birkel, J. Mater. Chem. C **7**, 6034 (2019).
[29]S. Lin, P. Tong, B. S. Wang, Y. N. Huang, W. J. Lu, D. F. Shao, B. C. Zhao, W. H. Song, and Y. P. Sun, "Magnetic and electrical/thermal transport properties of Mn–doped $M_{n+1}AX_n$ phase compound $Cr_{2-x}Mn_xGaC$ ($0 \le x \ge 1$)," J. Appl. Phys. **113**, 053502 (2013).
[30]A. Maniv, A. P. Reyes, S. K. Ramakrishna, D. Graf, A. Huq, D. Potashnikov, O. Rivin, A. Pesach, Q. Tao, J. Rosen, I. Felner, and E. N. Caspi, J. Phys.: Condens. Matter **33**, 025803 (2020).
[31] P. Eklund, M. Bugnet, V. Mauchamp, S. Dubois, C. Tromas, J. Jensen, L. Piraux, L. Gence, M. Jaouen, and T. Cabioc'h, Phys. Rev. B **84**, 075424 (2011).
[32]Q. Tao, R. Salikhov, A. Mockute, J. Lu, M. Farle, U. Wiedwald, and J. Rosen, APL Mater. **4**, 086109 (2016).
[33]P. E. Blochl, Phys. Rev. B **50**, 17953 (1994).
[34]G. Kresse and D. Joubert, Phys. Rev. B **59**, 1758 (1999).
[35]G. Kresse and J. Hafner, Phys. Rev. B **47**, 558 (1993).
[36]G. Kresse and J. Furthmüller, Comput. Mater. Sci. **6**, 15 (1996).
[37]G. Kresse and J. Furthmüller, Phys. Rev. B **54**, 11169 (1996).
[38]J. P. Perdew, K. Burke, and M. Ernzerhof, Phys. Rev. Lett. **77**, 3865 (1996).
[39]M. Dahlqvist, B. Alling, and J. Rosen, J. Phys.: Condens. Matter **27**, 095601 (2015).
[40]B. L. Gyorffy, A. J. Pindor, J. Staunton, G. M. Stocks, and H. Winter, J. Phys. F: Met. Phys. **15**, 1337 (1985).
[41] A. Zunger, S.-H. Wei, L. G. Ferreira, and J. E. Bernard, Phys. Rev. Lett. **65**, 353 (1990).
[42]H. J. Monkhorst and J. D. Pack, Phys. Rev. B **13**, 5188 (1976).

SUPPLEMENTARY MATERIAL

A. Additional results from theory

Lattice parameters were determined from the first-principles calculations as a function of composition for all the considered magnetic configurations. Figure S1 shows the results for the lattice parameters a and c. For most spin configurations, a decreases and c increases with decreasing amount of Mn. Similar trends are found in the values reported in this work and in previously reported experimentally values.[1–8] However, experiments consistently yield slightly higher values for both lattice parameters than theory. Note that the experimental results are retrieved from both thin film and bulk samples.

Calculated local and averaged magnetic moments along with net moment per M atom is shown in Fig S2. In all cases the Mn moments are quite robust, compared to Cr, with similar

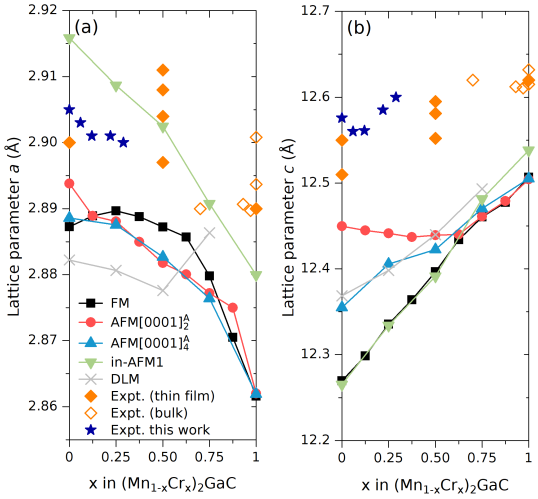

Figure S1. **Lattice parameters from first-principles calculations.** Calculated lattice parameters (a) a and (b) c for $(Mn_{1-x}Cr_x)_2GaC$ for selected spin configurations. Measured values reported herein are represented by blue stars and experimentally reported values for MAX phases in thin film[1,2,4,5] and bulk[3,6–8] form are marked by filled and open orange diamonds, respectively.

size at all x. Note that for AFM$[0001]_2^A$ and AFM$[0001]_4^A$, Cr moments easily flip sign and hence no average value is given. For in-AFM1, both Cr and Mn atoms are stable and with rather small spread. For the FM configuration, all moments keep their sign and show a rather small spread. The net moment per M atom for $x = 0.12$ is approximately 1.71 μ_B which is somewhat higher than the experimentally determined 5 T moment of 1.25 μ_B/M-atom for this composition.

B. Further structural analysis

Lattice parameters were determined from the XRD measurements for all compositions synthesized as thin films. The results can be seen in Tab. S2 and the relative change in lattice parameters can be seen in Fig. 5 in the main text. For the c lattice parameter it can be seen that as the Cr content is increased it initially contracts by -0.13% at x = 0.06 before increasing to 0.19% at x = 0.29 compared to pure Mn_2GaC. This is a considerable range of 0.32%, which is comparable to the total change in the c lattice parameter of Mn_2GaC from 100 K to 300 K[9]. Concomitantly, the a lattice parameter contracts slightly up to $x = 0.12$ and then remains stable up to $x = 0.29$. This results in the unit cell volume reaching a

Table S1. **Lattice parameters from first-principles calculations.** Lattice constants a and c used in Fig. S1.

	FM	FM	A2	A2	A4	A4	in-AFM1	in-AFM1	DLM	DLM
x	a (Å)	c (Å)	a (Å)	c (Å)	a (Å)	c (Å)	a (Å)	c (Å)	a (Å)	c (Å)
1.000	2.86159	12.5069	2.86200	12.5043	2.86193	12.5053	2.87997	12.5382		
0.875	2.87052	12.4775	2.87499	12.4791						
0.750	2.87978	12.4607	2.87719	12.4612	2.87638	12.4706	2.89074	12.4815	2.88635	12.4932
0.625	2.88574	12.4342	2.88003	12.4402						
0.500	2.88722	12.3967	2.88176	12.4393	2.88270	12.4229	2.90244	12.3912	2.87758	12.4400
0.375	2.88881	12.3638	2.88501	12.4372						
0.250	2.88967	12.3357	2.88806	12.4415	2.88755	12.4057	2.90866	12.3340	2.88064	12.3982
0.125	2.88892	12.2987	2.88891	12.4449						
0.000	2.88726	12.2696	2.89380	12.4498	2.88860	12.3549	2.91583	12.2652	2.88225	12.3684

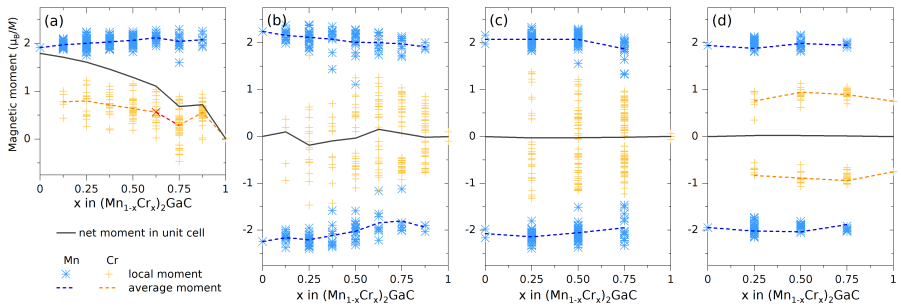

Figure S2. **Magnetic moments from first-principles calculations.** Calculated local and averaged magnetic moments of Cr and Mn along with net moment per M atom of $(Mn_{1-x}Cr_x)_2GaC$ for (a) FM, (b) AFM[0001]$^A_2$, (c) AFM[0001]$^A_4$, and (d) in-AFM1 spin configurations.

minimum at $x = 0.12$.

As described in the main text, all the films have a mixed (0 0 0 6) and (1 0 $\bar{1}$ 3) orientation. The fraction of (1 0 $\bar{1}$ 3) oriented grains was determined by comparing the measured (1 0 $\bar{1}$ 3) and (0 0 0 6) peak ratios to the theoretical values (100% and 18%, respectively). The peak ratios were acquired from symmetrical reciprocal space maps around the peaks to get their full volume intensity. The results are shown in Tab. S2. The (1 0 $\bar{1}$ 3) fraction increases from 49% in the pure Mn_2GaC to 71% in the sample with $x = 0.29$. We stress that both peaks correspond to the $(Mn_{1-x}Cr_x)_2GaC$ phase and that the films are phase pure but with a mixed orientation.

TEM imaging with EDX mapping was also performed with less magnification to examine the chemical uniformity of the films over larger length scales. The images are shown in Fig. S3. The STEM-HAADF image shows that the film thickness is uniform and the EDX maps indicate that there is no segregation of the elements on these length scales.

C. Temperature dependence of magnetic properties

Full hysteresis loop measurements were performed over a temperature range from 3 K to 750 K. Figure S4 shows the magnetization at 5 T up to 320 K, which can be considered as the saturation magnetization of the ferromagnetic response. It should be noted that 5 T is

Table S2. **Measured lattice parameters and critical temperature.** Lattice constants a and c for the $(Mn_{1-x}Cr_x)_2GaC$ MAX phase films, including the unit cell volume V_u and percentage of $(1\,0\,\bar{1}\,3)$ oriented grains, determined by XRD measurements.

x	a (Å)	c (Å)	V_u (Å^3)	% of $(1\,0\,\bar{1}\,3)$	T_c (K)
0.00	2.905	12.576	91.92	49	248
0.06	2.903	12.560	91.64	69	484
0.12	2.901	12.561	91.52	61	489
0.22	2.901	12.585	91.72	71	466
0.29	2.900	12.600	91.81	71	436

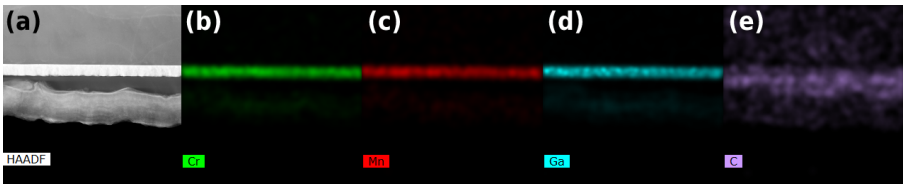

Figure S3. **Chemical composition overview.** Wider area TEM images of the $(Mn_{1-x}Cr_x)_2GaC$ film with $x = 0.22$ showing an STEM-HAADF image (a) with corresponding Cr-$K\alpha$ (b), Mn-$K\beta$ (c), Ga-$K\alpha$ (d) and C-$K\alpha$ (e) elemental EDX maps. The length scale can be seen from the film thickness, which is 140 nm. The elements are evenly distributed throughout the film.

the maximum field we can apply in the low-temperature Cryogenic system and in the film with $x = 0.00$ it is not clear whether this field is sufficient to saturate the magnetization fully at any temperature. The temperature dependence mostly mimics that of the remanent magnetization, except for the samples with $x \leq 0.06$. These samples have a fairly constant magnetization which is not typical of a ferromagnetic material. For temperatures above 320 K the magnetization was measured in a Lakeshore VSM system with a maximum field of 2 T. The lower field does not impact the magnetization of the samples with $x \geq 0.06$ but for the x = 0.00 sample this field is insufficient to induce the metamagnetic transition, which moves to increasingly higher fields with increasing temperature. Therefore, it was not measured above 320 K. The samples with $x > 0.06$ all show a temperature dependence

typical of the saturation magnetization of a ferromagnet. The highest magnetization is seen in the sample with $x = 0.12$ which reaches 516 kA/m (1.25 μ_B/M-atom) at 3 K.

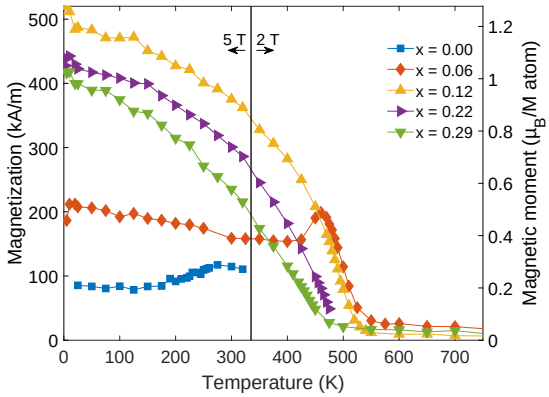

Figure S4. **Temperature dependence of the magnetization.** Magnetization as a function of temperature for the sample series. The data is combined from two different VSMs with different maximum fields, measured up to 5 T in the range 3-320 K, and up to 2 T in the range 300-750 K. The diamagnetic/paramagnetic background has been removed. Samples with $x = 0.12$ and above show typical ferromagnetic behavior and the magnetization is largest for $x = 0.12$.

The coercive field is shown in Fig. S5, as a function of temperature. All of the FM films have a similar coercive field in the range 12-18 mT at 300 K. The coercivity increases slowly as the temperature is reduced. The only outlier is the film with $x = 0.06$ where the increase is more pronounced, exceeding 50 mT at 3 K.

D. Resistivity

The film resistivity was determined at room temperature by four-probe resistance measurements. The results can be seen in Fig. S6 for the composition range studied. A trend similar to that of the c lattice parameter is observed, with a minimum in resistivity of approximately 360 $\mu\Omega\,$cm in the range $0.06 \leq x \leq 0.12$. The resistivity of the Mn_2GaC phase ($x = 0$) has been measured previously by Novoselova et al.[9] as 200 $\mu\Omega\,$cm, which is somewhat lower than the value found here. The resistivity is strongly dependent on grain structure

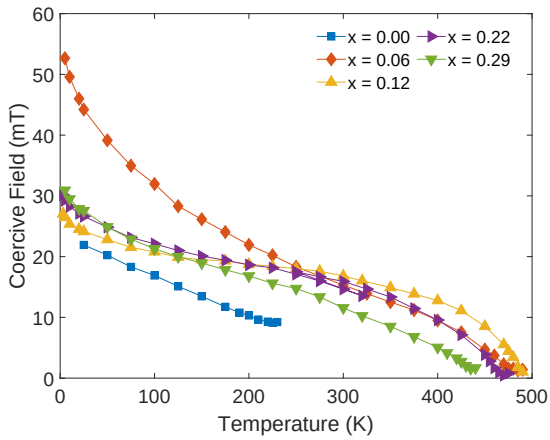

Figure S5. **Temperature dependence of the coercive field.** Coercive field as a function of temperature for the sample series. The coercive field is extracted up to the point where the remanence is reduced to zero.

and this value was obtained from a fully (0 0 0 1) oriented film. Our sample series has mixed (0 0 0 1) and (1 0 $\bar{1}$ 3) orientations which results in increased grain boundary scattering and a higher resistivity.

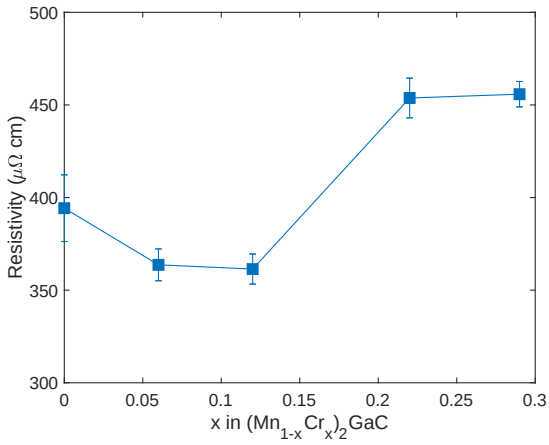

Figure S6. **Film resistivity.** The resistivity of the $(Mn_{1-x}Cr_x)_2GaC$ MAX phase films over the composition range studied. A minimum in resistivity is observed for x in the range 0.06-0.12.

REFERENCES

[1]M. Dahlqvist, A. S. Ingason, B. Alling, F. Magnus, A. Thore, A. Petruhins, A. Mockute, U. B. Arnalds, M. Sahlberg, B. Hjorvarsson, I. A. Abrikosov, and J. Rosen, Phys. Rev. B **93**, 014410 (2016).

[2]A. S. Ingason, A. Petruhins, M. Dahlqvist, F. Magnus, A. Mockute, B. Alling, L. Hultman, I. A. Abrikosov, P. O. A. Persson, and J. Rosen, Materials Research Letters **2**, 89 (2014).

[3]J. Etzkorn, M. Ade, D. Kotzott, M. Kleczek, and H. Hillebrecht, Journal of Solid State Chemistry **182**, 995 (2009).

[4]A. Petruhins, A. S. Ingason, M. Dahlqvist, A. Mockute, M. Junaid, J. Birch, J. Lu, L. Hultman, P. O. A. Persson, and J. Rosen, physica status solidi (RRL) – Rapid Research Letters **7**, 971 (2013).

[5]A. Petruhins, A. S. Ingason, J. Lu, F. Magnus, S. Olafsson, and J. Rosen, Journal of Materials Science **50**, 4495 (2015).

[6]A. Mockute, J. Lu, E. J. Moon, M. Yan, B. Anasori, S. J. May, M. W. Barsoum, and J. Rosen, Materials Research Letters **3**, 16 (2015).

[7]S. Lin, P. Tong, B. S. Wang, Y. N. Huang, W. J. Lu, D. F. Shao, B. C. Zhao, W. H. Song, and Y. P. Sun, Journal of Applied Physics **113**, 053502 (2013).

[8]A. Maniv, A. P. Reyes, S. K. Ramakrishna, D. Graf, A. Huq, D. Potashnikov, O. Rivin, A. Pesach, Q. Tao, J. Rosen, I. Felner, and E. N. Caspi, Journal of Physics: Condensed Matter **33**, 025803 (2020).

[9]I. P. Novoselova, A. Petruhins, U. Wiedwald, A. S. Ingason, T. Hase, F. Magnus, V. Kapaklis, J. Palisaitis, M. Spasova, M. Farle, J. Rosen, and R. Salikhov, Scientific Reports **8**, 2637 (2018).

Paper III

Growth and magnetic properties of epitaxial thin films of the i-MAX phase (Mn2/3Sc1/3)2GaC

E.B. Thorsteinsson, M. Dahlqvist, A. Elsukova, A. Petruhins, P. O. Å Persson, J. Rosen, A. S. Ingason, F. Magnus

Vacuum, 2025, Vol. 233, 113856

https://doi.org/10.1016/j.vacuum.2024.113856

Contributions: Synthesized the sample, performed all measurements except TEM, carried out data analysis and co-authored the paper.

Vacuum 233 (2025) 113856

Contents lists available at ScienceDirect

Vacuum

journal homepage: www.elsevier.com/locate/vacuum

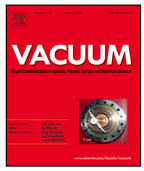

Growth and magnetic properties of epitaxial thin films of the *i*-MAX phase $(Mn_{2/3}Sc_{1/3})_2GaC$

E.B. Thorsteinsson [a,*], M. Dahlqvist [b], A. Elsukova [b], A. Petruhins [b], P.O.Å. Persson [b], J. Rosen [b], A.S. Ingason [c], F. Magnus [a]

[a] Science Institute, University of Iceland, Dunhaga 3, 107 Reykjavik, Iceland
[b] Department of Physics, Chemistry and Biology, Linköping University, SE-58183, Linköping, Sweden
[c] Grein Research ehf., Dunhaga 5, 107 Reykjavik, Iceland

ARTICLE INFO

Keywords:
MAX phases
Thin film
Magnetism
Antiferromagnetism
Magnetron sputtering

ABSTRACT

i-MAX phases are quaternary variants of the nanolaminated MAX phases, with additional in-plane ordering of the M atoms. The combination of in-plane and out-of-plane ordering potentially gives rise to complex magnetic behaviour. The *i*-MAX phase $(Mn_{2/3}Sc_{1/3})_2GaC$ has been synthesized in epitaxial thin film form on three different substrates, SiC-4H(001), MgO(111) and Al_2O_3(0001), by magnetron sputtering using elemental targets. Structural characterization by x-ray scattering and scanning transmission electron microscopy confirms the phase on all three substrates, although the highest crystal quality is obtained on SiC-4H(001). High-resolution images reveal the distinctive *i*-MAX structure, which is orthorhombic of space group *Cmcm*. Magnetic characterization reveals that the ground state is most likely antiferromagnetic. This confirms previous theoretical calculations which predicted an antiferromagnetic ground state and establishes the $(Mn_{2/3}Sc_{1/3})_2GaC$ *i*-MAX phase as a potential candidate for antiferromagnetic spintronic applications.

1. Introduction

Layered magnetic materials can give rise to a range of interesting properties, owing to their potential to combine the effects of competing intra- and interlayer magnetic interactions. MAX phases are a family of materials composed of a transition metal (M), an A-group element (A) and either carbon or nitrogen (X) with the chemical formula $M_{n+1}AX_n$ (n = 1, 2, 3), that naturally form a distinctive layered structure with highly anisotropic properties [1]. For n = 1, the crystal structure is composed of atomic layers with the order M-A-M-X-M-A-M-X. A number of magnetic MAX phases has been identified, with complex magnetic ordering ranging from helical to antiferromagnetic or ferromagnetic [2,3]. In 2017, a new class of MAX phases was discovered with an additional in-plane ordering within the M layers, the so called *i*-MAX phases [4,5]. In these materials, the M sites are shared by two elements, M^1 and M^2 with the common formula $(M^1_{2/3}M^2_{1/3})_2AX$. M^1 forms a honeycomb pattern where M^2 is positioned in the centre of each hexagon but slightly shifted towards the A-layer. The shift of M^2 towards the A-layer has an impact on the A-layer which then takes on a Kagomé-like pattern. The *i*-MAX phases represent yet another avenue to tune the magnetic ordering of MAX phases, by controlling the magnetic interactions within and between the magnetically ordered M layers [6–8].

The most studied of the magnetic MAX phases is Mn_2GaC, which has a ferromagnetic-like response below 210 K above which it undergoes a transition to antiferromagnetic ordering [9–13]. Lately, there has been a renewed interest in antiferromagnets for spintronics due to their inherent stability in large external fields and their fast magnetization dynamics compared to ferromagnets [14,15]. This interest has not least been fuelled by the realization that the magnetization in antiferromagnets can in some cases be manipulated by electric currents [16–18]. The combination of the highly anisotropic nanolaminated MAX phase structure and an antiferromagnetic ordering could therefore be highly appealing for spintronic devices. Furthermore, we have recently shown that by partially substituting Mn by Cr on the M site (in the range 6 to 29 at.%) a ferromagnetic ordering with a large magnetization is obtained up to temperatures far exceeding room temperature [19]. The ferromagnetic response was associated with a contraction in the unit cell volume hinting at the importance of tuning both the Mn–Mn and Mn–Ga atomic distances to control the magnetic ordering [20]. This was the first demonstration of a substantial ferromagnetic response in a MAX phase material at room temperature, paving the way for potential applications in magnetics and spintronics utilizing ferromagnetic properties.

* Corresponding author.
E-mail address: eth44@hi.is (E.B. Thorsteinsson).

https://doi.org/10.1016/j.vacuum.2024.113856
Received 11 September 2024; Received in revised form 31 October 2024; Accepted 20 November 2024
Available online 28 November 2024

Similarly, Petruhins et al. [21] have studied substitution of Mn by Sc to form the *i*-MAX phase $(Mn_{2/3}Sc_{1/3})_2GaC$ through ab initio calculations and solid state synthesis. They found that $(Mn_{2/3}Sc_{1/3})_2GaC$ is indeed stable and predicted theoretically that the ground state was antiferromagnetic, although it was close to degenerate in energy with a ferromagnetic spin arrangement. However, the magnetic properties remain to be studied experimentally. Thin film synthesis methods offer important advantages in this respect as they allow control over crystal orientation (through epitaxy for example) and thickness [2], as well as being more relevant to applications in spintronics.

In the present study we use thin film deposition techniques to synthesize the *i*-MAX phase $(Mn_{2/3}Sc_{1/3})_2GaC$ as an epitaxial film, by substituting Sc into the Mn layer. We show that $(Mn_{2/3}Sc_{1/3})_2GaC$ films can be grown epitaxially on different commonly available single-crystal substrates. Furthermore, we use the phase-pure films to study the magnetic ground state.

2. Experimental methods

The films were grown by direct current magnetron sputtering (dcMS) on 1 × 1 cm^2 substrates of SiC-4H(0 0 1), MgO(1 1 1) and Al_2O_3(0 0 0 1), using a 7.5 cm 99.9% pure manganese target, a 7.5 cm 99.99% carbon target, a 5.0 cm 99.9% scandium target and a liquid gallium target made from 99.9999% gallium pellets in a specially made 5.0 cm crucible attached to the magnetron (see Refs. [19] and [13]). For the duration of the growth the Ga target was in liquid form. Pressure was maintained at 0.40 Pa as measured by a capacitance manometer with 99.999% pure argon gas set to a 20 sccm flow rate and further controlled by a butterfly throttle valve. The vacuum chamber has a base pressure of $< 5 \times 10^{-7}$ Pa, but at the growth temperature of 720 °C, the base pressure increased to 5×10^{-6} Pa after preheating the substrate for 50 min. The sample holder was rotated ± 360° at a rate of 12 revolutions per minute.

The structural properties of the films were investigated by X-ray diffraction (XRD) using a Panalytical Empyrean diffractometer in line focus mode using Cu Kα source. For diffraction measurements, the incident side had a 2 bounce hybrid monochromator with a 1/8° divergence slit and on the diffracted side a PIXcel^{3D} detector operating in 1D mode. Pole figure measurements were done with the hybrid monochromator and a 1/4° divergence slit while the diffracted side had a 0.28° parallel plate collimator and 0.04 rad soller slits with the detector in 0D mode. The mean film thickness was estimated to be around 63 nm by utilizing an X-ray reflectivity (XRR) measurement on a Mn_2GaC film with comparable magnetron power values from the same growth session, as the $(Mn_{2/3}Sc_{1/3})_2GaC$ films did not give usable XRR scans due to high surface roughness.

Scanning transmission electron microscopy (STEM) was carried out in the Linköping double-corrected, monochromated, high-brightness FEI Titan^3 at 300 kV. Cross-sectional samples were first mechanically polished to a thickness of about 50 μm, followed by ion-beam milling with Ar^+ in a Gatan precision ion polishing system (PIPS) at 5 keV with a final polishing step at 1 keV of ion energies.

The magnetic properties were measured by vibrating sample magnetometry (VSM) in the temperature range from 10 K to 300 K with a 5 T cryogen free magnet system from Cryogenic (not shown) and 80 K to 850 K with a 2 T Lakeshore 8600 magnetometer. The magnetic moment was measured at a fixed applied field while ramping the temperature and full hysteresis measurements were carried out at regular temperature intervals.

3. Results and discussion

3.1. Structural characterization

The optimal growth conditions for Mn_2GaC films were used as the starting point for the optimization of the $(Mn_{2/3}Sc_{1/3})_2GaC$ *i*-MAX phase. The growth of Mn_2GaC has been described previously in a number of publications [9,10,13,19]. To obtain the $(Mn_{2/3}Sc_{1/3})_2GaC$ phase, the Mn flux was reduced while Sc was added, by varying the power on the two magnetrons appropriately. XRD measurements were used to analyse the phase formation and crystal quality. The optimum growth temperature for the $(Mn_{2/3}Sc_{1/3})_2GaC$ phase was found to be 720 °C, as compared to 550 °C for Mn_2GaC films. For Mn_2GaC films, such high growth temperatures result in the formation of a considerable amount of the competing phase Mn_3GaC, however, we did not encounter this for the $(Mn_{2/3}Sc_{1/3})_2GaC$ system.

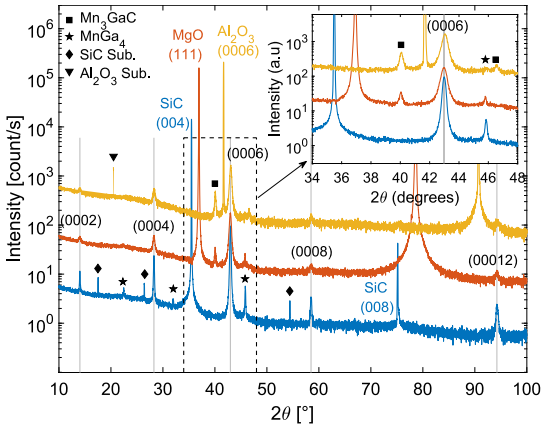

Fig. 1. XRD scans of $(Mn_{2/3}Sc_{1/3})_2GaC$ films grown at 720 °C on SiC (blue), MgO (orange) and Al_2O_3 (yellow) substrates. The scans are shifted by a factor of 10 successively in intensity for clarity. The inset focuses on the MAX phase (0 0 0 6) peak. All substrates yield the $(Mn_{2/3}Sc_{1/3})_2GaC$ phase but the best crystal quality is obtained on the SiC substrate.

Table 1
Lattice parameters extracted from peaks on the SiC film, compared to bulk values from Petruhins et al. [21].

Lattice par.	Bulk [Å]	On SiC [Å]	Change
a	9.0565	9.019	−0.42%
b	5.2150	5.239	0.45%
c	12.6276	12.613	−0.12%

Fig. 1 shows XRD scans of films grown at 720 °C on three different substrates deposited at the same time, SiC-4H(0 0 1), MgO(1 1 1) and Al_2O_3(0 0 0 1). The epitaxial growth of MAX phase films is observed on all three substrates, as indicated by the distinctive set of (0 0 0 *l*) peaks, and the peak positions match those of the $(Mn_{2/3}Sc_{1/3})_2GaC$ *i*-MAX phase [21]. The $(Mn_{2/3}Sc_{1/3})_2GaC$ phase is therefore formed on all three substrates. The films grown on both Al_2O_3 and MgO show the presence of a Mn_3GaC secondary phase (star), estimated at 4.3% and 27.3% of the total film volume, respectively, while the film on SiC only has a minor contamination of $MnGa_4$ (square), estimated at 1.3%. The estimates for the competing phases were based on peak area intensity scaled relative to their respective 100% relative intensities. The film grown on SiC has the best crystallinity out of these substrates, with more than twice the area intensity of the (0 0 0 6) peak compared to the films on Al_2O_3 and MgO. Lattice parameters were extracted from the SiC film by using the peak position of the (0 0 0 6), $(3\,1\,\bar{4}\,3)$ and $(1\,1\,\bar{2}\,5)$ peaks, and can be seen in Table 1. The film lattice parameters agree quite well with the bulk values.

In order to examine the in-plane ordering of the films we have carried out pole figure measurements centred at $2\theta = 40.68°$, the position of the 100% relative intensity $(3\,1\,\bar{4}\,3)$ plane. Fig. 2(a) shows a pole figure measured on the film grown on the SiC substrate. Several

Table 2
Overview of the crystal planes visible in the pole figure seen in Fig. 2, showing the 2θ position, the χ angle relative to the (0001) plane and the relative intensity.

Plane	2θ (°)	χ (°)	Rel. Int. (%)
$(22\bar{4}1)$	40.45	79.8	35.7
$(02\bar{2}3)$	40.56	58.1	47.0
$(31\bar{4}3)$	40.68	58.2	100
$(11\bar{2}5)$	40.92	29.1	27.1

planes of $(Mn_{2/3}Sc_{1/3})_2GaC$ are visible, as they have a very similar d-spacing. An overview of these peaks can be seen in Table 2. Due to the overlap in the polar angle χ, between the $(02\bar{2}3)$ and $(31\bar{4}3)$ planes we cannot distinguish between them, however, the $(22\bar{4}1)$ and $(11\bar{2}5)$ planes can be clearly seen at their respective χ angles. From the clear distinct peaks in the pole figure we can see that the film is mainly epitaxial in nature, while the presence of a ring feature indicates that the film also contains a partially textured component. However, the fact that these planes can be seen is further confirmation that this is the $(Mn_{2/3}Sc_{1/3})_2GaC$ *i*-MAX phase.

More information about the film morphology and texture can be deduced from SEM images of the surface, as shown in Fig. 2(b). The film is composed of smooth platelets, presumably corresponding to the (000*l*) oriented crystal grains, with smaller irregular grains in between. This correlates well with the pole figure, where the majority of the film has a well defined epitaxial relationship with the substrate, while a minority of the crystallites have a uniformly distributed in-plane orientation. The high surface roughness is also evident, in agreement with the XRR measurements (not shown).

STEM imaging was carried out on the film grown on SiC to examine the *i*-MAX structure further. Fig. 3 shows images acquired along the [100] and [110] crystallographic zone axes. Low-magnification images (a) and (d) show that the film is indeed quite rough and composed of grains with a large variation in size, possibly with some voids in between. Again, this is consistent with the XRR measurements which indicated a high film roughness and the surface morphology seen in Fig. 2(b). The thickness of the regular grains is found to be around 90 nm, so taking into account the irregular grain structure this is quite consistent with the estimated mean film thickness of 63 nm. High-resolution images (c) and (f) reveal the distinctive *i*-MAX structure, which is orthorhombic of space group *Cmcm* (#63). The structure is shown schematically on the right for the two different directions. For the [100] direction, the structure looks almost identical to the conventional MAX phase structure where the slight difference in the positions of Mn and Sc atoms cannot be distinguished. However, when viewed along the [110] direction, the slight shift of the Sc atoms from the M layer towards the Ga layer becomes apparent. In Fig. 3f, the Ga-layer is composed of alternating bright and dark spots which is a result of its Kagomé-like lattice. This is characteristic of the *i*-MAX structure and is consistent with results on bulk samples [21]. Energy-dispersive X-ray spectroscopy (EDX) was also done in the STEM. Elemental maps showed a uniform distribution in the areas sampled (not shown). The resulting chemical composition was found to be 47.0 at.% Mn, 23.9 at.% Sc and 29.1 at.% Ga (C content cannot be reliably determined). That gives a Mn/Sc ratio of 1.97, which is very close to the expected value of 2. The Ga is slightly low, at 29.1 at.%, with the expected value being 33.3 at.% when excluding C.

3.2. Magnetic properties

The XRD shows that films on both Al_2O_3 and MgO substrates contain a small amount of Mn_3GaC, which is known to be antiferromagnetic at low temperature and ferromagnetic in the temperature range of approximately 165–265 K [23–25]. Therefore, we focus on the films grown on SiC for magnetic characterization, which only have minimal amounts of $MnGa_4$, which is antiferromagnetic and in this concentration should

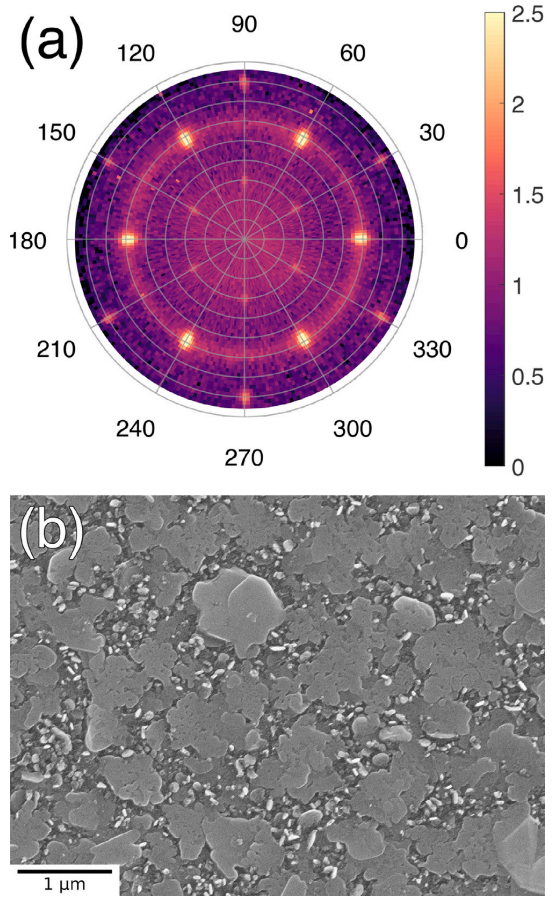

Fig. 2. (a) Pole figure of the $(Mn_{2/3}Sc_{1/3})_2GaC$ film on SiC, measured at $2\theta = 40.68°$, showing $(22\bar{4}1)$ peaks at $\chi = 79.8°$, $(31\bar{4}3)$ peaks at $\chi = 58.2°$ and $(11\bar{2}5)$ peaks at $\chi = 29.1°$, with respect to the (0001) plane. The intensity is on a logarithmic scale. For a more detailed overview of the planes, see Table 2. Grey circles are drawn every 10° in χ for visual aid. (b) A SEM image showing the surface morphology of the film on SiC.

not have significant effects on the overall magnetic response [26]. A selection of characteristic magnetization curves at different temperatures on a sample deposited on SiC is shown in Fig. 4. No background subtraction has been carried out and therefore the dominant feature is the diamagnetic response of the SiC substrate and sample holder. Corresponding magnetization measurements of a bare substrate of equal size (volume) are shown in the inset for reference. The slight S-shape at low fields is apparent in the substrate measurements and can therefore be attributed to very small amounts of magnetic impurities or defects in the substrate itself [27] or the adhesive used to attach the sample to the sample holder. No ferromagnetic response can be detected from the film in the temperature range of 10–750 K.

In order to determine the presence of antiferromagnetic ordering we examine the DC volume susceptibility as a function of temperature both with the field applied parallel and perpendicular to the film plane. This was done by fitting the slope above 1 T on the measured hysteresis loops. Fig. 5(a) shows the susceptibility, normalized to the value at the lowest temperature. The SiC substrate is diamagnetic [27] and its susceptibility should therefore be independent of temperature but we

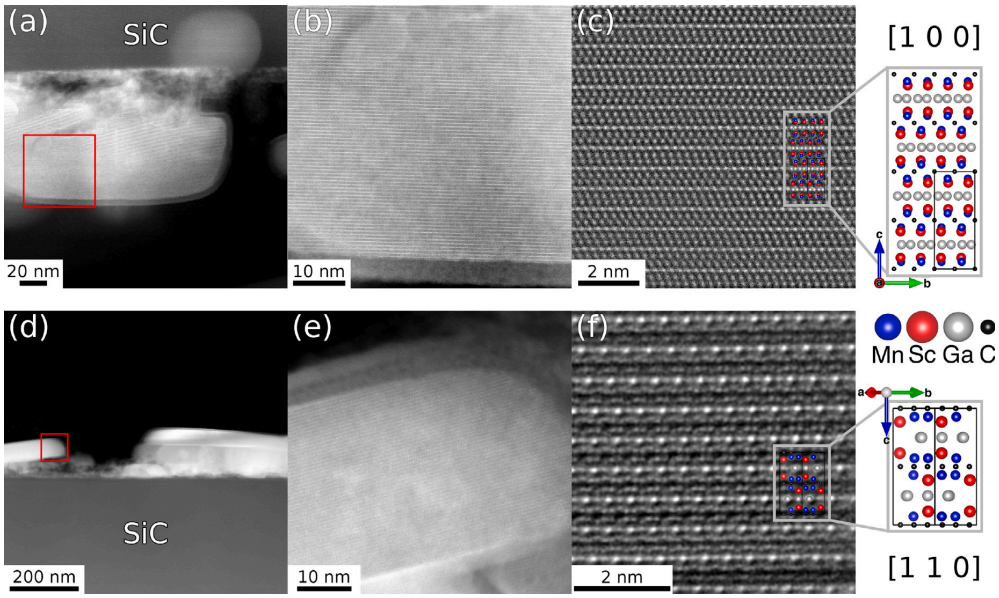

Fig. 3. HAADF-STEM images of a $(Mn_{2/3}Sc_{1/3})_2GaC$ film where (a–c) are viewed in the [1 0 0] direction and (d–f) are viewed in [1 1 0] direction. (a, d) Overview images. (b, e) Higher resolution of the area marked with a red square in the overview images. (c, f) Atomically resolved images in the [1 0 0] and [1 1 0] directions, respectively. The atomic structure is shown schematically on the right, as drawn by VESTA [22].

observe a slight decrease in its susceptibility with increasing temperature. Again, this can be attributed to the small amounts of magnetic impurities in the substrate itself or the adhesive. The susceptibility of the sample decreases more rapidly with temperature at first but notably there is a distinct difference between the in-plane and out-of-plane response. The susceptibility perpendicular to the plane starts to increase with temperature above approximately 200 K whereas the in-plane susceptibility decreases monotonically.

This difference is accentuated with the substrate susceptibility subtracted, as shown in Fig. 5(b), revealing the susceptibility of the film only. Here the susceptibility in the in-plane direction is seen to be almost temperature independent whereas in the out-of-plane direction it increases with temperature. This is consistent with the behaviour of antiferromagnets below the Néel temperature where the susceptibility is temperature independent in the direction perpendicular to the magnetization ($\chi_\perp$ constant) and increasing with temperature parallel to the magnetization ($\chi_\parallel$ increasing) [28].

The magnetization and DC susceptibility measurements combined show that $(Mn_{2/3}Sc_{1/3})_2GaC$ is not ferromagnetic but shows signs of antiferromagnetism. This is consistent with the theoretical predictions of Petruhins et al. [21] who predicted that an antiferromagnetic ground state was slightly favoured over the ferromagnetic one. The predicted antiferromagnetic ground state is shown schematically in Fig. 6, where the magnetic moment is carried by the Mn atoms and the moments of adjacent Mn layers are antiparallel. The susceptibility measurements indicate that the preferred magnetization axis is perpendicular to the film plane which means that the Mn moments are perpendicular to the $(000l)$ planes (parallel to the c axis), as shown in the figure. Unfortunately, heating the samples to 850 K and above results in irreversible structural and magnetic changes to the film, and therefore it is impossible to reach the Néel temperature and confirm that a magnetic phase transition exists. Further measurements, including for example neutron diffraction, would be required to unequivocally determine the antiferromagnetic ordering.

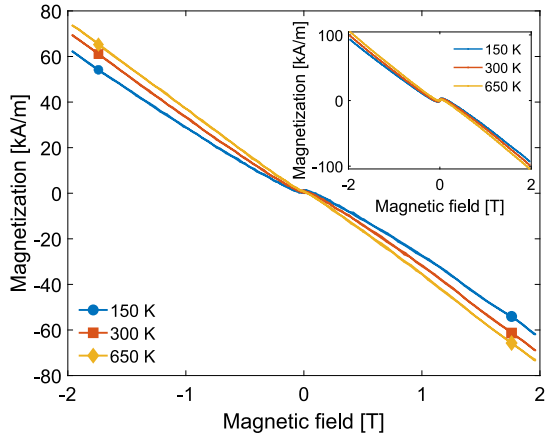

Fig. 4. Magnetization scans of the $(Mn_{2/3}Sc_{1/3})_2GaC$ film on SiC(0 0 1) at 150 K, 300 K and 650 K. The inset shows measurements of a SiC substrate of equal size at the same temperatures.

4. Conclusions

We have synthesized the *i*-MAX phase $(Mn_{2/3}Sc_{1/3})_2GaC$ in thin film form on SiC-4H(0 0 1), Al_2O_3(0 0 0 1) and MgO(1 1 1) as confirmed by structural characterization with XRD and STEM. The highest film quality was obtained on the SiC substrate with over twice the peak area intensity of the (0 0 0 6) peak compared to the other substrates and the least amount of competing phases as seen by XRD. This is the first time this phase is made in thin film form, having been previously made only in bulk [21]. Magnetic measurements with VSM show that the $(Mn_{2/3}Sc_{1/3})_2GaC$ *i*-MAX phase is not ferromagnetic. However,

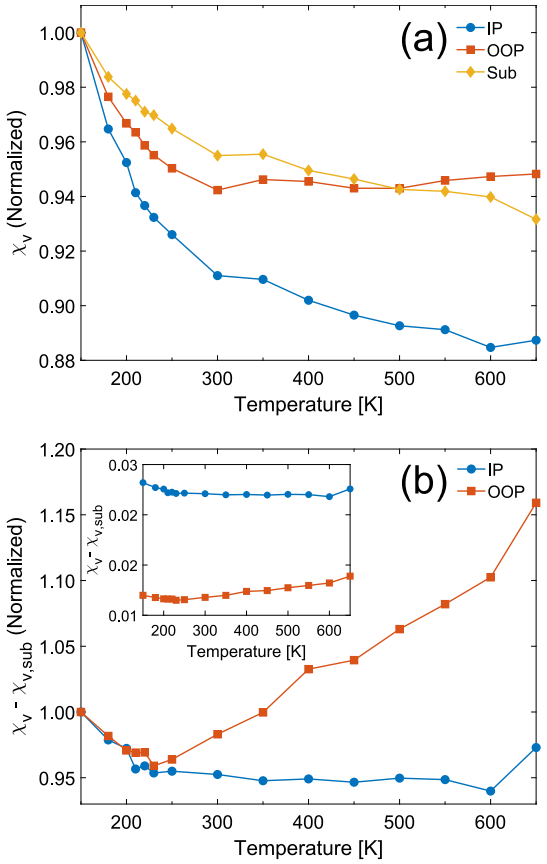

Fig. 5. Volume magnetic susceptibility extracted from hysteresis loops. (a) Normalized susceptibility for the in-plane (IP) and out-of-plane (OOP) directions on $(Mn_{2/3}Sc_{1/3})_2GaC$ films grown on a SiC substrate, as well as an in-plane measurement of a bare SiC substrate (Sub) of equal size. (b) Normalized susceptibility after subtracting the signal from the substrate. The inset shows the non-normalized data.

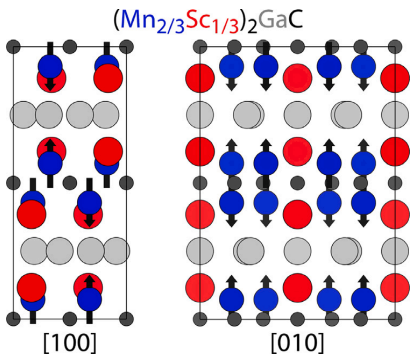

Fig. 6. Schematic of the lowest energy configuration of antiferromagnetic spin order for $(Mn_{2/3}Sc_{1/3})_2GaC$, as predicted by Petruhins et al. [21].

magnetic susceptibility measurements indicate that the ground state may be antiferromagnetic as predicted by theory, with alternating Mn layers of antiparallel moments along the *c* axis. The highly anisotropic nanolaminated structure of the *i*-MAX phase, coupled with antiferromagnetic ordering, means that $(Mn_{2/3}Sc_{1/3})_2GaC$ could for example be of interest for a range of antiferromagnetic spintronics applications.

CRediT authorship contribution statement

E.B. Thorsteinsson: Writing – review & editing, Writing – original draft, Investigation, Formal analysis. **M. Dahlqvist:** Writing – review & editing, Investigation, Conceptualization. **A. Elsukova:** Investigation. **A. Petruhins:** Writing – review & editing, Investigation. **P.O.Å. Persson:** Writing – review & editing, Funding acquisition. **J. Rosen:** Writing – review & editing, Funding acquisition, Conceptualization. **A.S. Ingason:** Writing – review & editing, Conceptualization. **F. Magnus:** Writing – review & editing, Writing – original draft, Supervision, Project administration, Funding acquisition, Conceptualization.

Declaration of competing interest

The authors declare that they have no known competing financial interests or personal relationships that could have appeared to influence the work reported in this paper.

Acknowledgements

This work was funded by the University of Iceland Research Fund and the Icelandic Research Fund (Grant Nos. 174271 and 217843). The authors also acknowledge ARTEMI, the Swedish National Infrastructure in Advanced Electron Microscopy, supported by the Swedish Research Council and the Swedish Foundation for Strategic Research (Grant Nos. 2021-00171 and RIF21-0026). Computational resources provided by the National Academic Infrastructure for Supercomputing in Sweden (NAISS) at the National Supercomputer Centre (NSC) partially funded by the Swedish Research Council through grant agreement no. 2022-06725.

Data availability

Data will be made available on request.

References

[1] M.W. Barsoum, Prog. Solid State Chem. 28 (2000) 201.
[2] A.S. Ingason, A. Mockute, M. Dahlqvist, F. Magnus, S. Olafsson, U.B. Arnalds, B. Alling, I.A. Abrikosov, B. Hjörvarsson, P.O. Å. Persson, J. Rosen, Phys. Rev. Lett. 110 (2013) 195502.
[3] M. Dahlqvist, M.W. Barsoum, J. Rosen, Mater. Today 72 (2024) 1.
[4] M. Dahlqvist, J. Lu, R. Meshkian, Q. Tao, L. Hultman, J. Rosen, Sci. Adv. 3 (2017) e1700642.
[5] M. Dahlqvist, J. Rosen, Nanoscale 14 (2022) 10958.
[6] J. Yang, G. Yao, S. Sun, Z. Chen, S. Yuan, K. Wu, X. Fu, Q. Wang, W. Cui, Carbon 179 (2021) 104.
[7] Q. Tao, J. Lu, M. Dahlqvist, A. Mockute, S. Calder, A. Petruhins, R. Meshkian, O. Rivin, D. Potashnikov, E.N. Caspi, H. Shaked, A. Hoser, C. Opagiste, R.-M. Galera, R. Salikhov, U. Wiedwald, C. Ritter, A.R. Wildes, B. Johansson, L. Hultman, M. Farle, M.W. Barsoum, J. Rosen, Chem. Mater. 31 (2019) 2476, http://dx.doi.org/10.1021/acs.chemmater.8b05298.
[8] J. Yang, R. Liu, N. Jia, K. Wu, X. Fu, Q. Wang, W. Cui, Carbon 183 (2021) 76.
[9] A.S. Ingason, A. Petruhins, M. Dahlqvist, F. Magnus, A. Mockute, B. Alling, L. Hultman, I.A. Abrikosov, P.O. Å. Persson, J. Rosen, Mater. Res. Lett. 2 (2013) 89.
[10] M. Dahlqvist, A.S. Ingason, B. Alling, F. Magnus, A. Thore, A. Petruhins, A. Mockute, U.B. Arnalds, M. Sahlberg, B. Hjörvarsson, I.A. Abrikosov, J. Rosen, Phys. Rev. B 93 (2016) 014410.
[11] I.P. Novoselova, A. Petruhins, U. Wiedwald, A.S. Ingason, T. Hase, F. Magnus, V. Kapaklis, J. Palisaitis, M. Spasova, M. Farle, J. Rosen, R. Salikhov, Sci. Rep. 8 (2018) 1.
[12] J. Dey, E. Jedryka, R. Kalvig, U. Wiedwald, M. Farle, J. Rosen, M. Wójcik, Phys. Rev. B 108 (2023) 054413.
[13] E.B. Thorsteinsson, A.S. Ingason, F. Magnus, Phys. Rev. Mater. 7 (2023) 034409.
[14] T. Jungwirth, X. Marti, P. Wadley, J. Wunderlich, Nature Nanotechnology 11 (2016) 231.

[15] V. Baltz, A. Manchon, M. Tsoi, T. Moriyama, T. Ono, Y. Tserkovnyak, Rev. Modern Phys. 90 (2018) 015005.
[16] P. Wadley, B. Howells, J. Železný, C. Andrews, V. Hills, R.P. Campion, V. Novák, K. Olejník, F. Maccherozzi, S.S. Dhesi, S.Y. Martin, T. Wagner, J. Wunderlich, F. Freimuth, Y. Mokrousov, J. Kuneš, J.S. Chauhan, M.J. Grzybowski, A.W. Rushforth, K.W. Edmonds, B.L. Gallagher, T. Jungwirth, Science 351 (2016) 587.
[17] S.Y. Bodnar, L. Šmejkal, I. Turek, T. Jungwirth, O. Gomonay, J. Sinova, A.A. Sapozhnik, H.-J. Elmers, M. Kläui, M. Jourdan, Nature Commun. 9 (2018) 348.
[18] A.K. Nayak, J.E. Fischer, Y. Sun, B. Yan, J. Karel, A.C. Komarek, C. Shekhar, N. Kumar, W. Schnelle, J. Kübler, C. Felser, S.S.P. Parkin, Sci. Adv. 2 (2016) e1501870, 1511.03128.
[19] E.B. Thorsteinsson, M. Dahlqvist, A. Elsukova, A. Petruhins, P.O. Å. Persson, J. Rosen, A.S. Ingason, F. Magnus, APL Mater. 11 (2023) 121102.
[20] J.M.D. Coey, J. Phys.-Conden. Matter 26 (2014) 064211.
[21] A. Petruhins, M. Dahlqvist, J. Lu, L. Hultman, J. Rosen, Cryst. Growth Des. 20 (2020) 55.
[22] K. Momma, F. Izumi, J. Appl. Crystallogr. 44 (2011) 1272.
[23] T. Kanomata, M. Kikuchi, T. Kaneko, K. Kamishima, M. Bartashevich, H. Katori, T. Goto, Solid State Commun. 101 (1997) 811.
[24] M.-H. Yu, L.H. Lewis, A.R. Moodenbaugh, J. Appl. Phys. 93 (2003) 10128, https://pubs.aip.org/aip/jap/article-pdf/93/12/10128/19013487/10128_1_online.pdf.
[25] A. Petruhins, A.S. Ingason, S. Olafsson, J. Rosen, Mater. Res. Express 7 (2020) 106102.
[26] V.Y. Verchenko, A.A. Tsirlin, D. Kasinathan, S.V. Zhurenko, A.A. Gippius, A.V. Shevelkov, Phys. Rev. Mater. 2 (2018) 044408.
[27] Y. Wang, Y. Liu, G. Wang, W. Anwand, C.A. Jenkins, E. Arenholz, F. Munnik, O.D. Gordan, G. Salvan, D.R.T. Zahn, X. Chen, S. Gemming, M. Helm, S. Zhou, Sci. Rep. 5 (2015) 8999, 1503.00487.
[28] S. Blundell, Magnetism in Condensed Matter, in: Oxford Master Series in Physics, Oxford University Press, USA, 2001.

Paper IV

Ferromagnetism at room temperature in Cr-doped polycrystalline Mn_2GaC MAX phase thin films

E.B. Thorsteinsson, D. Dagbjartsson, A. S. Ingason, F. Magnus

Applied Physics Letters, 2025, 127, 052408

https://doi.org/10.1063/5.0279839

Contributions: Synthesized the samples, performed X-ray pole figures, partially did VSM measurements and co-authored the paper

Applied Physics Letters ARTICLE pubs.aip.org/aip/apl

Ferromagnetism at room temperature in Cr-doped polycrystalline Mn_2GaC MAX phase thin films

Cite as: Appl. Phys. Lett. **127**, 052408 (2025); doi: 10.1063/5.0279839
Submitted: 8 May 2025 · Accepted: 24 July 2025 ·
Published Online: 7 August 2025

View Online Export Citation CrossMark

E. B. Thorsteinsson,[1] D. Dagbjartsson,[1] A. S. Ingason,[2] and F. Magnus[1,a)]

AFFILIATIONS

[1]Science Institute, University of Iceland, Dunhaga 5, 107 Reykjavik, Iceland
[2]Grein Research ehf, Dunhaga 5, 107 Reykjavik, Iceland

[a)]Author to whom correspondence should be addressed: fridrikm@hi.is

ABSTRACT

Magnetic MAX phases are nanolaminated compounds where competing interactions within and between laminae shape their complex magnetic ordering. The resulting low magnetization and ordering temperature has limited their use in practice but the search for ferromagnetism at room temperature has been ongoing. Here, we show that a strong ferromagnetic response can be obtained at room temperature in the MAX phase Mn_2GaC by partially substituting Mn by Cr. Polycrystalline (0001) textured $(Mn_{1-x}Cr_x)_2GaC$ films are obtained on SiO_2/Si (001) substrates for $0 \leq x \leq 0.29$ and films with $0.06 \leq x \leq 0.29$ show a ferromagnetic response at room temperature. The magnetization peaks at $M_s = 420 \pm 20$ kA/m for $x = 0.12$. The films with $x > 0.06$ have an in-plane magnetic anisotropy and are isotropic within the film plane. The results show that the room temperature ferromagnetic response in Cr-doped Mn_2GaC is not restricted to single-crystal films which facilitates its use in device applications and bulk magnets.

Magnetic multilayers give rise to a variety of complex magnetic ordering due to competing interactions, interface effects, and finite size effects. Many applications such as traditional magnetic sensors and more exotic spintronic devices based on topological spin textures rely on our understanding of these effects and the ability to manipulate them. New layered magnetic systems continue to emerge, bringing new possibilities and challenges. MAX phases are intrinsically nanolaminated materials composed of an early transition metal (M), an A-group element (A) and C, N, B, or P (X).[1] They share a common hexagonal crystal structure where the M, A, and X elements arrange in a distinct layer sequence in the *c*-axis direction. The M-A bonds are more metallic compared to the more covalent-like M-X bonds, which leads to highly anisotropic properties within and between *c* planes. The interest in MAX phases was initially sparked by their unusual mechanical properties,[2,3] but more recently the prospect of combining the nanolaminated structure with magnetism has stimulated the search for new MAX phases with magnetic elements.[1,4]

The first magnetic MAX phase, $(Cr_{0.75}Mn_{0.25})_2GeC$, was discovered[5] in 2013 and was found to be weakly ferromagnetic below approximately 200 K, as well as having a significant magnetic response without remanence at room temperature. In the following decade, a flurry of new magnetic MAX phases appeared, mostly by including Mn, Cr, or Fe on the M-site[5–16] or Mn, Fe, Co, and/or Ni on the A-site.[17–19] What all of these materials have in common is that the remanent magnetization is zero or negligible at room temperature, meaning that they are not particularly promising as magnetic materials in practice.

The low magnetization is a result of the competing magnetic interactions within the M layers and between M layers across the A layers. This typically results in antiferromagnetic or non-collinear ordering with no or only a small ferromagnetic component. The prototypical case is the Mn_2GaC phase, which has a small ferromagnetic moment below 210 K, above which it undergoes a magnetic phase transition to non-collinear antiferromagnetic ordering.[11–13] Both the high and low temperature magnetic states are thought to be transverse helical where each Mn-C-Mn slab can be considered a supermoment which is rotated by a certain temperature-dependent angle with respect to the next Mn-C-Mn slab.[20,21] Recently, however, we have shown that by partially substituting Mn with Cr in epitaxial films of the MAX phase $(Mn_{1-x}Cr_x)_2GaC$, a strong ferromagnetic response can be obtained, even at room temperature.[22] The precise nature of the magnetic ordering is still not known but a large remanent magnetization is seen, with a temperature dependence resembling that of a ferro- or ferrimagnet. Room temperature ferromagnetism (or other ordering with a large net magnetization) is essential for any practical applications in bulk magnets or ferromagnetic spintronics. The films were grown on

single-crystal MgO(111) substrates which promoted an epitaxial growth of two distinct crystal orientations. While highly promising, such stringent substrate requirements limit the possibilities for integration into devices or realization of the material in the bulk.

For practical applications, it is important to be able to obtain ferromagnetic MAX phases without the complexity of epitaxial growth. Here, we show that a room temperature ferromagnetic response can be obtained in the well-known Mn_2GaC MAX phase by doping with Cr and that a large magnetization can be obtained even in polycrystalline films grown on silicon substrates. We furthermore examine the magnetic anisotropy of the ferromagnetic films.

The $(Mn_{1-x}Cr_x)_2GaC$ films were grown by dc magnetron sputtering in an ultrahigh vacuum system with a base pressure below 5×10^{-7} Pa. Four elemental sources were used, arranged in a confocal geometry, allowing precise control of the film stoichiometry. The Ga source was positioned horizontally, facing upward, and equipped with a custom-built crucible to contain the molten Ga during sputtering (Ga has a melting point of only 29.76 °C). The process gas was Ar at a pressure of 0.4 Pa. The sputtering power ranged from 12 W (for the Ga) to 300 W (for the C), giving a total growth rate of approximately 0.16 nm/s. Films with a composition in the range $0.00 \leq x \leq 0.29$ were produced by varying the Mn and Cr power, while keeping the total Mn and Cr flux constant. The Mn:Cr ratio was confirmed by energy dispersive x-ray spectroscopy measurements in a scanning electron microscope, from which we estimate an uncertainty of $\Delta x = 0.03$. Each film was measured by x-ray reflectivity (XRR) to determine its thickness, which was found to be in the range 138–143 nm (± 2 nm). XRR also shows that the film roughness is quite high, approximately 6.5 nm, which is typical of MAX phase thin films.[23] The substrates were Si (001), with a native oxide layer, and they were kept at 550 °C during deposition. Further details regarding the growth process can be found in Refs. 13 and 22.

The film structure can be seen in Fig. 1. The structure is that of an $M_{n+1}AX_n$ phase with $n = 1$, which has a repeated M–A–M–X–M–A–M–X layering in the c-axis direction. The Cr atoms randomly replace Mn on the M sites,[22] as shown schematically in Fig. 1(a). X-ray diffraction (XRD) measurements were carried out in a Panalytical Empyrean system with Cu K-α radiation, to determine the phase purity and crystal structure. The θ–2θ scans [Fig. 1(b)] show the characteristic series of (000l) peaks of the MAX phase, where the (0006) peak at 43.2° has the highest intensity. A smaller peak is also observed at 41.9°, next to the (0006) peak, which corresponds to the $(10\bar{1}3)$ crystal planes of the MAX phase. These "tilted grains" are commonly observed in MAX phase thin films[13,22,24] and from the relative intensity of the peaks we can estimate that they account for only 0.1%–0.4% of the film volume. From the position of the (0006) and $(10\bar{1}3)$ peaks, we can also calculate the lattice parameters $c = 12.524 \pm 0.002$ Å and $a = 2.902 \pm 0.003$ Å (for $x = 0.12$). The c lattice parameter is contracted by 0.3% compared to the epitaxial films on MgO(111) whereas a is identical.[13] The Si(004) substrate peak is also seen, but it is important to note that the amorphous native SiO_2 layer was not removed and therefore there is no epitaxial relationship between the film and substrate. No or only very minor traces of additional phases are seen, labeled by squares in the figure. These peaks did not unambiguously match any known phases but are most likely small Ga-rich Mn-Ga grains due to the slight excess of Ga which is necessary during growth to form the MAX phase.[13,25] The peak labeled by a star is the forbidden

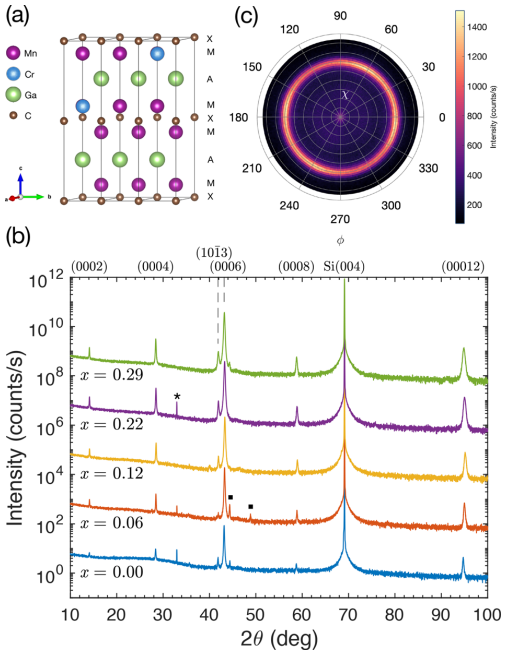

FIG. 1. Film structure. (a) Crystal structure of $(Mn_{1-x}Cr_x)_2GaC$. Cr randomly replaces Mn atoms on the M sites. (b) θ–2θ x-ray diffraction scans for x in the range 0.00–0.29 showing the characteristic (000l) series of MAX phase peaks. The squares and star denote peaks that do not belong to the MAX phase. (c) Pole scan of the (10 $\bar{1}$ 3) peak, showing a polycrystalline structure with strong (000l) texture.

Si (002) reflection which can be observed for specific in-plane orientations.[26]

Figure 1(c) shows a pole figure obtained for the $(10\bar{1}3)$ peak. A ring feature of fairly even intensity is seen at $\chi = 59°$ which corresponds exactly to the angle between the (000l) and $(10\bar{1}3)$ planes, showing that the (000l) planes are almost fully parallel with the substrate surface but there is no preferred in-plane orientation of the crystallites. Pole figures on the (0006) peak confirm this picture as well (not shown). Therefore, the films are polycrystalline, but nonetheless strongly (000l) textured, in the absence of any epitaxial relationship with the substrate. A small proportion of $(10\bar{1}3)$ oriented grains are also present.

The magnetic properties of the films were determined by vibrating sample magnetometry (VSM) in a Lakeshore 8600 system and a Cryogenics Inc. Cryogen-Free Magnet System at room temperature. Figure 2 shows the magnetic hysteresis loops for different Cr doping levels, where the diamagnetic background from the Si substrate has been removed by fitting a linear function to the saturation region (above 1 T) and subtracting it from the data. The inset shows data from the undoped sample which is antiferromagnetic at room temperature, but undergoes a metamagnetic transition to the non-collinear ferromagnetic state at above 2.5 T. This behavior is almost identical to

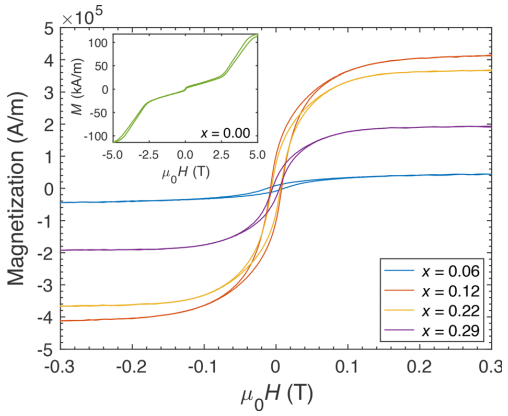

FIG. 2. Magnetic response. Magnetic hysteresis loops for x in the range 0.06–0.29 at room temperature. The inset shows the undoped sample ($x = 0$) up to an applied field of 5 T.

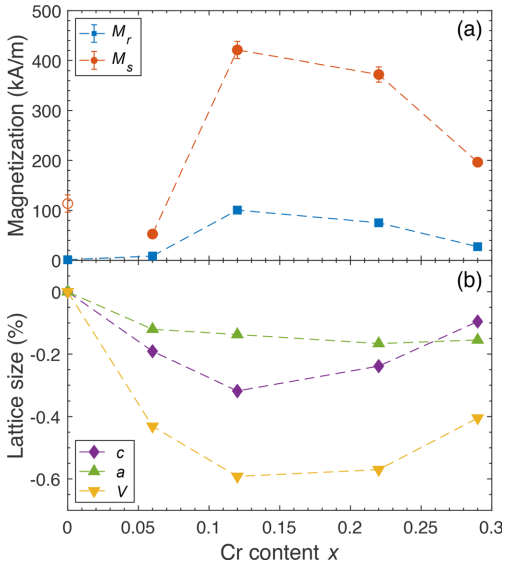

FIG. 3. Composition dependence of magnetization. (a) Saturation magnetization M_s and remanent magnetization M_r as a function of composition. The magnetization peaks for $x = 0.12$. The M_s value for the undoped sample is denoted with an unfilled circle to highlight that it is evaluated at 5 T compared to 1.5 T for the doped samples. (b) The change in lattice parameters c and a, as well as the unit cell volume V, relative to the undoped film. The uncertainty in the composition values (the x axis) is estimated as ± 0.03.

that found previously in epitaxially grown films, except for the slightly higher transition field.[11–13] All of the Cr-doped films show a typical ferromagnetic response with a considerable remanent magnetization M_r and a coercive field H_c in the range 3–6 mT. It should be noted that many types of magnetic ordering such as ferrimagnetism or various non-collinear alignments can manifest in this way and therefore it is quite possible that the films are not simple collinear ferromagnets. However, in the interest of readability, we use the term ferromagnetism as a supercategory of magnetically ordered states with a ferromagnetic-like response.

The saturation magnetization M_s for the different compositions can be seen in Fig. 3(a), together with the remanence M_r. Volume magnetization values were calculated using the films' lateral dimensions and thicknesses, determined by XRR (not shown). The M_s value for the undoped sample is evaluated at 5 T, above the metamagnetic transition, and is therefore not fully comparable to the other M_s values which are extracted at 1.5 T. The magnetization peaks at $M_s = 420 \pm 20$ kA/m for the Cr content $x = 0.12$, which is slightly higher than the peak magnetization of 380 kA/m in epitaxial $(Mn,Cr)_2GaC$ films. Theory suggests that ferromagnetism in Mn_2GaC is associated with a contraction in the c lattice parameter[27] and our previous results on epitaxial films showed an inverse correlation between the magnetization and the unit cell volume.[13] A similar correlation is found here, as shown in Fig. 3(b). The c lattice parameter has a minimum of 12.524 ± 0.002 Å at $x = 0.12$, which is the composition with the highest magnetization, and this also coincides with a minimum in the unit cell volume V. This corresponds to a 0.3% contraction in the c lattice parameter compared to epitaxial $(Mn_{0.88}Cr_{0.12})_2GaC$ films on MgO (111), which further supports the theoretically predicted relationship between the c lattice parameter and ferromagnetic coupling between the M atoms in the $(Mn,Cr)_2GaC$ system.

Magnetic hysteresis loops were collected as a function of both the azimuthal angle ϕ and the polar angle θ in order to examine the magnetic anisotropy of the films. The remanent magnetization, normalized by the saturation magnetization M_r/M_s, is shown in a polar representation in Fig. 4. The in-plane measurements (rotation around ϕ) show no variation in M_r/M_s, meaning that the films are isotropic in the plane, regardless of Cr content. This is to be expected since there is no preferred in-plane orientation of the crystallites, as seen in the XRD pole figures. Rotation around the polar angle θ (from in-plane to perpendicular to the plane) shows a typical easy-plane response for all the films except for $x = 0.06$, which is almost isotropic with respect to θ. Overall, the films with $x = 0.12$ and above therefore have an in-plane anisotropy and are isotropic within the film plane. Using the measured magnetization of the films, we can calculate the shape anisotropy using $K_s = \mu_0 M_s^2/2$ and compare it to the measured effective anisotropy $K_{\text{eff}} = \mu_0 H_{\text{sat}} M_s/2$ where H_{sat} is the saturation field perpendicular to the plane. We find that the two are within error equal, which means that the observed directional dependence can be attributed to shape anisotropy. However, undoped Mn_2GaC has been shown to have magnetocrystalline anisotropy with (000l) as the easy planes in its low temperature non-collinear ferromagnetic state[13] and we cannot rule out that this is a secondary contributing factor here. The film with the lowest Cr content shows markedly different, isotropic, behavior. This, together with the low magnetization, is a sign that the magnetic ordering for such low Cr levels could be non-collinear in nature, more like the undoped Mn_2GaC phase. However, it is important to note that its small magnetization will also reduce the shape anisotropy which reduces the driving force for in-plane magnetic alignment.

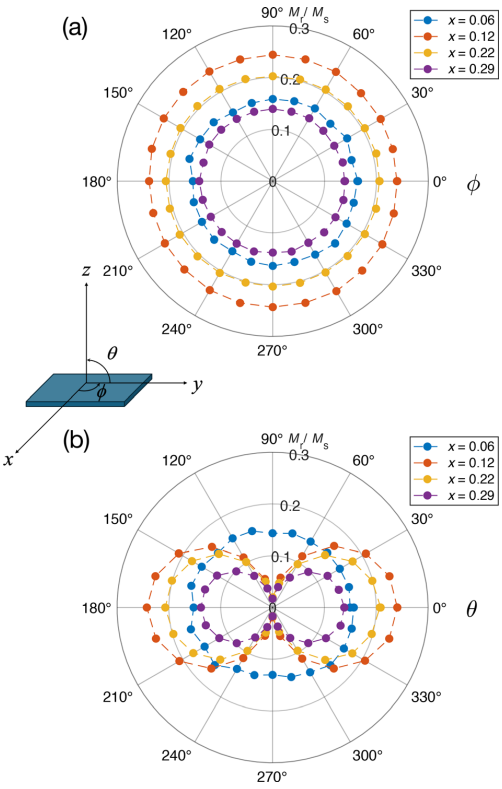

FIG. 4. Directional dependence of magnetic properties. (a) Normalized remanent magnetization as a function of the azimuthal angle ϕ showing that the films are isotropic in the film plane. (b) Normalized remanent magnetization as a function of the polar angle θ showing that all the compositions have an in-plane anisotropy except for $x = 0.06$.

In summary, we have shown that phase pure $(Mn_{1-x}Cr_x)_2GaC$ MAX phase films can be grown on standard Si substrates, without removal of the amorphous native oxide. The films are polycrystalline but highly (000*l*) textured. For a Cr doping of $0.06 < x \leq 0.29$, the films have a ferromagnetic response at room temperature with a sizable magnetization and an in-plane magnetic anisotropy. The results demonstrate that such a strong magnetic response can be obtained at room temperature in a MAX phase without the need for epitaxial growth on specific substrates. The magnetic properties are largely the same in both polycrystalline and epitaxial films which shows that the magnetic ordering is robust even in the presence of defects or small changes in film stress. This greatly facilitates the use of $(Mn_{1-x}Cr_x)_2GaC$ in practical applications, such as in spintronic devices or as a bulk magnet.

We wish to acknowledge funding from the University of Iceland Research Fund and the Icelandic Research Fund (Grant Nos. 174271, 2410333, and 217843).

AUTHOR DECLARATIONS

Conflict of Interest

The authors have no conflicts to disclose.

Author Contributions

E. B. Thorsteinsson: Formal analysis (equal); Investigation (equal); Methodology (equal); Writing – review & editing (equal). **D. Dagbjartsson:** Investigation (supporting); Visualization (supporting); Writing – review & editing (equal). **A. S. Ingason:** Conceptualization (equal); Methodology (equal); Supervision (supporting); Writing – review & editing (equal). **F. Magnus:** Conceptualization (equal); Formal analysis (equal); Investigation (equal); Methodology (equal); Project administration (lead); Supervision (lead); Visualization (lead); Writing – original draft (lead); Writing – review & editing (equal).

DATA AVAILABILITY

The data that support the findings of this study are available from the corresponding author upon reasonable request.

REFERENCES

[1]M. Dahlqvist, M. W. Barsoum, and J. Rosen, Mater. Today **72**, 1 (2024).
[2]M. W. Barsoum, Prog. Solid State Chem. **28**, 201 (2000).
[3]M. W. Barsoum and T. El-Raghy, Am. Sci. **89**, 334 (2001).
[4]A. S. Ingason, M. Dahlqvist, and J. Rosen, J. Phys. Condens. Matter. **28**, 433003 (2016).
[5]A. S. Ingason, A. Mockute, M. Dahlqvist, F. Magnus, S. Olafsson, U. B. Arnalds, B. Alling, I. A. Abrikosov, B. Hjorvarsson, P. O. A. Persson, and J. Rosen, Phys. Rev. Lett. **110**, 195502 (2013).
[6]M. Dahlqvist, A. S. Ingason, B. Alling, F. Magnus, A. Thore, A. Petruhins, A. Mockute, U. B. Arnalds, M. Sahlberg, B. Hjorvarsson, I. A. Abrikosov, and J. Rosen, Phys. Rev. B **93**, 014410 (2016).
[7]R. Meshkian, A. S. Ingason, U. B. Arnalds, F. Magnus, J. Lu, and J. Rosen, APL Mater. **3**, 076102 (2015).
[8]A. Petruhins, A. S. Ingason, J. Lu, F. Magnus, S. Olafsson, and J. Rosen, J. Mater. Sci. **50**, 4495 (2015).
[9]R. Salikhov, A. S. Semisalova, A. Petruhins, A. S. Ingason, J. Rosen, U. Wiedwald, and M. Farle, Mater. Res. Lett. **3**, 156 (2015).
[10]A. Mockute, P. O. A. Persson, F. Magnus, A. S. Ingason, S. Olafsson, L. Hultman, and J. Rosen, Phys. Status Solidi RRL **8**, 420 (2014).
[11]A. S. Ingason, A. Petruhins, M. Dahlqvist, F. Magnus, A. Mockute, B. Alling, L. Hultman, I. A. Abrikosov, P. O. A. Persson, and J. Rosen, Mater. Res. Lett. **2**, 89 (2014).
[12]I. P. Novoselova, A. Petruhins, U. Wiedwald, A. S. Ingason, T. Hase, F. Magnus, V. Kapaklis, J. Palisaitis, M. Spasova, M. Farle, J. Rosen, and R. Salikhov, Sci. Rep. **8**, 2637 (2018).
[13]E. B. Thorsteinsson, A. S. Ingason, and F. Magnus, Phys. Rev. Mater. **7**, 034409 (2023).
[14]C. M. Hamm, J. D. Bocarsly, G. Seward, U. I. Kramm, and C. S. Birkel, J. Mater. Chem. C **5**, 5700 (2017).
[15]H. Pazniak, M. Stevens, M. Dahlqvist, B. Zingsem, L. Kibkalo, M. Felek, S. Varnakov, M. Farle, J. Rosen, and U. Wiedwald, ACS Appl. Nano Mater. **4**, 13761 (2021).
[16]S. Lin, Y. Huang, L. Zu, X. Kan, J. Lin, W. Song, P. Tong, X. Zhu, and Y. Sun, J. Alloys Compd. **680**, 452 (2016).
[17]Y. Li, S. Zhu, E. Wu, H. Ding, J. Lu, X. Mu, L. Chen, Y. Zhang, J. Palisaitis, K. Chen, M. Li, P. Yan, P. O. A. Persson, L. Hultman, P. Eklund, S. Du, Y. Kuang, Z. Chai, and Q. Huang, J. Phys. Chem. Lett. **14**, 481 (2023).
[18]Y. Li, J. Lu, M. Li, K. Chang, X. Zha, Y. Zhang, K. Chen, P. O. A. Persson, L. Hultman, P. Eklund, S. Du, J. S. Francisco, Z. Chai, Z. Huang, and Q. Huang, Proc. Natl. Acad. Sci. **117**, 820 (2020).
[19]L. Chen, Y. Li, B. Zhao, S. Liu, H. Zhang, K. Chen, M. Li, S. Du, F. Xiu, R. Che, Z. Chai, and Q. Huang, Adv. Sci. **10**, 2206877 (2023).

[20]J. Dey, E. Jedryka, R. Kalvig, U. Wiedwald, M. Farle, J. Rosen, and M. Wójcik, Phys. Rev. B **108**, 054413 (2023).
[21]Q. Tao, A. Mockute, F. Orlandi, D. Khalyavin, P. Manuel, G. Palsson, B. Ouladdiaf, J. Rosen, and A. T. Boothroyd, "Magnetic structure of Mn_2GaC thin film by neutron scattering," J. Phys: Condens. Matter **37**(17), 175802 (2025).
[22]E. B. Thorsteinsson, M. Dahlqvist, A. Elsukova, A. Petruhins, P. O. A. Persson, J. Rosen, A. S. Ingason, and F. Magnus, APL Mater. **11**, 121102 (2023).
[23]E. Thorsteinsson, M. Dahlqvist, A. Elsukova, A. Petruhins, P. Persson, J. Rosen, A. Ingason, and F. Magnus, Vacuum **233**, 113856 (2025).
[24]P. Eklund, M. Bugnet, V. Mauchamp, S. Dubois, C. Tromas, J. Jensen, L. Piraux, L. Gence, M. Jaouen, and T. Cabioc'h, Phys. Rev. B **84**, 075424 (2011).
[25]A. S. Ingason, A. Petruhins, and J. Rosen, Mater. Res. Lett. **4**, 152 (2016).
[26]P. Zaumseil, J. Appl. Cryst. **48**, 528 (2015).
[27]M. Dahlqvist and J. Rosen, Sci. Rep. **10**, 11384 (2020).